Design and Deployment of Bicep:

A Novel Small-Aperture CMB Polarimeter to Test Inflationary Cosmology

Thesis by

Ki Won Yoon

In Partial Fulfillment of the Requirements

for the Degree of

Doctor of Philosophy

California Institute of Technology

Pasadena, California

2007

(Submitted October 3, 2007)

Acknowledgments

I have been privileged to have worked for the past several years in a richly stimulating and rewarding environment, free of most worries but for the challenging work itself — allowed to freely explore ideas, fail, and sometimes succeed even, of my own volition. My adviser Andrew Lange has never hesitated to place utmost importance on independence and intellectual freedom in my development as a scientist, and for that I am grateful.

Much of what I know, and worth knowing at all, I have learned from a rich cast of fellow students, post-docs and scientists, past and present. To Marcus Runyan and Bill Jones, whom I have peppered with countless questions over the years, thank you for bringing me into the fold. Fellow Bicep'ers Cynthia Chiang, Evan Bierman, Yuki Takahashi and Denis Barkats, thank you for the great camaraderie over the years outside work as much as in it. To those who have served as impromptu mentors as much as co-workers, Jamie Bock, Darren Dowell, Brian Keating, John Kovac, Chao-Lin Kuo and Hien Nguyen, thank you all for the encouragements. It's been a great learning experience. It goes without saying, all this takes place under the aegis of ever-reliable and resourceful Kathy Deniston, whose admistrative skills it is hard to fathom we could have done without, even temporarily.

Last but not least, my family has never wavered in their unconditional support of all I do — Mom, Dad, Kijung, thank you so much. Jean, words are not enough. Thank you for putting up with the madness and standing by me in spite of it all.

Abstract

BICEP is a ground-based millimeter-wave bolometric array designed to study the polarization of the cosmic microwave background radiation (CMB) and galactic foreground emission. Such measurements probe the energy scale of the inflationary epoch, tighten constraints on cosmological parameters, and verify our current understanding of CMB physics. BICEP consists of a 250 mm aperture refractive telescope that provides an instantaneous field-of-view of $17°$ with angular resolution of $0.93°$ and $0.60°$ at 100 GHz and 150 GHz, respectively, coupled to a focal plane of 98 polarization-sensitive bolometers.

This work details the design and characterization of the instrument, with discussion of preliminary results from data collected beginning inaugural 2006 observing season at the South Pole through present. Instrument testing indicates that the systematic contaminations of the B-mode will be below the threshold required for probing down to a tensor/scalar ratio of $r = 0.1$. Positive detection of the E-mode polarization is reported, while the B-mode maps are consistent with noise. In addition, the fractional polarization of the galactic foreground is constrained to $f < 0.05$ at moderate galactic latitudes.

Contents

List of Figures

List of Tables

CHAPTER 1

Introduction

1.1 Why inflation?

How did the universe begin? It is one of the most fundamental human curiosities, and, remarkably, one which is now firmly in the realm of testable scientific inquiry. In less than a century, Einstein's general relativity and advances in other areas of fundamental theoretical physics have combined with astronomical observations to radically alter our view of the universe — from a static picture to that of a dynamic cosmos endowed with a particular history and an ostensible beginning.

The resulting Big Bang model, describing an expanding and cooling universe, has proved to be exceptionally robust in the face of observational scrutiny. Most recently, precision measurements of the spatial fluctuations in the cosmic microwave background (CMB), the residual 2.7 K radiation from Big Bang, have continued to provide dramatic confirmations of the model, establishing the geometry and the content of the universe with unprecedented and ever-increasing precision.

However successful in explaining the nucleosynthesis of light elements, the existence and the properties of the CMB, and the expansion history of the universe, the standard Big Bang model cannot adequately account for a number of fundamental puzzles:

- Why is the geometry of the universe so flat today? Without a fine-tuning of the curvature of space in the beginning, any slight deviation from flatness would have quickly grown with time, resulting in a re-collapse or a runaway expansion.

- Why is the universe so uniform? The CMB is observed to be isotropic to one part in 10^5, seemingly over causally disconnected regions on the sky.

- Where did the primordial fluctuations that grew to present-day large-scale structures originate?

The inflationary paradigm[13] is the leading candidate for solving these mysteries. It describes an exponential expansion of the universe during the first 10^{-35} seconds preceding the ordinary Big Bang, driven by the vacuum energy at energy scales of 10^{16} GeV — approaching a level at which the strong, weak, and electromagnetic forces are expected to unify in a Grand Unification Theory (GUT). Such an inflation implies that the entire observable universe today grew from a primordial sub-nuclear volume of space, and that the seeds of large-scale structures are in fact the quantum fluctuations present in that volume. It is an astonishing idea, but, fortunately, one with observable consequences.

1.2 CMB polarization and consequences of inflation

Numerous experimental efforts in recent years have confirmed that the temperature and polarization anisotropies in the CMB contain a wealth of information about the evolution and content of the universe. The detailed results of these observations have provided a growing confidence in the inflationary paradigm of the origin of the cosmos. One of the basic predictions of the theory of recombination — the decoupling of the CMB from matter during the formation of atoms at redshift ~ 1100 — is that the CMB will be polarized at the level of a few percent of the temperature anisotropy, and that this polarization will have a curl-free, or E-mode, pattern that is correlated with the temperature anisotropy.

This polarization signature has now been detected by several experiments over a wide range of angular scales (arcminutes to tens of degrees), providing a heartening and important confirmation of our basic understanding of CMB physics. DASI was the first to report a detection in 2002[24], followed by WMAP's 1-yr measurement of TE-correlations[23], and more recently complemented by results from BOOMERANG[32][36], CBI[40], CAPMAP[1], and multi-year analyses from both
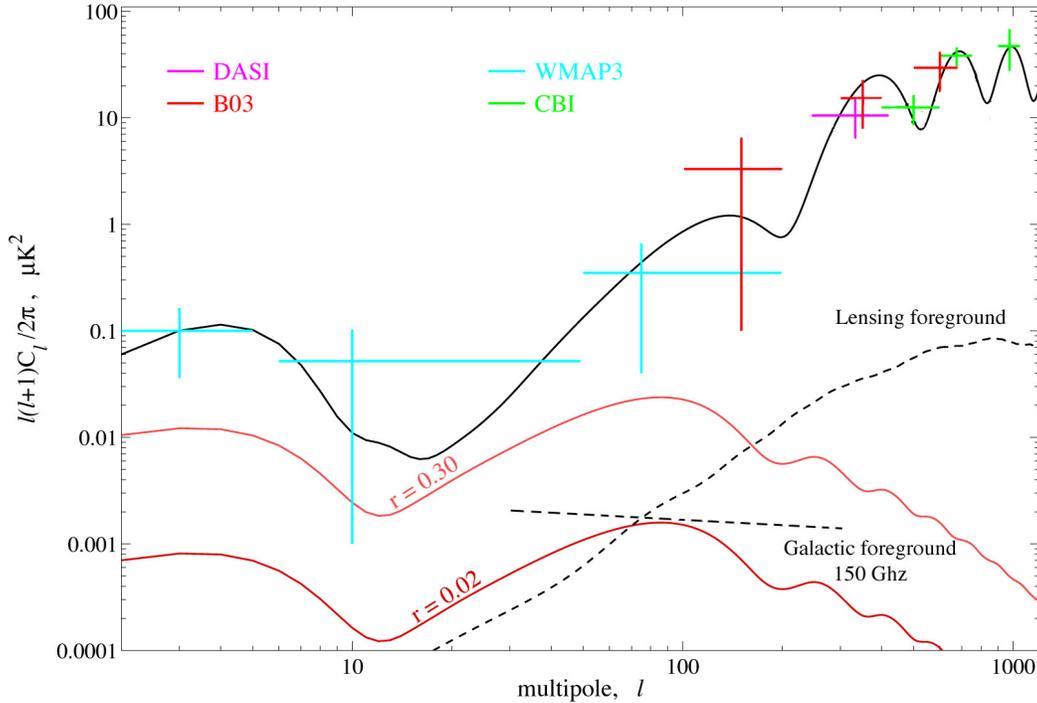
Figure 1.1: Recent measurements of the E-mode CMB polarization. Although a number of experiments have detected the polarization of the CMB over a wide range of angular scales, none have constrained it tightly, and the best upper limit on the tensor perturbations to date is $r \sim 0.3$. The level of the galactic foreground is estimated for the cleanest region of the sky available from the South Pole.

DASI[28] and WMAP[35], among others.

By verifying the theoretical model and further tightening the constraints on the cosmological parameters, the polarization measurements thus far have laid a strong foundation for tackling an even more elusive goal: measuring the B-mode polarization of the CMB. As much as the temperature and E-mode polarization are a relic of scalar or density fluctuations in the early universe, the B-modes are a direct probe of primordial tensor or gravitational wave perturbations[18]—a generic prediction of inflationary models. This curl component of the CMB polarization, if detected, would be the clearest and most unambiguous evidence of inflation having taken place.

The B-mode polarization is expected to peak at degree angular scales at $\ell \sim 100$, with the magnitude of the power spectra directly related to the energy scale of the inflation. Current best upper limit come from WMAP, at $r \sim 0.3$, where r is the ratio of the initial tensor to scalar spectra at $k = 0.002$ Mpc^{-1}, still well above being limited by the galactic synchrotron and dust polarization foregrounds and the lensing confusion which converts the much brighter E-modes to B-modes at

higher ℓ.

So far, inflation has passed every observational test. Yet the critical test still remains: the detection of gravitational wave background (GWB) and its faint imprint on the CMB polarization. An instrument designed to target the expected peak of the B-mode signature at $\ell \sim 100$, with judicious selection of observed field and careful control of systematics, can and should be able to probe deeply below the current best upper limits on r with the foreground contaminations well below the instrument sensitivity. BICEP, utilizing proven bolometric technologies albeit with unprecedented total sensitivity and well-focused science goals, is just such an effort.

CHAPTER 2

Instrument Design

2.1 Instrument overview

BICEP[21] is a mm-wave bolometric array designed specifically to target the B-mode polarization of the CMB at degree-scale angular resolution, where the signature of the primordial GWB is expected to peak. Such a measurement would constitute a powerful new evidence in support of inflation, and a remarkable probe of the energy scales of the earliest processes in the birth of the universe.

A realistic attempt at measuring the B-modes from the ground requires not only high system sensitivity, but an instrument and observing strategy specifically geared towards exquisite control of systematics. In tailoring BICEP for sensitive detection of degree-scale polarization, we have taken care to minimize or avoid possible sources of systematic contaminations that would otherwise dwarf the sub-μK cosmological signal. BICEP utilizes field-proven detectors, instrumentation, and mm-wave technologies, albeit combined with a novel optical and operational design, resulting in a reliable, easy to characterize, and compact instrument optimized for its inflationary science goals.

The instrument can be largely divided into four major functional parts: (1) mm-wave optics and bolometer focal plane, (2) cryogenic and vacuum systems, (3) telescope mount and control, and (4) signal and housekeeping electronics. Figure 2.1 gives a simplified overview of these major pieces of the instrument.

At the heart of BICEP is a simple 2-lens telescope coupled to a focal plane of corrugated feedhorns, designed to work at 100 GHz and 150 GHz — large windows in Earth's atmospheric opacity which
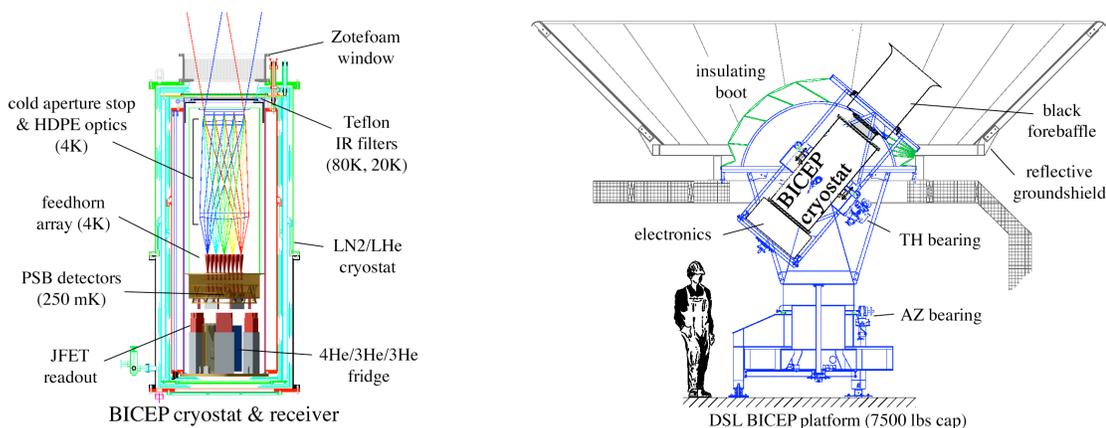
Figure 2.1: BICEP receiver and mount as installed on site. The core instrument consists of a cryogenically-cooled two-lens refractive telescope coupled to a focal plane of 100 GHz and 150 GHz polarization-sensitive bolometers (PSBs) via corrugated feedhorns. Liquid helium cryogenic cooling is necessary to both sufficiently cool the optical elements to minimize radiative loading onto the detectors, and as a thermal base for the helium sorption fridge system that provides the sub-Kelvin working temperatures for the PSBs. Once integrated with the three-axis mount (azimuth, elevation and boresight rotation) and housed inside the observation laboratory, the telescope is fully protected from the outside elements by the co-moving flexible environmental seal, with only the main aperture and the forebaffle exposed through the roof cut-out. The building's roof also supports the reflective fixed groundscreen which minimizes the refracted ambient radiation from contaminating the signal.

are, rather fortuitously, not far from the peak CMB blackbody radiation and roughly coincident with the expected null in the galactic foreground emissions. This optical system then guides the incoming radiation to pairs of polarization-sensitive micromesh bolometers which populate the sub-Kelvin focal plane, 25 pairs at 100 GHz and 24 at 150 GHz (as deployed for the first season).

As simple as the above may sound, BICEP is indeed a straightforward instrument, with a straightforward if daunting mandate: directly measure the temperature and polarization of the CMB and foregrounds at degree angular resolution. Given this goal the design and engineering of BICEP, then, is a complex exercise in turning the core instrument concept into a powerful, functioning machine, capable of rewarding science.

The following sections detail the development and design considerations of the core instrument and all the supportive secondary subsystems necessary for the experiment to work as intended, along with discussion on some of the inevitable trade-offs, compromises and limitations encountered over the course of building BICEP.
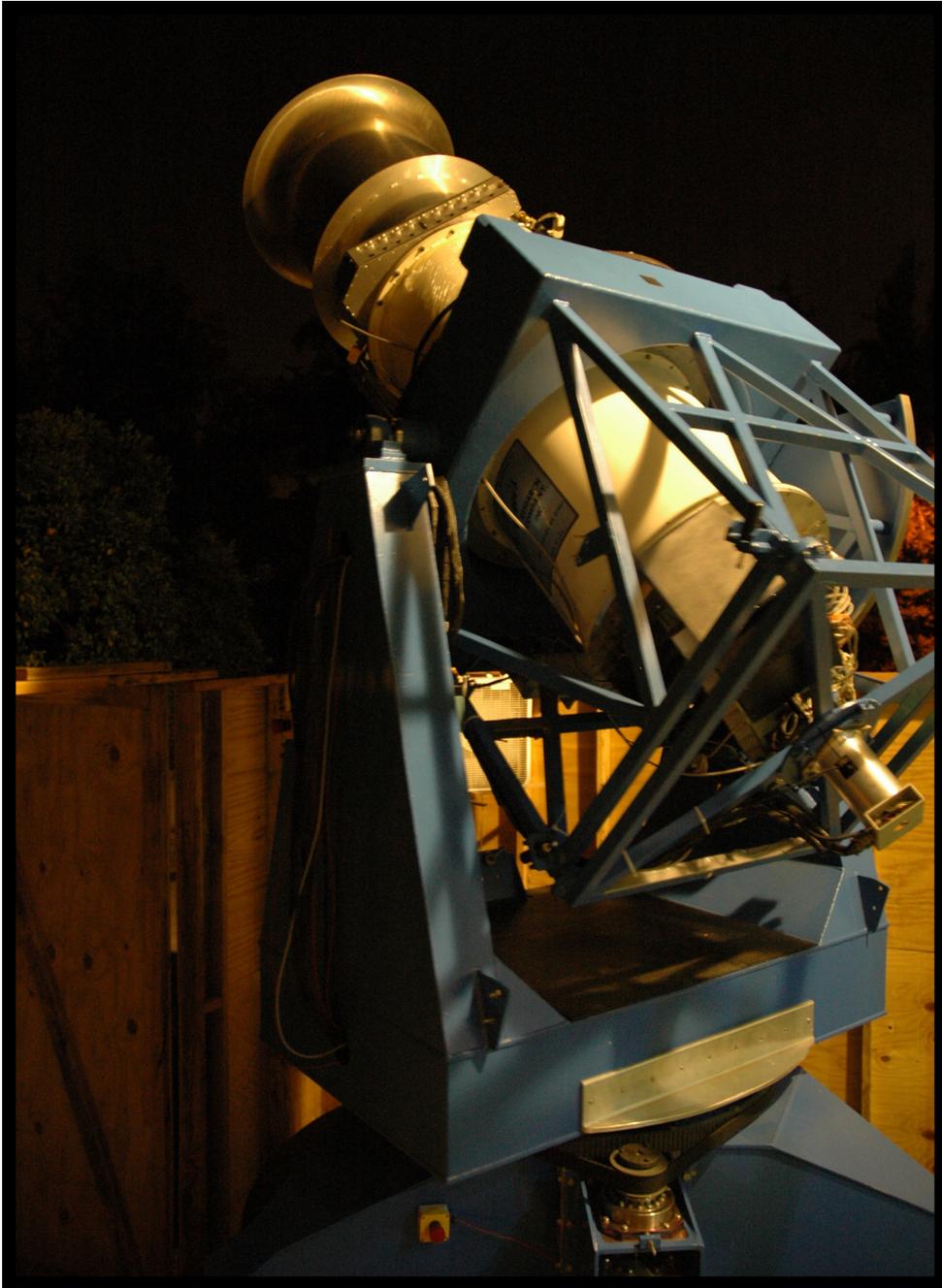
Figure 2.2: Fully operational BICEP cryostat and mount, during test observing in Pasadena, CA prior to deployment

Band Center (GHz)	Band Width (GHz)	No. of Detectors	Beam FWHM	NET ($\mu K_{CMB}\sqrt{s}$)
96.0	22.3	25	0.93°	480
150.1	39.4	24	0.60°	420

Table 2.1: BICEP instrument summary.

2.2 Cryostat

Because of the desire to eliminate ambient temperature reflectors and incorporate only the minimal set of optics that would provide the wide field-of-view (FOV) imaging at degree resolution, the entire core BICEP instrument is housed within a single, contiguous cryogenic volume. This required the development of a large cryostat, capable of accommodating up to 300 cm diameter optical window and providing multiple days of continuous operation at a base temperature of 4 K.

The 4 K base temperature is necessary as a heat sink for operating the multi-stage helium adsorption fridge which cools the detector focal plane to 250 mK — crucial for achieving the requisite raw bolometer sensitivities. While mechanical cryocoolers can provide continuous operation at 4 K without the need for liquid cryogens, we opted for a wet system that makes use of liquid nitrogen and liquid helium to both take advantage of our previous experience with similar systems, and also to avoid any unnecessary engineering and design complications from using a mechanical alternative.

The BICEP LN/LHe cryostat was designed and built in conjunction with Janis Research.[1] Because of the lack of external optics, the aperture of the cryostat must be upward-looking. This led to toroidal, nested cryogen tanks — the outer LN tank surrounding and shielding the inner LHe tank — with a large cylindrical central volume reserved for the cooled optics and the receiver. The optics/receiver insert is cooled via a high-conductivity Cu baseplate mounted to the bottom surface of the LHe toroidal tank using a single bolt circle.

Aside from providing adequate mechanical platform for housing the optics/receiver insert, the main design consideration for the cryostat is thermal. Efficient thermal design not only ensures that the frequency of operational cycle is reasonably low — minimizing thermal stressing and risks associated with each cryogenic transfer — but is absolutely essential at a remote location such as the South Pole where supplies are limited and vulnerable to failures outside the purview of the experiment.

Three major pathways of thermal conduction — between the outer 300 K shell and the LN tank, and between the LN and the LHe tanks — determine the hold-times of the two cryogens: (1) direct conduction from mechanical support structures, (2) radiative loading from non-zero emissivities of surfaces, and (3) optical loading from the aperture (addressed in more detail in section 2.3).

---

[1]Janis Research Company, Inc., Wilmington, MA 01887. Web: http://www.janis.com/
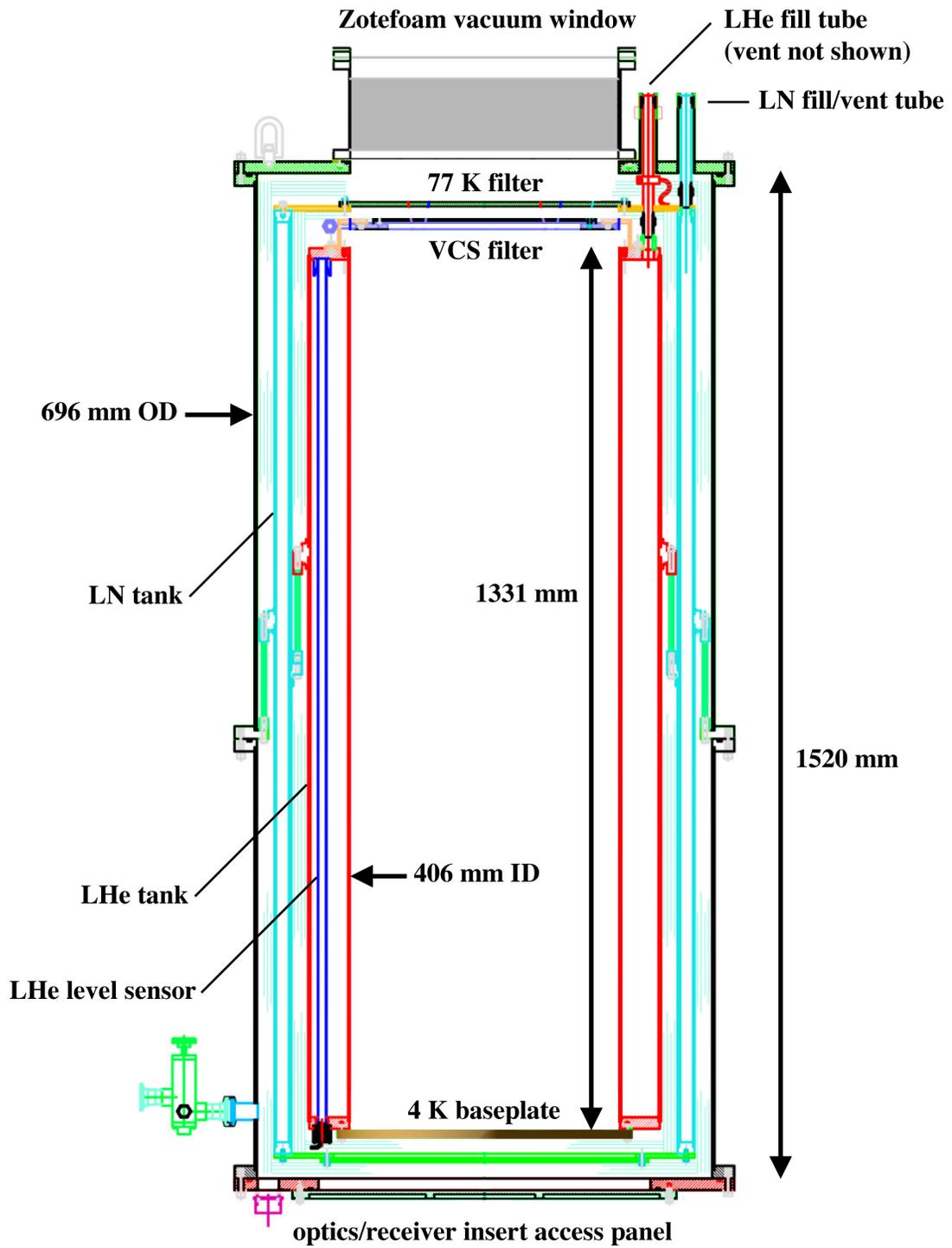
Figure 2.3: LN/LHe cryostat.

	Liquid Volumn (L)	Surface Area (m²)	Heat Capacity (W hr)	Operating Load (W)
LN	55	3.52	2450	25
LHe	110	2.66	77.6	0.44

Table 2.2: Nominal design dimensions of the two cryogenic tanks. The surface area is that of an equivalent solid cylinder. The operating load is from the measured boil-off rates during normal observing, and does not take into account excess load from fridge cycling, etc.

The two G10 truss structures between the outer shell, LN tank and the LHe tank are the sole mechanical supports, responsible for both bearing the weight of the filled tanks and the rigidity of alignments. The integrated thermal conductances between 300–77 K and 77–4 K can be calculated from published values,[31] giving 0.965 W/cm and 0.149 W/cm, respectively. The truss structures have total $A/L \approx 0.3$ cm, resulting in loadings of ~ 0.3 W and ~ 0.04 W, respectively, sub-dominant for both stages.

The net radiative energy flux between two surfaces with non-unity emissivities ϵ_H and ϵ_C, accounting for multiple reflections, is given by

$$\Delta\Phi \;=\; \frac{\epsilon_H \epsilon_C}{\epsilon_H + \epsilon_C - \epsilon_H \epsilon_C} \sigma\big(T_H^4 - T_C^4\big) \;\approx\; \frac{\epsilon_H \epsilon_C}{\epsilon_H + \epsilon_C} \sigma\big(T_H^4 - T_C^4\big) \qquad \text{for } \epsilon_H, \epsilon_C \ll 1 \tag{2.1}$$

derived from summing the resulting infinite geometric series. Without additional insulation, this would result in radiative heat loads of ~ 40 W and ~ 0.13 W for the two stages assuming 5% emissivity, unacceptably high for LN and not insignificant for LHe. The non-aperture radiative loading can be mitigated by using low emissivity multilayer insulation (MLI). Approximately 20–30 layers of aluminized mylar surround most of the exposed surfaces of both cryogen tanks, with integrated fibrous backing limiting conduction between layers from close contact.

With the design of the G10 support structures driven by mechanical requirements, and radiative loading minimized by MLI, much of the vulnerability for additional thermal loading — and potential for improving the cryogenic performance — lies in effectively limiting the broadband radiation through the aperture outside the observed science bands. The BICEP cryostat was designed with provisions for thermal rejection filters at the top of the LN and LHe tanks, with the latter coupled not to the tank itself but to an isolated stage cooled by the boil-off He gas through the vent line. This

makes use of the cooling power of the escaping gas that would otherwise be wasted, and provides an additional filtering stage to protect the LHe stage from excessive radiation.

2.3 Optics

BICEP's optical elements consists of an ambient temperature foam window, Teflon IR filters at 77 K and the He vapor-cooled 20 K stages, and 4 K cooled high-density polyethylene (HDPE) lenses which form a 17° FOV image of the sky at the focal plane of primary corrugated feedhorns.

The designs of these elements are driven my multiple concerns. First, the cooled image-forming optics must provide wide FOV imaging of the sky at infinity with low aberrations across the full focal plane. BICEP's axisymmetric refractive optical design partly addresses this, eliminating potential polarization systematics associated with off-axis designs or on-axis secondary support structures.

Second, the system must attain high optical efficiencies for both science frequency bands, to limit excessive instrument loading on the detectors and prevent degraded sensitivities to the CMB. Properly designed, the total in-band optical loading should be driven by the site-specific atmospheric opacity (expected at the order of ~ 10 K_{RJ}), and the instrumental contribution should be comparatively small and stable. Careful materials selection and thermal design are necessary to achieve this.

Third, out-of-band IR radiation must be sufficiently blocked from the LHe stage to achieve the long hold-times necessary for efficient overall operation of the experiment. While IR blocking does not directly impact the optical performance for the science at hand, this is crucial from an operation standpoint.

2.3.1 Zotefoam window

The 300-mm aperture vacuum window consists of four individual layers of Zotefoam PPA30,[2] heat-laminated to form a single 10-cm thick slab and sealed to an aluminum frame using Stycast epoxy. A similar low-loss Zotefoam window was used in ACBAR.[38] The window was measured to have $\sim 1\%$ loss at 150 GHz, adding an expected 2–3 K_{RJ} of optical loading on the detectors. Scattering at millimeter wavelengths is very low due to the small cell size (0.3 mm) and low density (30 mg/cm^3).

---

[2]Zotefoams Inc., Walton, KY 41094. Web: http://zotefoams.com/
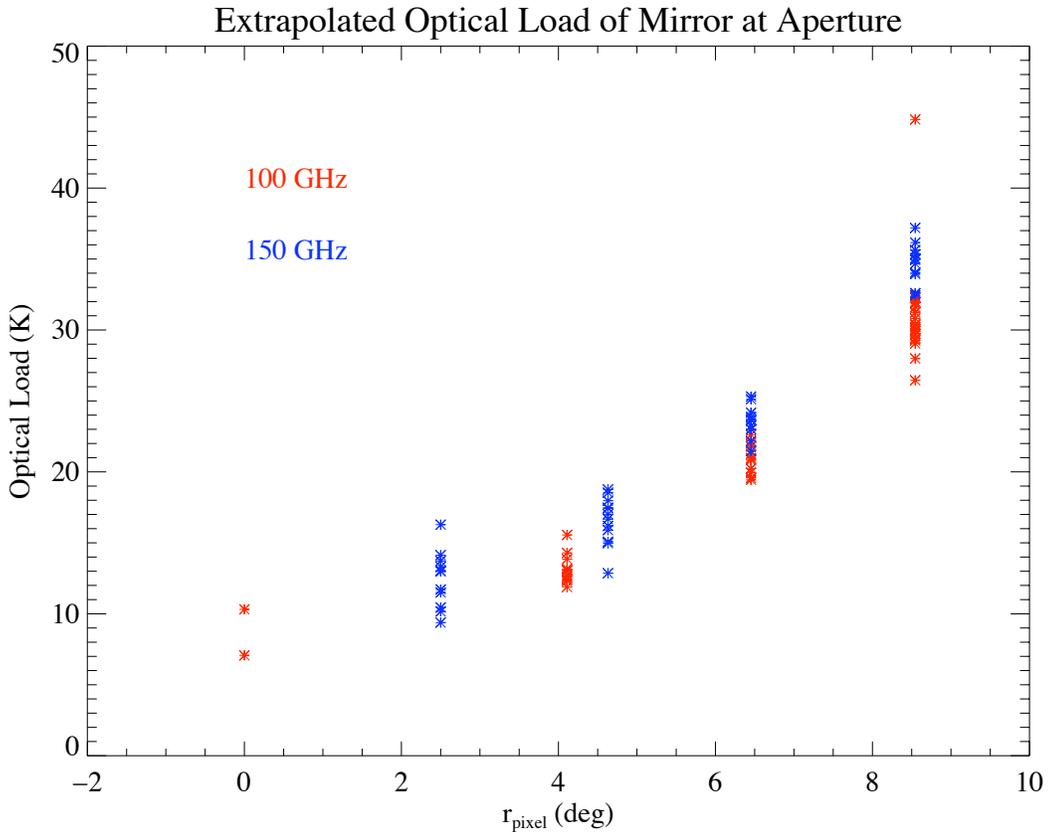
Figure 2.4: The upper limit on instrument loading is given by extrapolating the effective temperature of a flat reflector at the window aperture in comparison with standard 300/77 K loads. The asymptotic behavior of the effective loading versus pixel radius — falling to ~ 8–10 K at the center pixel — indicates at most 4–5 K_{RJ} loading from the instrument assuming only a single bounce from the reflector. Multiple reflections would lower this limit further.

Because the foam window is radiatively cooled to below ambient temperature from both sides, frost can form from residual moisture in the air. To prevent this, a taut 18-μm polypropylene film was installed as a cover, with the airspace between the cover and the Zotefoam window slightly pressurized and continuously purged by warm dry nitrogen gas.

Because the rest of the optics is internal to the cryostat and cooled to cryogenic temperatures, instrument optical loading is minimized and is dominated by the ambient vacuum window (see Table 2.3). The measured upper limit on the instrument loading is less than 4–5 K_{RJ}, consistent with the expected loading of ~ 3.5 K_{RJ} in both frequency bands (Figure 2.4).

	100 GHz (pW)	(K_{RJ})	150 GHz (pW)	(K_{RJ})
CMB	0.067	0.97	0.059	0.53
Sky	1.16	16.7	0.584	5.3
Window	0.160	2.30	0.250	2.79
77 K Teflon	0.063	0.90	0.098	0.89
VCS Teflon	0.013	0.19	0.019	0.17
4 K spillover	0.007	0.10	0.008	0.07
4 K lenses	0.002	0.03	0.003	0.03
Total	1.47	21.2	1.02	9.3

Table 2.3: Expected in-band optical loading. The sky dominates the total loading, and in turn the window dominates that of the instrument contributions.

2.3.2 IR-blocking filters

Effectively blocking the incoming IR radiation is crucial to reducing the thermal loading onto the LHe stage and subsequent optical elements at 4 K and below. Two absorptive PTFE (Teflon) filters of thickness 1.5 cm and 2.0 cm are used at the 77 K liquid nitrogen stage and the LHe vapor-cooled 20 K stage, respectively, for this purpose.

Application as an absorptive IR-blocking filter ideally requires good in-band transmission, high thermal conductivity to dissipate absorbed radiation to the edge, ease of anti-reflection coating or low index of refraction, and effective blocking above 3 THz. Attenuation below 3 THz provides negligible mitigation of the thermal loading onto 4 K. Teflon was chosen over other candidates for meeting the requirements in all of the above areas, with low in-band loss of 0.015 Np cm^{-1} at 150 GHz and a relatively low index of refraction n = 1.44.[26] The thermal conductivity of 1.4–2.2 mW cm^{-1} K^{-1} at 20–80 K is sufficient to dissipate the expected absorbed radiation,[7] and avoid excess heating of the filters beyond their usefulness. IR-attenuation properties are excellent for this application: ~ 3 Np cm^{-1} near the cut-on region at 3 THz, and negligible transmission at higher frequencies.[2]

To consider the thermal performance of the Teflon filters, we must first estimate the incident radiative loading from the ambient temperature Zotefoam window. Assuming the window is opaque at IR (dominating the total emissive radiation) and that the inside surface radiates onto much colder surroundings, the temperature of the inside surface T_{IN} can be estimated from equilibrium between

conduction through the window and blackbody radiation:

$$\frac{\kappa}{l}\left(T_{\mathrm{AMB}} - T_{\mathrm{IN}}\right) = \sigma T_{\mathrm{IN}}^4 \tag{2.2}$$

where $\kappa = 0.4~\mathrm{mW\,cm^{-1}\,K^{-1}}$ is the thermal conductivity of the foam window,[3] and $l = 10$ cm is the thickness. Solving the above gives $T_{\mathrm{IN}} = 145$–170 K for $T_{\mathrm{AMB}} = 210$–300 K, which covers the ambient temperature range between winter South Pole observing and lab testing conditions. Lab measurement of $T_{\mathrm{IN}} \approx 180$ K agrees well with the above approximation. Note that the physical surface temperature T_{IN} is a lower limit on the effective temperature incident on the colder stages, which will be the foam temperature at optical depth of unity.

Left unabated, the window would radiate ~ 4 W into the cryostat (confirmed through direct experience), or about ten times the final achieved operating load on the LHe stage! The presence of the IR filters are crucial for intercepting this load. Direct lab measurements of the filter temperatures indicate that during normal operation, the LN filter equilibrates at ~ 130–150 K at the center and ~ 80–100 K at the mounting edge, with the range driven by the LN fill level. The VCS filter — cooled by a 1 m long copper tube heat exchanger along the LHe vent — equilibrates at ~ 70–80 K at the center and ~ 15–25 K at the heat exchanger itself. This reduces the incident aperture radiation onto the LHe stage to an expected ~ 0.13 W.

This is in good agreement with an independent confirmation of the IR blocking efficiency, derived from comparing the LHe boil-off rates between the blanked-off cryostat and one in operational configuration with the window/filters installed. With the latter, the quiescent loading on the LHe is 15 L/day (~ 0.44 W). Blanked off, we measure 10 L/day (~ 0.29 W) — a difference of ~ 0.15 W.

Note that the primary role of the IR filters is thermal. It reduces the loading on the LHe stage, with the secondary benefit of easing the workload on the sub-K band-defining filters. They do *not* in any way function to define the science bands or to prevent harmonic leaks at multiples of the band-defining edges.

Without coating, the Teflon filters incur ~ 3.3% reflection per surface. Efficient anti-reflection coating is accomplished with Zitex, a porous Teflon sheet available in many thicknesses and den-

---

[3]As cited by the manufacturer for 10 °C: http://zotefoams.com/pages/EN/datasheets/PPA30.HTM

sities. The typical relative density compared to regular Teflon is ~ 40%, making it ideal for coating applications in conjunction with its parent material. The measured index of refraction of $n = 1.2$ agrees with expectation.[2] A single layer of Zitex per surface is used to achieve good transmission over both 100 GHz and 150 GHz bands, with ~0.5% reflection per surface.

Due to its low melting point at 120 °C, thin sheets of LDPE provide a cryogenically robust and mm-wave transparent bonding of the Zitex layers to the bare Teflon filters. Layers of LDPE 2-mil in thickness are sandwiched between Zitex and Teflon, and press-heated together above the melting temperature of LDPE. Teflon has a significantly higher melting point and is not degraded in this process.

2.3.3   HDPE lenses

BICEP uses two cryogenically-cooled biconvex lenses to image the focal plane to infinity, with the top objective lens providing the 250 mm aperture stop for degree-scale resolution. With the aperture size roughly determined by the desired angular resolution on the sky, the physical focal length of the optics is driven by considerations for the edge taper of the primary feedhorn beam profiles at the aperture and efficient packing density of pixels on the focal plane.

Because feedhorn-coupled arrays sample the sky sparsely, the pixels need to be closely packed for efficiency, with inter-pixel distances on the focal plane driven by the size of the feedhorn apertures. Minimum achievable feedhorn aperture diameter — without going under the limit set by the size of the PSB modules themselves, and accounting for clearances and wall thicknesses — was ~14 mm at 150 GHz, giving ~21 mm at 100 GHz by direct scaling so as to keep the illumination of the aperture the same between the two bands. (See Section 2.4.)

A −20 dB edge taper at the main aperture was chosen to minimize both far-field sidelobes and loss from internal spill-over, which translates to ~ $3.1f\lambda$ diameter feedhorn apertures assuming lowest-order gaussian coupling of beams to the lens optics. Equating this to the above physical aperture diameters provides the effective design f-number of $f/2.3$. We can then derive the plate scale of the focal plane, given by:

$$S = \frac{1}{f d_A} \times \left(\frac{180°}{\pi} \right) \approx 0.1 \,°/\text{mm} \tag{2.3}$$

where d_A is the diameter of the main aperture. The focal plane accommodates a ~170 mm diameter array of pixels, or ~17° diameter region on the sky.

Considering the packing density of the feedhorns on the focal plane is thus a crucial step in the design and implementation of the entire instrument, not only driving the design of the optics, but determining the overall scale of the telescope and setting the instantaneously accessible FOV, which in turn influence everything from baffling and ground shielding to scan strategy.

For reasons of ease of manufacture and low reflection loss, we chose HDPE[4] for the lenses. The performance of the HDPE design predicted by the ZEMAX software is similar to that for silicon and fused silica designs originally considered: Strehl ratios > 0.99 and cross polarization = few × 10^{-5} over the field of view. The induced linear polarization at the edge of the field is predicted to be 0.8% without the anti-reflection coatings, and less with the coatings, but this has not been confirmed with measurement.

The shape design of the lenses assumed a uniform 1.9% contraction of the lens between room and operating temperatures. The validity of this assumption was tested by measuring the $1.7 \pm 0.2\%$ contraction of a sample of the HDPE at room temperature and after immersion in liquid nitrogen. Using a Michelson interferometer, we measured an index of refraction of $n = 1.574 \pm 0.007$ at cryogenic temperatures, and we used this value in the optical design. Given an index of refraction similar to Teflon and a melting point (130 °C) that tolerates the LDPE bonding technique used in AR-coating the IR-blocking filters, both sides of the bi-convex lenses were similarly coated with Zitex.

To accommodate the thermal contraction mismatch between the HDPE lenses and the aluminum enclosure, each lens is mounted on three thin vertical aluminum vanes. This design is predicted to position the lens repeatably and was observed to be stiff. Flexible braided copper straps are attached from the lenses to the 4 K base of the telescope enclosure for heat sinking, and the VCS Teflon filter minimizes the incident radiation. The edge of the top lens is measured to equilibrate at < 8 K so negligible emission is expected from the lenses. Circular apertures located at the lenses and in two intermediate locations within the telescope are blackened with epoxy loaded with carbon black or iron filings[5] to minimize stray light.

---

[4]Accurate Plastics, Inc., Yonkers, NY 10705. Web: http://www.acculam.com/
[5]Emerson & Cumings, Billerica, MA 01821. Web: http://www.emersoncuming.com/

~ 800 mm

17° FOV

Zotefoam window   **Teflon filters**   **4 K HDPE lenses**   **4 K focal plane**
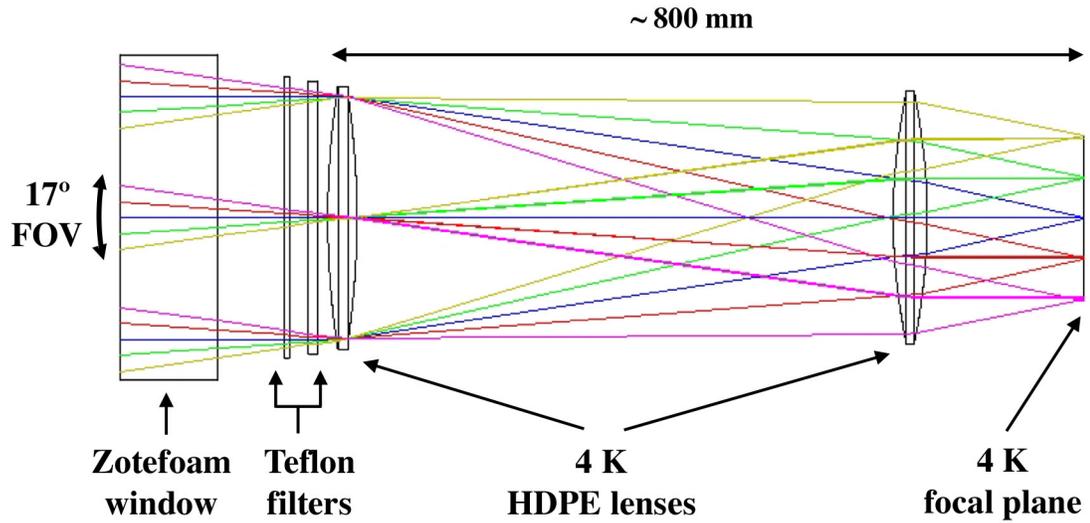
(a) Cooled f/2.3 2-lens optics. The objective lens serves as the 250 mm cold aperture stop.

center pixel   **4° off axis**   **8° off axis**

20 mm

Airy disk for 150 GHz (11.52 mm diameter)

(b) Geometric spot diagrams. The optical performance of the lenses is completely diffraction-limited, as the above comparisons between the 150 GHz Airy disk and geometric spot diagrams for various focal plane locations show.

Figure 2.5

2.4 Feedhorns

The image of the sky formed at the focal plane by the optics must be coupled to the bolometers with high polarization fidelity and optical efficiency, and well-defined spectral passbands. BICEP uses pro-filed corrugated feedhorns and capacitive metal mesh filters for this purpose, with each pixel on the focal plane consisting of 4 K primary and re-expanding feed horns in a back-to-back configuration, followed by a small thermal gap to the 250 mK band-defining filter stack and PSB coupling feed horn (Figure 2.6). This arrangement allows for the separation of design considerations between efficient coupling to the lens optics, spectral band definition, and proper interfacing to the bolometers, and is similar to that used in ACBAR, BOOMERANG, and *Planck* HFI.

If designed to propagate only the fundamental HE_{11} mode, profiled corrugated feedhorns can offer low sidelobe response and superior polarization characteristics over a wide bandwidth. This is easy to see when we look at the functional form of the aperture field distribution of such a design:

$$\vec{E}_t \propto J_0 \left(\frac{r}{a} u_{0,1} \right) \hat{i}_x \tag{2.4}$$

where a is the inner radius of the corrugations and $u_{0,1} = 2.405$ is the first zero of the zeroth-order Bessel function J_0. That is, the field distribution is radially tapered, possesses strictly linear polariza-tion, and is azimuthally symmetric, ideal for application in this context.

The detailed analytical calculations for the design of the corrugated feeds are available from Zhang (1993) [43] and numerous other references, which are not repeated here. Instead, the following discussion highlights a few of the considerations relevant to the specific designs in BICEP.

The design of the primary feedhorn must take into consideration three major constraints in ad-dition to the details of the corrugation geometry along the whole length: (1) throat geometry, driven by the required band definition; (2) flare profile, affecting both the acceptable level of propagation mode contamination and the overall length of the feedhorn; and (3) the aperture geometry, which reflect the maximum attainable packing density of the pixels given limitations on the compact design of the detector array.

In terms of the impact on the optical quality of the experiment, the design of the throat section
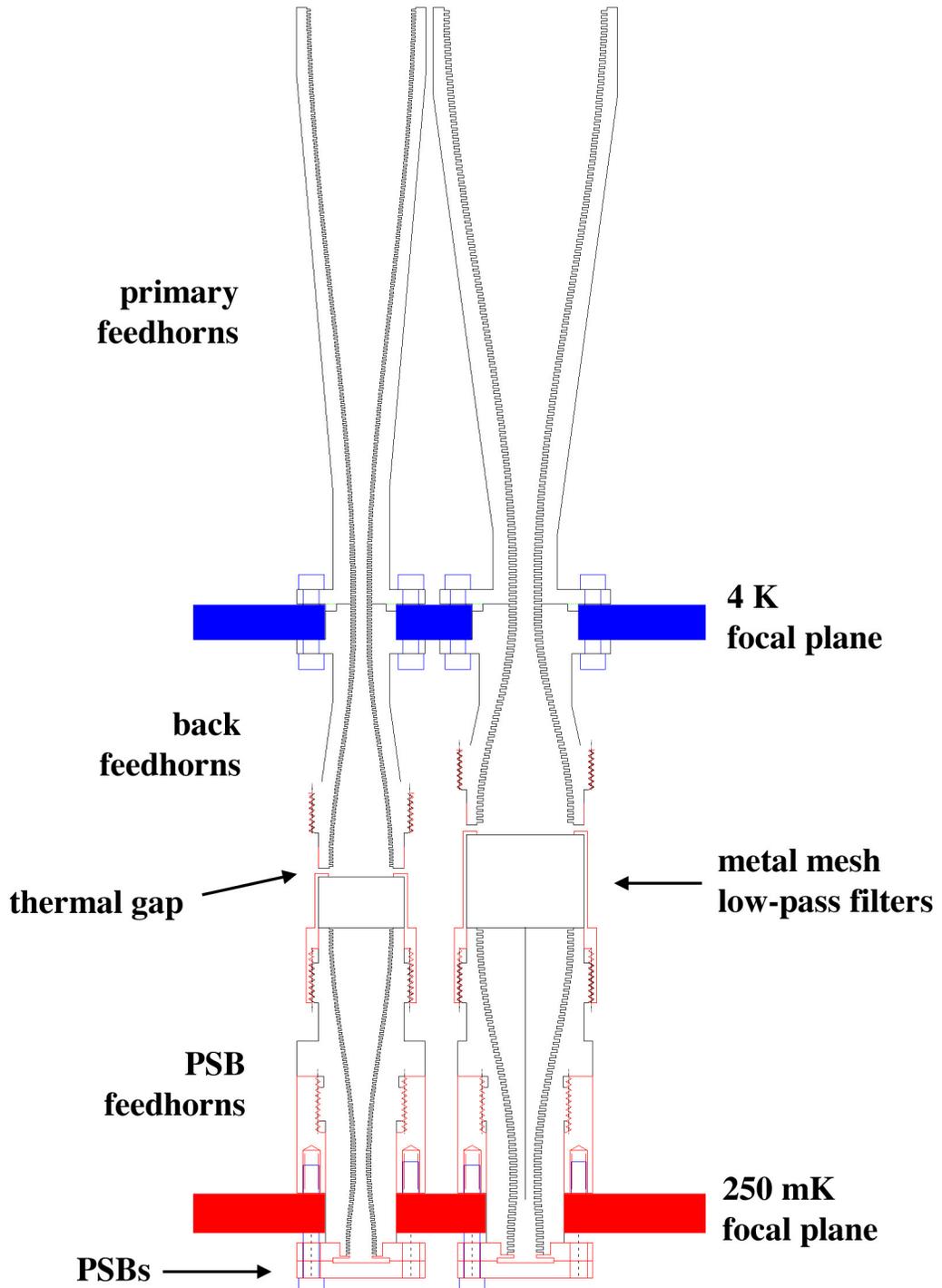
Figure 2.6: The optical aperture is illuminated by corrugated profiled 4 K feedhorns. Re-expanding back-facing feedhorns provide a convenient thermal gap between the 4 K back-to-back stage and the 250 mK focal plane. Sub-Kelvin metal mesh filters and the PSB coupling feedhornss define the spectral bands at both frequencies.

	β_{MAX}	a_{APERTURE} (mm)	w_0 (mm)	θ_{FWHM}
100 GHz	$10°$	10.695	6.89	$6.04°$
150 GHz	$6.5°$	7.130	4.59	$6.04°$

Table 2.4: Design parameters of primary feedhorns (maximum flare angle β_{MAX}, gaussian beam waist radius at the aperture w_0)

of the feedhorns is perhaps most crucial, as it directly influences the allowed modes of electromagnetic propagation, affecting the illumination pattern and polarization characteristics of the beams on the sky. In short, following Zhang's procedure, widest possible bandwidth for single-mode HE_{11} performance can be achieved by constraining the ratio of outer and inner radii of the corrugations to $b/a = 1.8309$ at the throat, then determining the inner radius a for the desired modal cut-on.

The determination of the waveguide cut-on in this case is equivalent to that of a smooth-walled circular waveguide: $ka = 1.841$, where k is the wavenumber at the lowest desired frequency of operation. In practice, because the throat sections have finite lengths on the order of nominal wavelengths, the actual achieved cut-on frequencies are noticeably higher and depend on the exact details of the corrugation design. Simulations with the HFSS software were used to numerically derive the effective cut-on condition with other constraints on the throat design present, giving $ka \approx 2.1$.

In BICEP, the lower edges of the bands are defined by the throat sections of the PSB feedhorns. The throat sections of the 4 K back-to-back feeds are of slightly larger diameters to accommodate the optional Faraday rotator modules, such that they can operate away from the waveguide cut-ons over the entire bandwidth. The numerically-derived design cut-ons were placed at 83 and 130 GHz for the two bands for the PSB feedhorns. The cut-ons for the back-to-back feedhorns are at 80 and 125 GHz and do not determine the overall spectral bands.

The design of the aperture diameters of the primary feedhorns is much simpler in comparison. They have the largest aperture diameters that still allow for the pixel density to be driven by the minimum achievable size of the PSB modules. The design values are given in Table 2.4. Given the target throat and aperture sizes, the flare section can be designed. BICEP makes use of a profiled design with continuously-varying flare angle instead of a conical one for two major reasons: (1) profiled feedhorns tend to be shorter in length than conical designs for similar performance, and (2) the
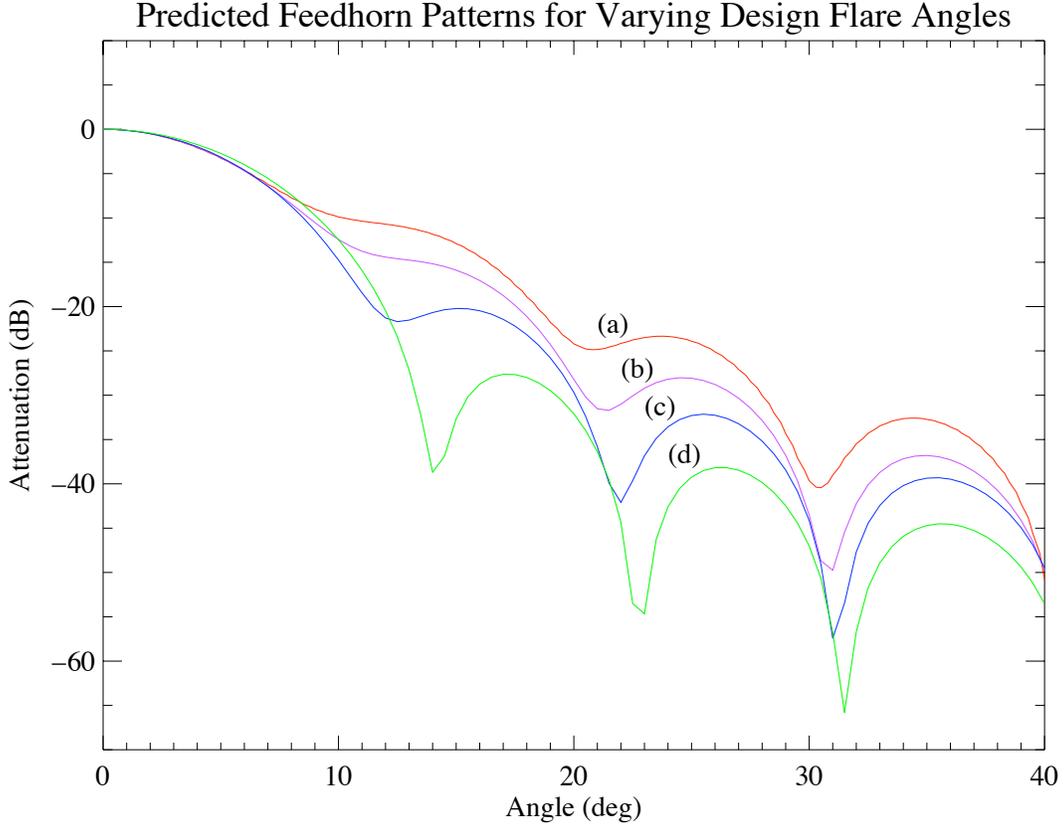
Figure 2.7: Maximum flare angle β_{MAX} vs. predicted beam patterns for profiled 100 GHz primary feedhorns. The curves {(a), (b), (c), (d)} correspond to $\beta_{\text{MAX}} = \{20, 15, 10, 2\}$ degrees.

phase center is aligned with the aperture plane. The latter property is particularly relevant for the front-to-front coupling of the back-facing and PSB feedhorns across the thermal gap, as it minimizes the axial separation of the phase centers in the absence of lenses in the filter stacks.

The exact profiling can take a number of functional forms with little practical difference in performance in the end, as long as the flare angle varies adiabatically. The profile used for the inner radius a is:

$$a(z) = a_{\text{THROAT}} + \left(a_{\text{APERTURE}} - a_{\text{THROAT}}\right)\left(\left(1 - A\right)\frac{z}{l} + A\sin^2\left(\frac{\pi z}{2l}\right)\right) \tag{2.5}$$

where z is the axial dimension, l is the length of the flare section, and $A = 0.7$ modulates the degree of linearity and is determined by trial-and-error for reasonable performance and design solutions.

A useful metric for the aggressiveness of designing for compactness is the maximum allowed flare angle β_{MAX}. Figure 2.7 shows calculated far-field patterns for four different 100 GHz primary horn
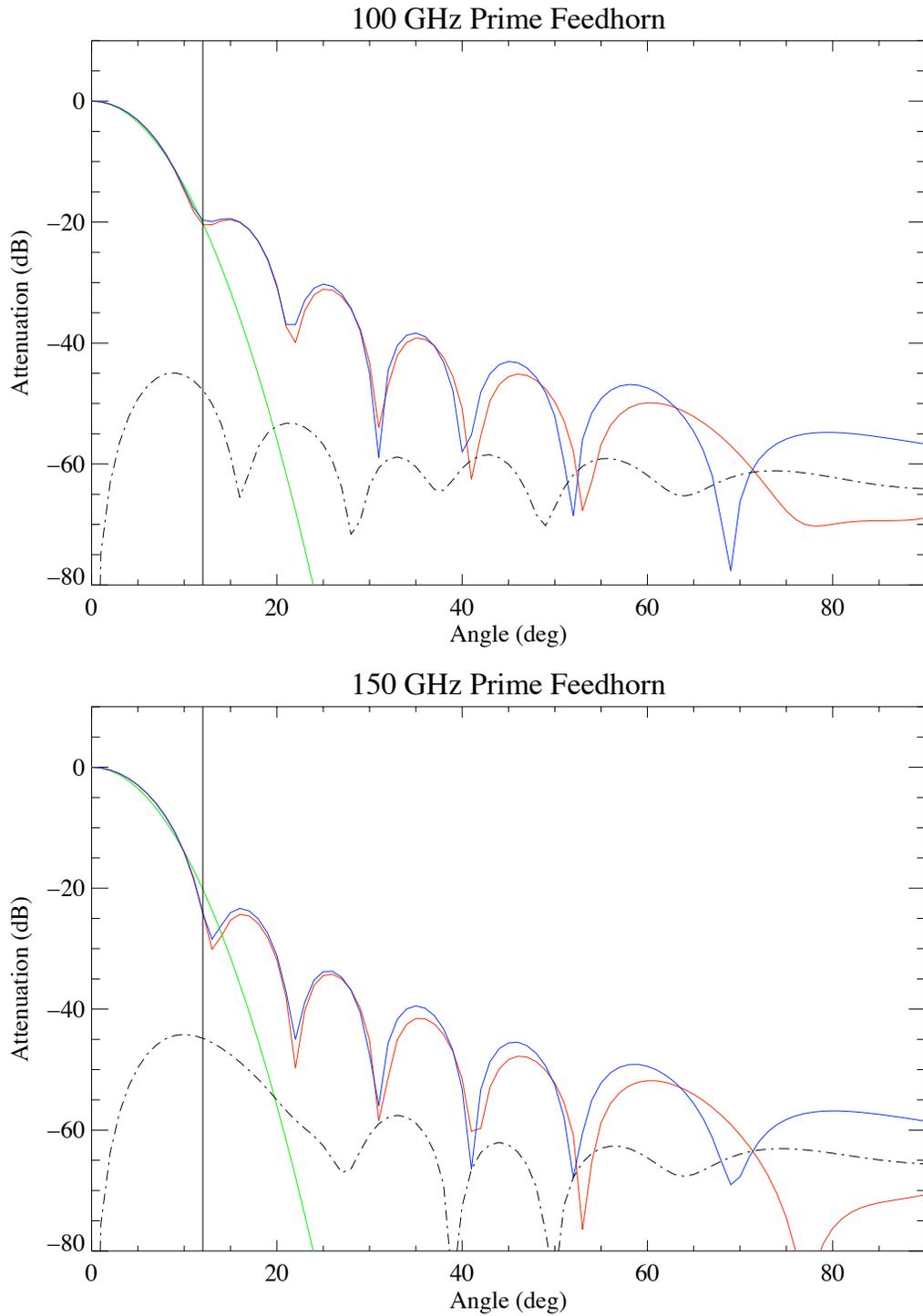
Figure 2.8: Simulated far-field patterns of the primary feedhorns using modal matching. The red and blue patterns correspond to the E- and H-plane cuts of the beam pattern; the dotted pattern corresponds to the cross-polar beam at 45° from vertical polarization. The green profiles are equivalent pure gaussian beams. The approximate aperture stop is indicated by the vertical line.

designs, identical except for the lengths of the flare sections which directly determine the maximum angles. In this context where the feedhorn beams will be coupled to a −20 dB aperture stop, the trade-off is essentially between compactness and directivity. The design corresponding to (c), or $10°$ maximum flare, was chosen as a compromise offering good aperture efficiency and reasonable ease of manufacturing. The length of the 150 GHz primary feed is simply matched to that of the 100 GHz, giving $6.5°$ maximum fare.

The field distribution at the aperture of the primary horns (Equation 2.4) not only results in excellent performance characteristics for polarimetry, but is also convenient for simplified gaussian optics calculations since ~98% of the power is in the fundamental gaussian mode. This maximum coupling efficiency is achieved for $w_0/a_{\mathrm{APERTURE}} = 0.644$, where w_0 is the gaussian beam waist radius coupling to the feedhorn aperture. This approximation of the propagation of beams was used in aiding the design of the HDPE lenses.

The predicted far-field beam patterns for the primary feedhorns (calculated with the CORRUG software[6]) are shown in Figure 2.8, with the main aperture taper at the objective lens shown by the vertical line at ~$12°$. Although detailed radiation pattern measurements were not carried out for all the feedhorns, past experiences with other systems have indicated very good agreement between the modal-matching calculations by CORRUG and physical measurements. Return loss measurements using a vector network analyzer were carried out, however, to identify individually flawed feedhorns, and a small number of these were replaced prior to full system integration.

2.5 Spectral band definition

BICEP's two frequency channels at 100 GHz and 150 GHz are designed to coincide with windows in the Earth's atmospheric opacity, and enable discrimination against non-thermal foreground sources such as the galactic dust and synchrotron emissions. With the lower edges defined by the corrugated waveguide cut-ons, the upper edges are provided by stacks of capacitive metal mesh low-pass filters at the aperture of the PSB feedhorns, heat-sunk and cooled to 250 mK. Multiple layers of metal meshes are supported on a dielectric substrate for each individual filter, and AR-coated to minimize loss.

---

[6]Antenna Software Ltd., UK. Web: http://www.maasdesign.co.uk/
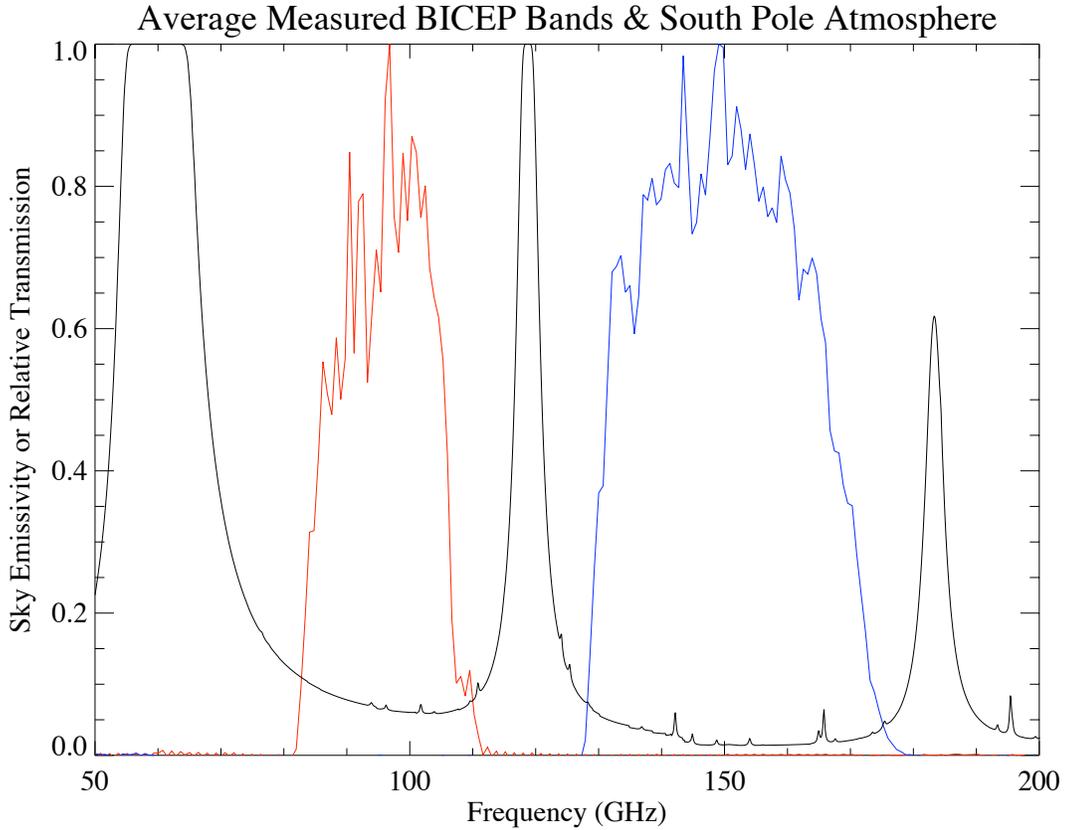
Figure 2.9: Average measured BICEP spectral bands.

Correctly tuning the locations of both the waveguide cut-ons and the metal mesh profiles requires reasonable estimates of the atmospheric emission and expected performance of the receiver. Given an atmospheric model the bandwidth and band-center of both channels can be optimized for sensitivity to CMB. The detailed treatment of the optimization procedure is explained in Appendix A; the salient results are summarized here.

Figure 2.9 shows the expected South Pole atmospheric model appropriate for winter conditions at the expected elevation of observation ($\sim 60°$), calculated with the AT software[12], along with average measured spectral passbands of both channels prior to deployment. Rigorous optimization of the spectral bands can become quite involved, requiring not only accurate atmospheric/instrument models, but also knowledge of operational choices such as sub-Kelvin focal plane temperature and detector biasing which may not be precisely determined until a working instrument is available.

In reality — due to the intrinsic uncertainties in the atmospheric modeling, complex dynamic

	Edge Filter (cm^{-1})	Blocker 1 (cm^{-1})	Blocker 2 (cm^{-1})
100 GHz	"B829" 3.65	"B822" 4.00	"B657" 6.60
150 GHz	"B647" 5.90	"B807" 5.77	"B712" 8.50

Table 2.5: Nominal metal mesh filter edges and serial numbers.

behavior of the South Pole weather, long lead times involved in developing and testing prototype metal mesh filters, *etc.* — more guesswork is involved in the so-called "band-optimization" than one might be led to believe! Rough locations for the band edges for high sensitivity are readily apparent even without rigorously detailed calculations, however. Assuming a simple top-hat spectral band and realistic estimates of the end-to-end optical efficiency is adequate enough to narrow the optimization phase space to a small range. In particular, since the waveguide cut-ons that define the lower edges of the bands can be reliably predicted and expected to be sharp, these were fixed early in the design cycle as explained in Section 2.4, leaving just the profile of the metal mesh low pass filters to be optimized, fabricated and tested iteratively.

Most critical to the experiment is the upper edge definition of the 150 GHz band, as it is bound by the strong water emission at ∼183 GHz, which is highly variable with weather conditions. The lower edge of the 150 GHz band and the edges of the 100 GHz band are bound by oxygen emission lines which are stable, and these can be optimized using a static model of the atmosphere. Although a detailed dynamic model of the atmosphere can be attempted to optimized the 150 GHz band — taking into account both the spatial and temporal fluctuations specific to the observing site — in the end Bicep conservatively used filter designs with edge profiles similar to the proven earlier-generation designs in ACBAR, but with better cut-off performance in further limiting the water contribution to the total loading.

Typically, these filters exhibit spectral leaks at multiples of the cut-off frequency (3.65 cm^{-1} and 5.9 cm^{-1} respectively for 100 GHz and 150 GHz bands). Two additional metal mesh filters at higher cut-offs are used at each pixel to efficiently block out these leaks. Testing with thick grille filters indicates an upper limit of high frequency leak at −25 dB for 100 GHz pixels and −30 dB for 150 GHz pixels. Limiting the high frequency leaks are crucial: as well as introducing unpredictable excessive optical loadings and potential spectral mismatches within a pair, there is little guarantee that the

resulting beams on the sky corresponding to the leaks will be well-behaved, either in profile or in polarization purity. Theses results are given in more detail in Section 3.2.

2.6 Faraday rotation modulators

Six of the 49 pixels deployed for this first season of observation were employed as testbeds for Faraday rotation modulators[19] (FRM), operated as polarization switches in a phase-sensitive detection scheme between the primary and back feed horns. Such modulation in principle offers the ability to minimize susceptibility to systematic instrumental polarization, tune the post-detection audio band for more flexibility in avoiding microphonic lines, and mitigate optical sources of systematic polarization such as differential gain fluctuations. Modulation increases the system's immunity to offset variations downstream of the primary feed horns.

The FRMs are functionally similar to a rotating birefringent half-waveplate, but have no moving parts and are implemented at the back-to-back feed horn section of each pixel. Modulation is achieved using the Faraday effect, whereby the plane of linearly polarized radiation is rotated during propagation through a magnetized dielectric. A superconducting solenoid, biased with ±0.1 A, produces ±45° rotation, allowing measurement of the Q Stokes parameter with a single PSB without the need for pair-differencing.

Rotation angle has been measured to be uniform across both of the optical bands and is extremely stable over time. At the time of the initial deployment, FRM performance met desired design criteria: ∼ 80% transmission, ∼ 1% reflection, ∼ 1% instrumental polarization, < 1% cross polarization, > 90% polarization efficiency, and < 1 mW *r.m.s.* total power dissipation.

However, because of the large difference in instrument operating modes between pair-differencing of simple scan-modulated signals (requiring a relatively fast mount scanning speed to place the target science range of $\ell \sim 30$–300 sufficiently above the $1/f$ knee of the atmosphere) and FRM-modulated scheme (requiring relatively slow scanning for effective and accurate amplitude demodulation of the incoming polarization), along with the good performance of the former method of pair-differencing in nulling out the common-mode fluctuations over a wide enough bandwidth, led us to remove the FRMs at the end of the first season and commit to scan-based modulation of the signal.

2.7   Polarization-sensitive bolometers
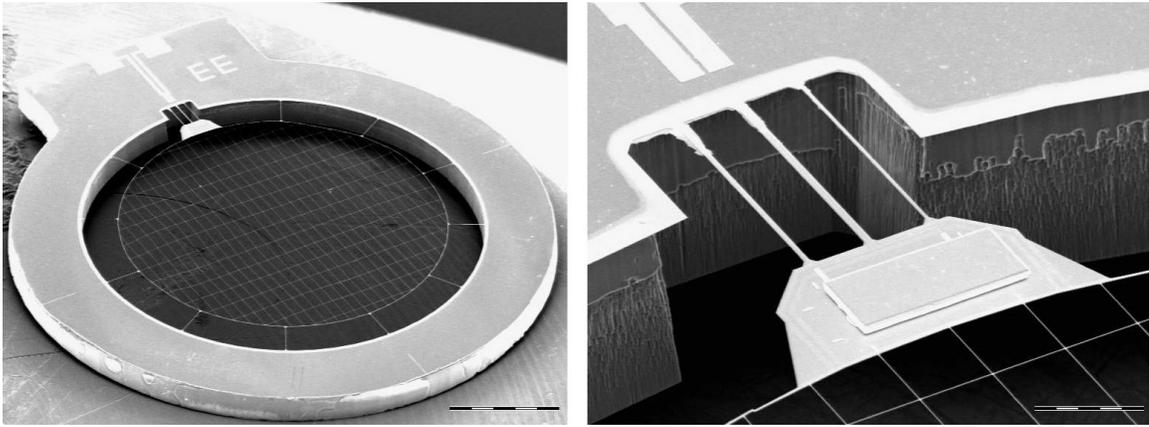
Figure 2.10: A Bɪᴄᴇᴘ Si$_3$N$_4$ PSB prior to being mounted and wirebonded in its module housing. Only the longitudinal legs are metalized for polarization sensitivity, and spaced at 150 μm for operation in both 100 GHz and 150 GHz bands. The metalized and trimmable pair of legs adjacent to the signal leads allows for custom tuning of the thermal conductance to the 250 mK bath, depending on expected total loading on the bolometer.

Bɪᴄᴇᴘ uses a pair of silicon nitride micromesh polarization sensitive bolometers[17] (PSBs) at each pixel location, orthogonal in polarization orientations and co-mounted behind shared feeds and cold band-defining filters. A total of 49 such pairs, 25 at 100 GHz and 24 at 150 GHz, are cooled to 250 mK to achieve close to background-limited sensitivities. After adjusting for the relative responsivities, the pairs are summed or differenced to measure the Stokes I or Q parameters. Because the orthogonal PSBs observe the CMB through the same optical path and atmospheric column with near-identical spectral pass bands, systematic contributions to the polarization are greatly minimized.

Due to its wide intrinsic bandwidth, the same micromesh bolometer design can be used for both 100 GHz and 150 GHz band, in detector housings tuned for band-specific $\lambda/4$ backshort integrating cavities and appropriate mating to the corrugated PSB feed horns. Figure 2.10 shows a typical Bɪᴄᴇᴘ PSB prior to being mounted. The optically active absorber mesh area is 4.5 mm in diameter, metalized along the vertical direction to couple only to a single polarization mode, and suspended along the perimeter by low thermal conductance support legs. A neutron transmutation-doped germanium (NTD Ge) thermistor is mounted at the edge of the absorber, placed outside the coupling area to the incoming guided wave to minimize crosspolar response.
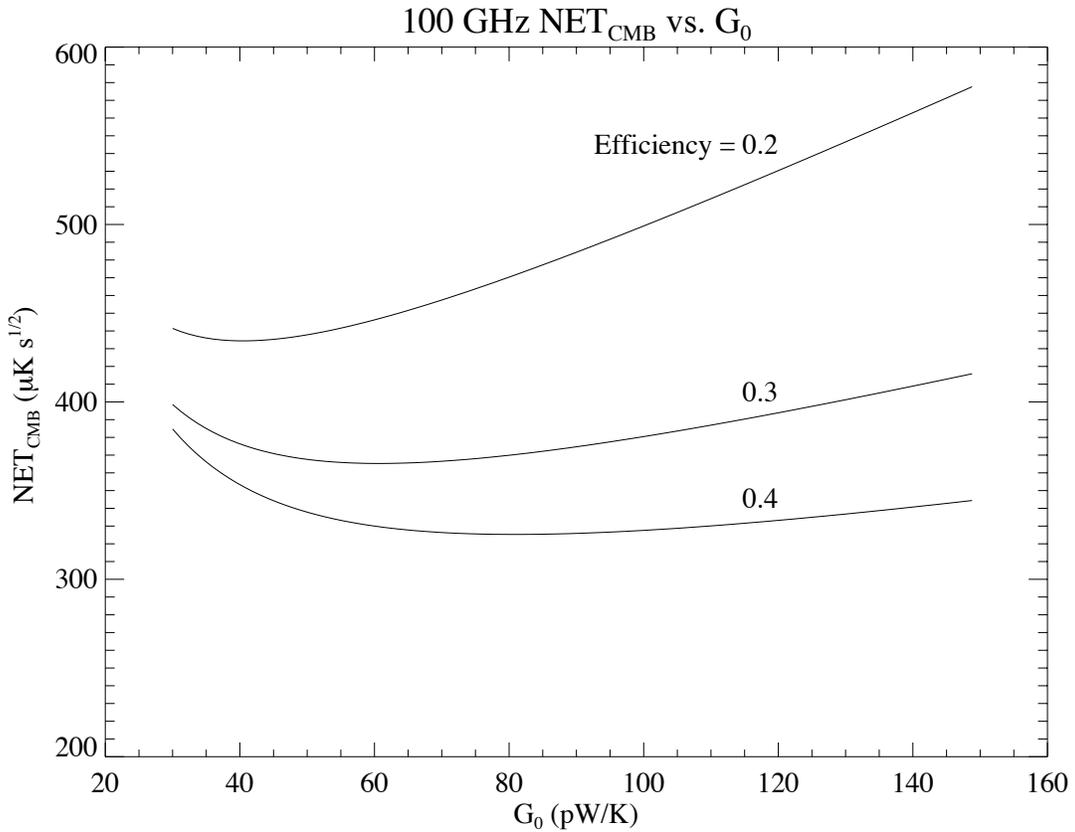
Figure 2.11: 100 GHz NET$_{\text{CMB}}$ vs. G_0, for optical efficiency $\eta = \{0.2, 0.3, 0.4\}$

Properly tuned, NTD Ge bolometers can offer background photon noise-limited sensitivity in low loading conditions.[4] The thermal conductance $G(T) = (T/T_0)^\beta$ between the thermistor and the 250 mK bath is tailored for the expected total loading to limit phonon noise. (T_0 = 300 mK by convention.) The conductance of the BICEP PSBs is dominated by the signal leads and a pair of adjacent metalized legs, which can be laser-trimmed to change the final conductance to $\{40, 50, 67\}\%$ of its full value.

At relatively high end-to-end optical efficiencies (and thus higher fractional photon noise contribution), a wide range of G_0 is acceptable for low-noise performance. But as the optical efficiency becomes degraded, the thermal conductance must be appropriately adjusted for maximum sensitivity (Figure 2.11). Prior to deployment, the PSBs for both bands were adjusted to a target value of $G(T = 300 \text{ mK}) \approx 60$ pW/K by trimming both of the adjustment legs, based on achieved optical efficiency during testing, and expected atmospheric loading projected for observing conditions.
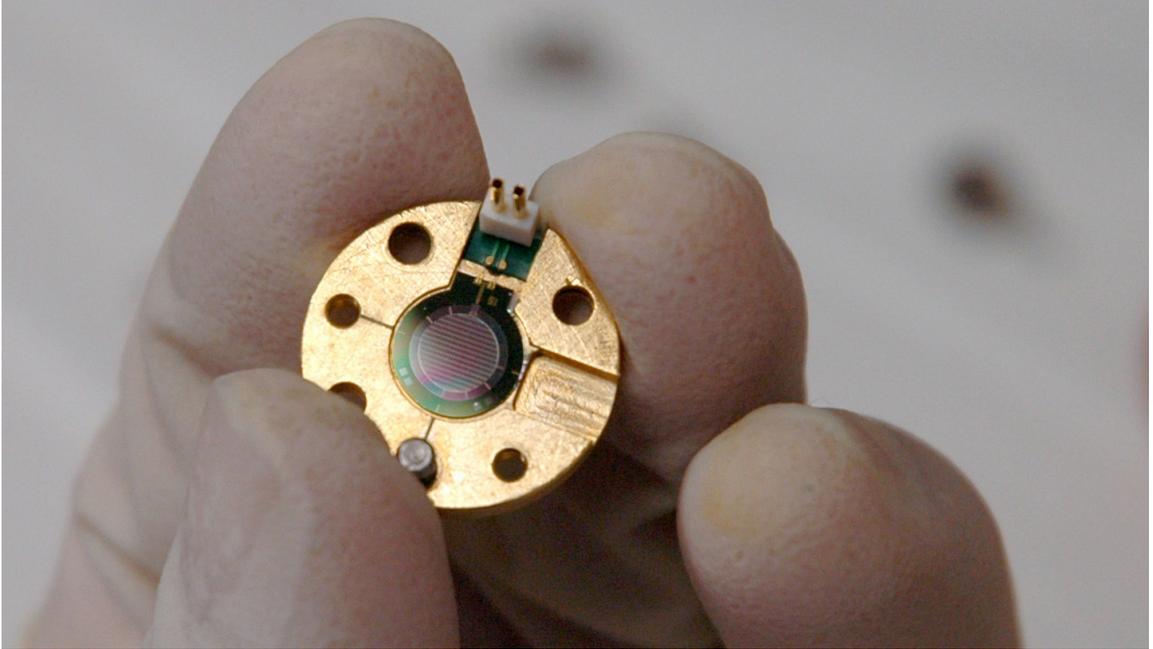
Figure 2.12: Un-etched PSB mounted into a Bicep module to be used as a thermistor, prior to being mated with its pair and installed into the focal plane. Alignment pins register the polarization orientation both within a pair and *w.r.t.* the focal plane.

The optical time constant $\tau \sim C/G$ determines the maximum desirable scanning speed $v_{\text{MAX}} \approx \theta_{\text{FWHM}}/3\tau_{\text{MAX}}$. Single-pole equivalent median τ was measured to be ~ 21 ms, with 97% of the PSBs under 45 ms. This allows for azimuth scanning at up to 5 deg/s without significant signal roll-off. Typically, the beams move across the sky at 1–2 deg/s over the elevation range of the observed field, safely within the limit set by time constant roll-off considerations. Measurements of the bolometer transfer functions and model fits to time constant values are detailed in Section 3.5.

PSBs have been used for a number of experiments. Detectors similar in design were used in the 2003 flight of Boomerang at 145 GHz,[30] providing the first bolometric measurement of CMB polarization. PSB modules identical to the ones described here have been deployed in QUAD,[6] targeting CMB polarization at angular scales an order of magnitude smaller than Bicep's range. In addition, the HFI instrument of the upcoming *Planck* mission will incorporate eight PSBs (4 feeds) at each of 143, 217, and 353 GHz. The PSB concept derives from previous generations of total intensity Si_3N_4 micromesh bolometers,[5] used in numerous measurements of the temperature anisotropy (ACBAR, *Archeops*, Bolocam, Boomerang 98, MAXIMA and MAXIPOL).

2.8   Helium sorption refrigerator
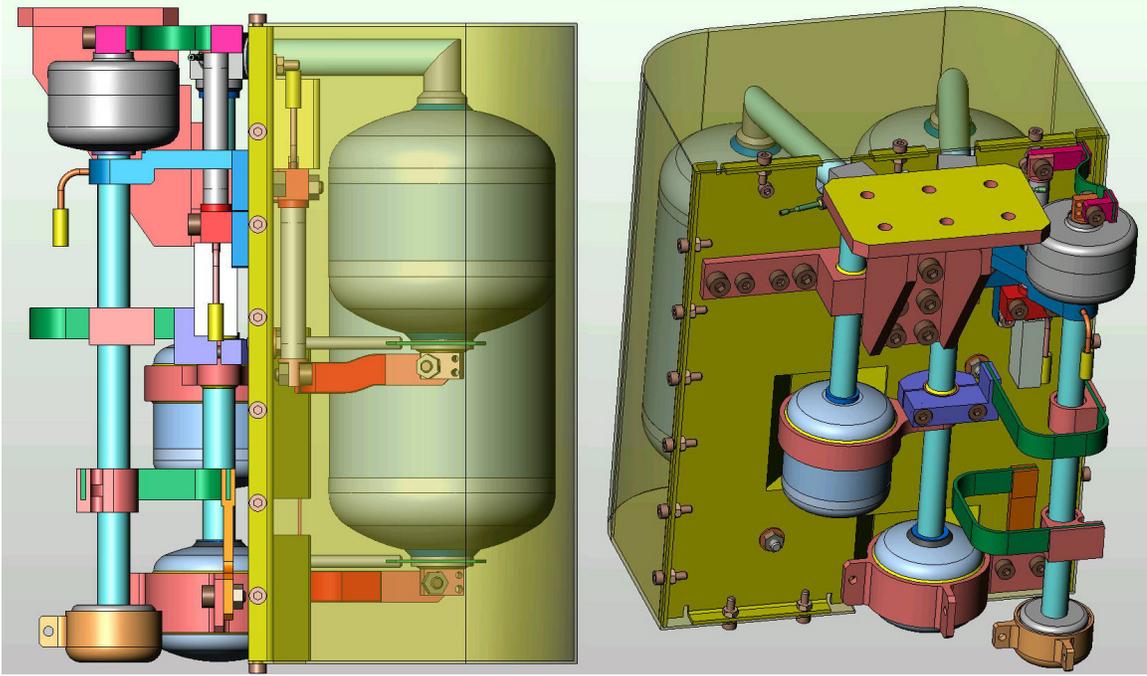
Figure 2.13: Diagram of the multi-stage sorption refrigerator, showing the pump and evaporator of each stage (4He, 3He InterCooler, and 3He UltraCooler). The large 4He and 3He IC sorption pumps are cooled by gas-gap heat switches and housed in a light-tight shield. The small 250 mK stage UC pump is separately shielded (shield not shown). The sorption unit mounts to the main LHe tank by a copper flange (4 K contact), which connects directly to the 4He condensation point.

The detector focal plane is cooled to 250 mK by a 3-stage 4He/3He/3He sorption refrigerator filled with $\{32, 16, 2\}$ L (STP) of gas, respectively. This design eliminates the convection found in previous multi-stage designs[3] during the condensation phase[10] by putting several bends in the pump tube between the pump and the condensation point (see Figure 2.13). The fridge requires $\{4.68, 1.62, 0.41\}$ kJ to cycle the pumps with a power dissipation of $\{70, 60, 60\}$ mW to sustain the pumps at the end of the condensation phase. A similar design was used to reduce the parasitics on an adiabatic demagnetization refrigerator and a large suspended focal plane in the Z-Spec instrument.[33]

To reduce additional load on the focal plane from the un-pumped main LHe bath, we employ a thermal intercept stage in the focal plane connected to the 4He evaporator. This stage maintains 1.4 K while the 4He lasts, and 2.4 K after the 4He is exhausted, still cooled by the 3He vapor of the

second stage (inter-cooler, or IC) and intercepting ~ 30 μW of parasitic heating from the 4 K bath.

The cycling of the refrigerator is entirely automated via the control system, and requires ~ 5 hours to reach 250 mK from the 4 K starting point. The hold time from the start of the cycle is ~ 65 hours, limited by the 3He IC stage running out. In normal operation the refrigerator is cycled every 48 sidereal hours at the beginning of each observation schedule, providing an operating temperature duty cycle of 89%.

The hold time is ultimately driven by the capacity of the IC stage, which is in turn largely determined by the hold time of the 4He first stage — before it is exhausted the parasitic thermal loading on the IC is small. The third stage (ultra-cooler, or UC) which provides the actual working temperature of the focal plane has a capacity beyond the requirements for normal operation, and does not affect the total hold time.

All three evaporators of the fridge are linked to the focal plane at various isolated stages with solid OFHC Cu thermal straps which are braced with insulating and/or isothermal supports to guard against vibrational heating.

2.9 Sub-K focal plane

The focal plane is arranged in a six-fold symmetric pattern, as seen in Figure 2.14. As deployed for the first season, each hextant contains four pixels at each of the two frequency bands. The central 100 GHz pixel is read out by one of the six hextants, accounting for a total of 96 + 2 light bolometers. Additional readout channels provide for one pair of 5 MΩ resistors, dark bolometers, and high sensitivity NTD thermistors in each hextant for diagnosing systematics.

A PSB pair can be installed in either boresight "Q" or "U" orientation on the focal plane, defined with respect to the radius from the center. With a few exceptions during the first season to accommodate the FRM test pixels, the orientations alternate between the two in adjacent hextants, such that upon odd-multiple 60° rotation of the instrument about the boresight, we achieve complete parity in Q/U coverage on the sky.

A PCB fan-out board on the backside of the detector focal plane routes the individual PSBs of each hextant to the six load resistor modules (LRM) on the perimeter for readout by the JFET amplifier
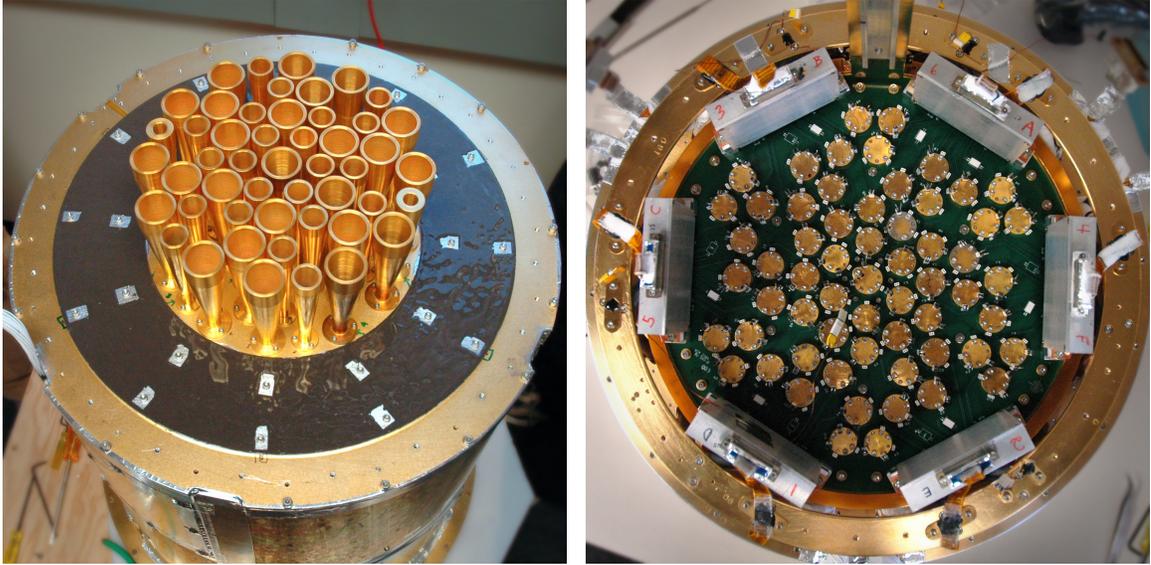
Figure 2.14: 4 K and 250 mK focal plane. The 4 K focal plane as shown reflects the addition of two 220 GHz pixels at the beginning of the second year of observations.

stage. The entire focal plane, from the 4 K back-to-back throat section down to the output of the JFET modules, resides within a tightly-sealed Faraday cage, eliminating any stray radiation coupling to the bolometers.

The sub-Kelvin focal plane is thermally isolated from the 4 K base temperature by a series of Vespel trusses and thermal intercept stages, and hung off from the 4 K back-to-back feed horn plate such that the complete focal plane — from the primary feedhorns down to the PSBs — form a single modular unit that can be detached easily from the rest of the receiver insert (Figure 2.15).

The thermal engineering of the truss system is designed to optimize the total hold time of the sub-Kelvin fridge cycle given expected parasitic loadings on the multiple stages of the fridge. In addition to the 250 mK UC stage, the fridge provides two buffer stages at the IC and 4He stages. To achieve adequate hold time for multiple days of operation, it was determined that the loading onto the IC stage must be kept to within ~ 25 μW.

The Vespel support structure makes use of two flavors of the material, SP1 and SP22, for different temperature ranges. In addition we must also consider the properties of the manganin signal read-out wires for the thermal engineering of the support structure. The thermal conductivities of the three material can be described by $\kappa = \kappa_0 (T/\mathrm{Kelvin})^n$; Figure 2.16 compares the conductivities over
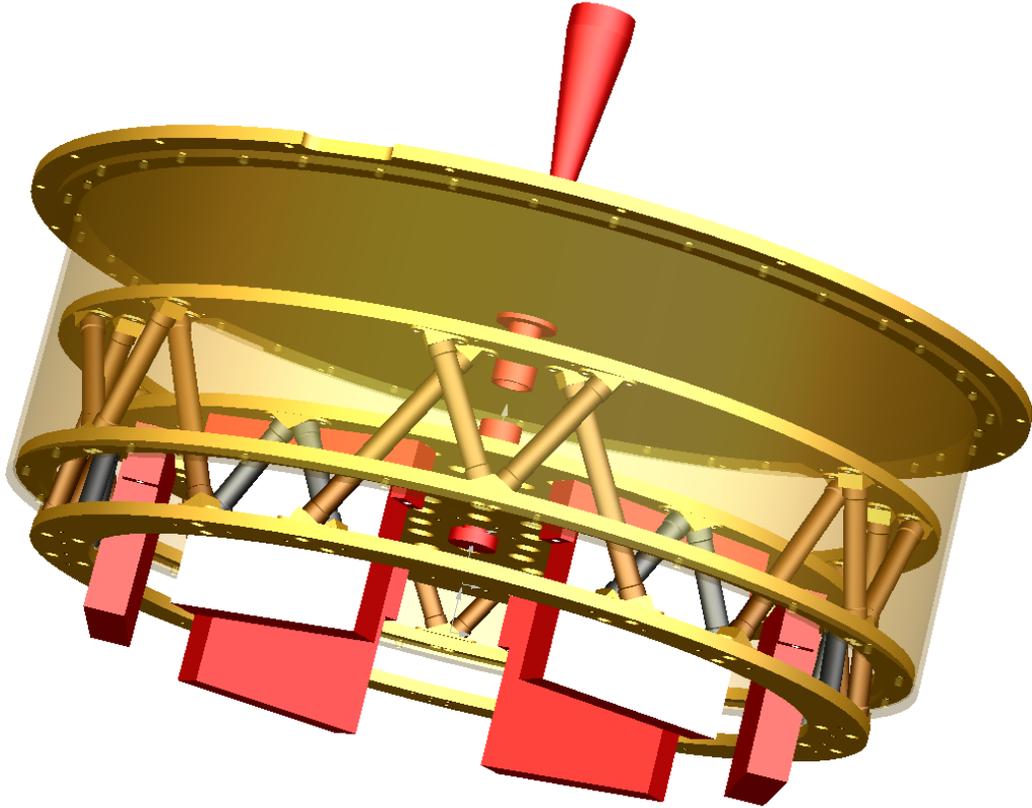
Figure 2.15: Thermal isolation Vespel truss structure. Different flavors of the material are used as appropriate for optimal thermal properties at each thermal isolation stage. The legs shown in black represents Vespel SP22.

the temperature range of interest, and Table 2.6 shows the integrated conductances over the expected temperature differences. The graphite-doped SP22 holds an advantage over SP1 at sub-Kelvin temperatures, and is used for the trussing between the focal plane and the IC intercept ring (inner-most trussing in Figure 2.15). SP1 is used between the IC intercept and the vapor-cooled 4He intercept rings, and between the 4He intercept and the 4 K focal plane support cylinder.

Given these numbers, then, we can work out the maximum allowed geometric aspect ratios of the support legs that meet the required thermal loading on the IC stage. The instrument is operated in two distinct but regular fridge phases: prior to the 4He stage running out, the equilibrium stage temperatures for {UC, IC, 4He} are {0.25, 0.30, 1.4} K, subsequent to the 4He stage becoming exhausted, the equilibrium temperatures are {0.25, 0.38, 2.4} K. The expected loading on the IC stage in the first phase is ~ 5 μW; during the second phase, this rises to ~ 17 μW. In both cases the Vespel
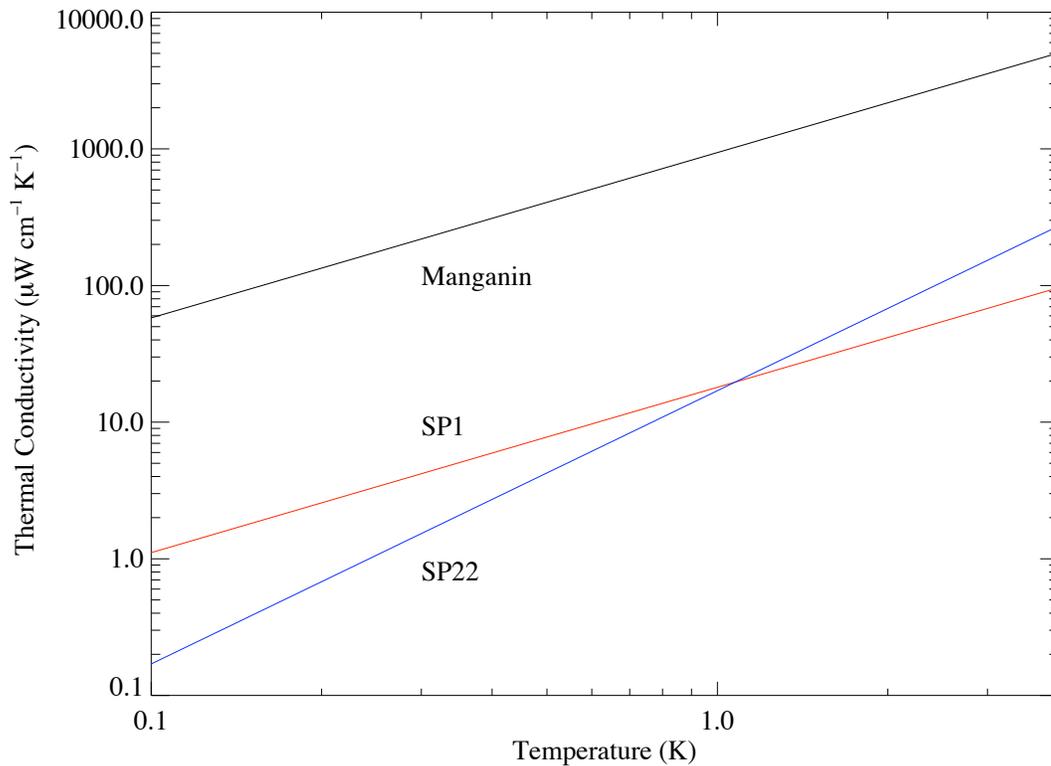
Figure 2.16: Thermal properties of manganin and Vespel.

legs account for ∼70% of the loading.

At sea-level testing conditions where the LHe base temperature is higher, the loading on the IC stage is expected to be near the specified limit of 25 μW. (At the South Pole, LHe temperature is 3.8 K.) The operational advantage of the high-altitude South Pole is thus significant, increasing the total useful hold time from ∼40 hours to ∼60 hours, excluding the cycling time itself.

Despite the relatively large mass of the sub-Kelvin focal plane (∼ 5 kg) the canted Vespel legs are robust against any measurable deflection even at large deviation from vertical orientation of the cryostat, and there is no evidence of deflection-mediated modulation of the optical coupling at the front-to-front thermal gap between the PSB and back feedhorns.

2.10 Signal electronics

The readout electronics system uses digitally-generated AC bias current, cold JFETs, analog pream-plifiers, and digital demodulators. The behavior of the bias generator and digital electronics can be

	$\kappa_0\ (\mu\mathrm{W/cm\,K})$	n	$\sigma_{0.38-0.25}$	$\sigma_{2.4-0.38}$	$\sigma_{3.8-2.4}$
Vespel SP1	18.0	1.21	0.58	55.4	99.3
Vespel SP22	17.0	2.00	0.22	78.0	233
Manganin	940.0	1.20	30.6	288	5130

Table 2.6: Properties of Vespel and manganin used in the thermal design of the focal plane support structure, and integrated conductances for measured ΔT's (as specified in the subscripts). The σ's are given in μW/cm.

changed on demand from the control software, enabling, for instance, DC mode operation for measuring load curves.

A sinusoidal 100 Hz AC bias current, applied symmetrically across 2×20 MΩ load resistors to minimize common mode pickup, eliminates $1/f$ electronics noise above 10 mHz. The quasi-stationary optical signals can then be recovered using synchronous demodulation of the AC signals. The bolometer bias is produced by a highly stable, digitally-controlled sinusoidal waveform synthesizer capable of varying the bias frequency from 100 to 200 Hz.

The bolometer readout front end consists of cold JFET amplifiers operated at ~ 120 K, mounted to the 4 K baseplate and connected to the 250 mK LRM via low thermal conductivity manganin twisted-pair cables.[7] The JFETs are necessary to amplify the signal from high impedance bolometers and protect the bolometer from EMI. Three JFET modules (developed originally for the Herschel/SPIRE instrument) with two sets of membranes each service the six hextants, dissipating a total of 45 mW at 4 K. The best 24 channels out of 30 available are selected from each membrane, achieving an average voltage noise contribution of 7 nV/$\sqrt{\mathrm{Hz}}$. The output of the JFET modules exits the 4 K Faraday cage through RF-filtered connectors.

Upon exiting the cryostat, the signal is routed inside an RF-tight cage to the room-temperature preamplifiers, each equipped with a commandable high pass filter for AC bias mode operation. The preamplifier output is then anti-alias filtered and exits the "clean" electronics through RF-filtered connectors to be digitized synchronously with the bolometer bias. In AC bias mode, the digitized signal is multiplied by synchronous sine and cosine, averaged and filtered by a gaussian digital finite impulse response filter in a low power mixed signal processor. In DC bias mode, the digitized signal is instead multiplied by ± 1. This allows for the demodulator transfer function to be measured by

---

[7]Tekdata Interconnect Systems, Staffordshire, ST6 4HY, UK. Web: http://www.tekdata-interconnect.com/
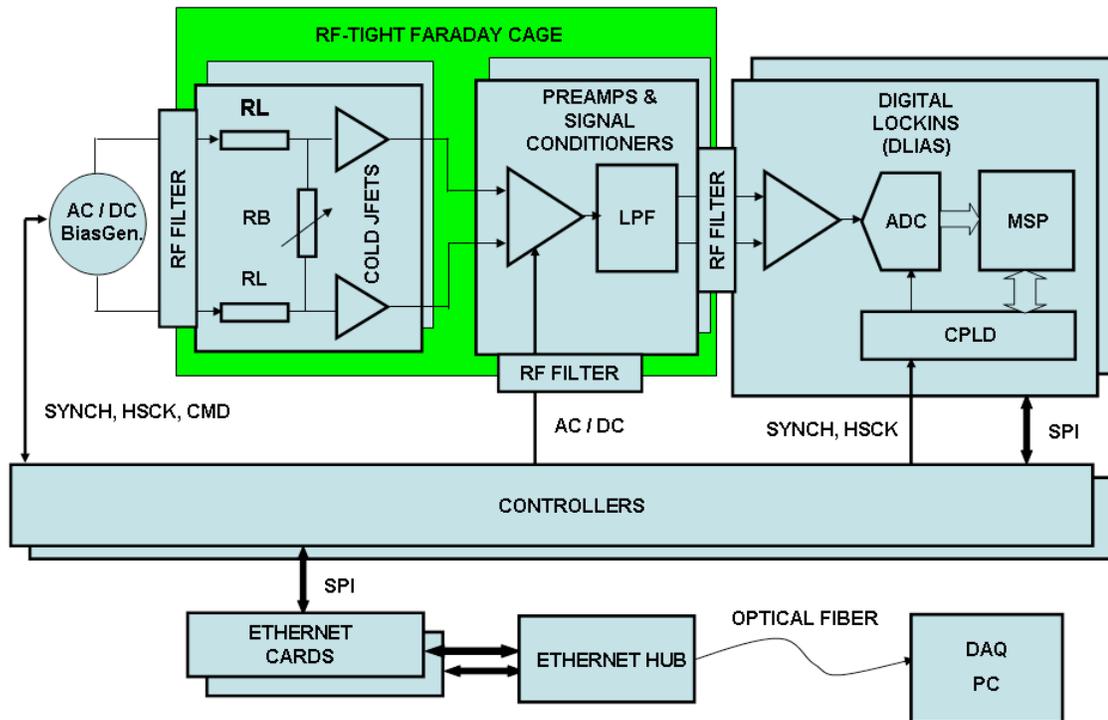
Figure 2.17: Read-out electronics diagram.

applying a delta function in DC test mode, if needed.

The demodulated sine and cosine signals from all the bolometers are packaged onto an ethernet bus, converted into an optical fiber signal and sent to the acquisition computer. The optical fiber data are routed through the central section of a pair of slip rings[8] to allow for unimpeded boresight rotation of the cryostat.

2.11 Telescope mount

The telescope mount addresses the requirements of reliable winter-over operation at the South Pole by enclosing all serviceable components of the system except for the receiver window itself within an easily accessible shirt-sleeve environment. Its unique design, illustrated in Figure 2.18, accomplishes this while allowing steering and tracking of the telescope through a full range of motion in azimuth (400°), elevation (50–90°), and continuous rotation about the boresight, or theta axis.

---

[8]Moog Components Group, Blacksburg, VA 24060. Web: http://www.polysci.com/
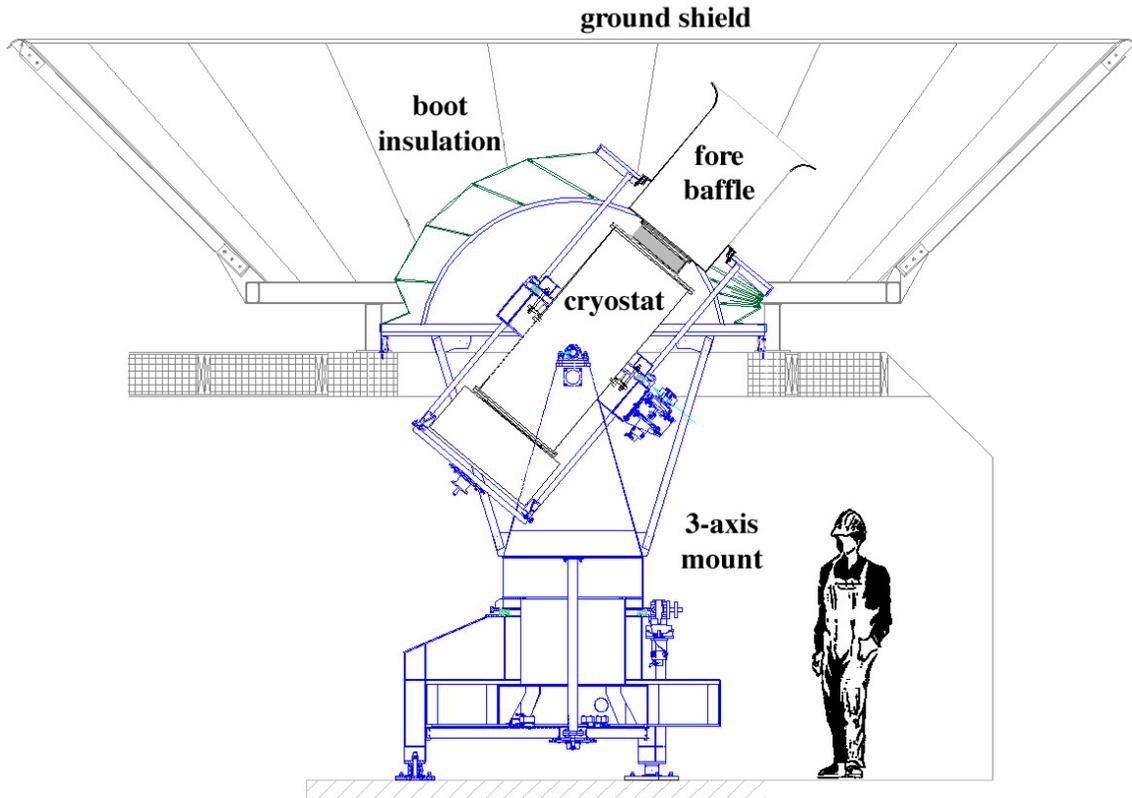
Figure 2.18: The three-axis telescope mount, cryostat, and ground shield as installed on site. The entire cryostat and the receiver electronics reside inside the DSL building, with only the optical aperture and the forebaffle exposed to the elements. A flexible and co-rotating "boot" insulation allows for unhindered movement of the telescope.

The mount is situated in the upper floor of the new Dark Sector Laboratory (DSL), 0.8 km from the geographic South Pole. An insulated fabric bellows permits motion in the elevation axis, and together with double brush seals at the azimuth and theta axes forms an environmental seal between the rooftop of the building and the front of the receiver which maintains the space around the cryostat, control electronics, and drive assemblies at room temperature. The enclosed observatory space is kept at a slight positive pressure, so that a constant outward airflow through the brush seals and special vents directed toward the window eliminates ice buildup there.

The Bicep mount was engineered and fabricated in conjunction with TripointGlobal/VertexRSI.[9] Lightweight box steel construction lends the mount extreme rigidity and immunity to flexure; the combined weight of the telescope, when fully equipped and operational, is approximately 7500 lbs. It

---

[9]VertexRSI, Kilgore, TX 75662. Web: http://www.tripointglobal.com/

is supported on a steel and wood platform attached to the structural beams of the building. Continuous tilt monitoring and periodic star pointing have confirmed short term stability and blind pointing accuracy of the combined mount/platform structure to meet our pointing spec of $< 20''$. Long term drifts at the level of $\sim 1'$/month appear to be dominated by settling of the building.

The mount allows rapid scanning, up to 5 deg/s, about the azimuth and/or theta axes while maintaining precise pointing and producing minimal vibration. These axes employ ultra-quiet crossed roller bearings[10] and gearless cycloidal motor reducers.[11] Integrated testing with the BICEP receiver drove a choice of toothed belt drives[12] for the azimuth and theta axes, which further reduced high drive speed microphonic excitation to levels well below our detector noise floor.

2.12 Optical star camera

BICEP aims to achieve overall pointing accuracy better than 1% of the beam size to limit contamination to the B-mode polarization. This requires a precise knowledge of the dynamic state of the mount, including flexure, axis tilts, and encoder offsets. To aid in the pointing reconstruction, we have built an optical star-pointing refractor camera with a $2''$ resolution, mounted adjacent to the main optical window and co-aligned with the boresight rotation axis.

Since there are ten dynamic parameters (including the collimation error of the pointing telescope itself), a complete calibration requires observation of at least 20 stars. To be able to establish a pointing model during the Antarctic summer, the camera was designed to be sensitive enough to detect magnitude 3 stars in daylight. For maximum contrast against the blue sky, a sensor with enhanced near-IR sensitivity is used with an IR72 filter.[13]

The 100-mm diameter lens, color-corrected and anti-reflection coated for 720–950 nm, was designed by Anthony Stark of the Smithsonian Astrophysical Observatory for the South Pole Telescope (SPT). Its 901-mm focal length results in a small $0.5°$ field of view. Careful adjustments of the CCD camera and the mirrors reduced the star camera's collimation error to $2.4'$. During the austral summer season prior to the first season of observations, we were able to successfully capture stars down

---

[10]ROLLON Corp., Sparta, NJ 07871. Web: http://www.rollon.com/
[11]Gates Mectrol Corp., Salem, NH 03079. Web: http://www.mectrol.com/
[12]TB Wood's Inc., Chambersburg, PA 17201. Web: http://www.tbwoods.com/
[13]Astrovid StellaCam EX CCD — AVA Astro Corp., Hudson Falls, NY 12839. Web: http://www.astrovid.com/
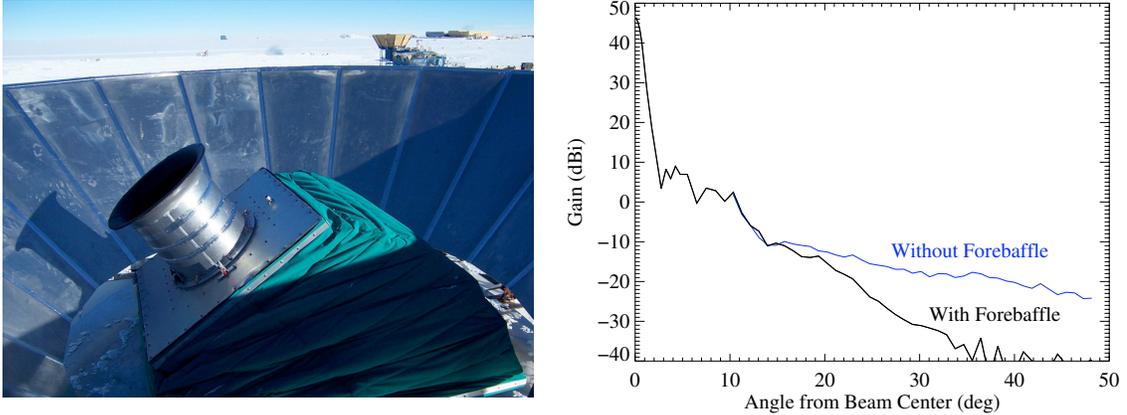
Figure 2.19: Absorptive forebaffle and fixed groundscreen as installed on-site (*left*), and sidelobe rejection performance as measured for the central pixel (*right*).

to magnitude 2.8 for initial pointing calibration.

2.13 Groundscreen & forebaffle

We use two levels of shielding against ground radiation contamination: an absorptive forebaffle fixed to the cryostat and a large reflective screen fixed to the roof of DSL. The geometry of the shielding is such that any ground radiation must be diffracted at least twice before entering the window in any telescope orientation during operation.

The forebaffle is an aluminum cylinder lined with a microwave absorber to minimize reflected radiation into the telescope. It is sized to clear the sidelobes of the edge pixels, and long enough so that the window will never directly see either the outer ground screen or that of the proposed SPT adjacent to the BICEP facility. The dimension of the forebaffle also prevents moonlight up to $21°$ elevation from entering the window directly. The Moon is above this elevation 5 days a month. The forebaffle's aperture lip is rounded with a 13-cm radius to reduce diffraction.

After testing many materials for the absorber, we chose a 10-mm thick open-cell polyurethane foam sheet,[14] which had the lowest measured reflectivity (< 3%) at 100 and 150 GHz when placed on a metal surface.[29] To prevent snow from accumulating on the porous Eccosorb foam, it is lined with 1.6-mm thick smooth Volara polyethylene foam. The combined Eccosorb HR/Volara stack was

---

[14]Eccosorb HR — Emerson & Cuming, Randolph, MA 02368. Web: http://www.eccosorb.com/

measured to reflect ~ 5% at 100 GHz. In addition, a self-regulating heat cable is wrapped around the outside of the baffle to sublimate any snow on the baffle surface, if necessary.

The additional loading on the bolometers due to this forebaffle was measured to be ~ 1 K_{RJ}. Since the baffle is fixed with respect to the detectors, its thermal emission is not expected to significantly affect the differential measurements. The attenuation of the ground pickup by the forebaffle was measured on site to be > 10–20 dB below the already low sidelobes of the primary beams, limiting the far-sidelobe response to < −30 dBi beyond 30° off-axis.

The 2-m tall outer screen reflects any stray sidelobes to the relatively homogenous cold sky. The 8-m top diameter is sized so that the diffracted ground radiation will never directly hit the window even at the low end of our observing elevation at 55°. As with the forebaffle, the edge of the outer screen is rounded with a 10-cm radius to reduce diffraction.

CHAPTER 3

Instrument Characterization

3.1 Introduction

To understand the behavior of the instrument, institute a meaningful program of its characterization, and properly analyze the data, we must first construct a reasonable model of the signal of the PSB. Detailed exposition and treatment of the polarized signal response of a PSB is available from Jones[16]; here we lay out a simplified treatment that seeks to motivate the discussions of instrument characterizations that follow.

Because of the low intrinsic cross-polar power response of the corrugated feedhorns ($\sim 10^{-4}$) and the typically high copolar leakage of the PSBs ($\sim$ few $\times 10^{-2}$), we have

$$\epsilon P_\parallel(\Omega) \gg P_\perp(\Omega) \tag{3.1}$$

where $P_{\parallel,\perp}(\Omega)$ are the normalized copolar and crosspolar power response functions, respectively, of a given beam, and ϵ is the polarization leakage. That is, typically, the copolar pattern dominates the response of a PSB to an orthogonally polarized source, and without much loss to the usefulness of the following discussions, we can safely ignore $P_\perp(\Omega)$ and let $P(\Omega) = P_\perp(\Omega)$. (Because in general the response functions are not symmetric *w.r.t.* the centroid of the beams, there is also an orientation dependence of the $P(\Omega)$ that is left implicit.)

The signal model of a Bicep PSB (ignoring the noise term) is as follows:

$$d(t) = H_t \otimes \frac{s'}{2} \int d\nu \, A_e F_\nu^\star \int d\Omega \, P(\nu, \Omega) \left[(1 + \epsilon) I + (1 - \epsilon) (Q \cos 2\psi + U \sin 2\psi) \right] \qquad (3.2)$$

where

- ψ is the orientation angle of the copolar direction *w.r.t.* the coordinates used to measure the Stokes parameters $\{I, Q, U\}$; the bearing angle from the pixel P to the instrument boresight relates ψ to the copolar instrument orientation angle χ: $\psi_P = \chi_P + \alpha_{P \to B}$ (See Appendix B)

- $\{I, Q, U\}$ are in units of spectral radiance (W sr^{-1} m^{-2} Hz^{-1}) and the dependence on (ν, Ω) is implicit

- $F_\nu^\star = \eta F_\nu$ is the absolute spectral response (normalization of F_ν and hence the definition of effective optical efficiency η to be given later)

- $A_e = (\lambda^2 / \Omega_b)$ by the antenna theorem[25], where $\Omega_b = \int d\Omega \, P(\nu, \Omega)$

- s' is the DC power responsivity of the PSB coupled to a single, pure polarization mode

- $H_t \otimes \ldots$ signifies the convolution of the time-domain kernel of the frequency transfer function.

This can be simplified by assuming $\epsilon(\nu) = \text{const.}$:

$$d(t) = H_t \otimes \frac{s}{2} \int d\nu \, \frac{\lambda^2}{\Omega_b} F_\nu^\star \int d\Omega \, P(\nu, \Omega) \left[I + \gamma (Q \cos 2\psi + U \sin 2\psi) \right] \qquad (3.3)$$

where $s = s' (1 + \epsilon)$ and $\gamma = \frac{(1-\epsilon)}{(1+\epsilon)}$. Further, if $\{I, Q, U\}$ vary slowly over the scale of the beam:

$$d(t) = H_t \otimes \frac{s}{2} \int d\nu \, \lambda^2 F_\nu^\star \left[I + \gamma (Q \cos 2\psi + U \sin 2\psi) \right] \qquad (3.4)$$

as may be the case for beam-filling test loads.

Complete knowledge of $\{\epsilon, \chi, P(\nu, \Omega), F_\nu^\star, s, H_t\}$ allows for the reconstruction of the input $\{I, Q, U\}$ on the sky given sufficient sampling (again, ignoring noise issues). But errors in the characterizations

of these instrument properties will in turn lead to errors in the reconstruction of the polarization map, some of which can be quite dangerous (as is the case when the large I leaks into Q/U).

A rigorous exploration of these systematic errors stemming from miscalibrations of the instrument can be carried out numerically, given an input scan strategy and a reasonable range of parameter space to be explored. An input map free of B modes is "observed" with a parameterized model of the instrument response, and the false B modes in the reconstructed output map quantify the level of systematic contamination in direct comparison with the experimental B-mode target. In conjunction with such numerical efforts, however, we can develop some intuitive and qualitative understanding of the systematic effects with the simplified signal model as applied to direct differencing of an orthogonal pair of PSBs.

3.1.1 Polarization orientation & leakage systematics

Let's ignore everything except ψ/χ. Given two nearly orthogonal PSBs A and B with *relative* orientation angle uncertainty $\delta\psi$:

$$
\begin{aligned}
d_{\text{A,B}} &= \frac{1}{2}\Big[I \pm \big(Q\cos(2\psi \pm \delta\psi) + U\sin(2\psi \pm \delta\psi)\big)\Big] \\
&= \frac{1}{2}\Big[I \pm \big(Q(\cos 2\psi \cos \delta\psi \mp \sin 2\psi \sin \delta\psi) \\
&\quad + U(\sin 2\psi \cos \delta\psi \pm \cos 2\psi \sin \delta\psi)\big)\Big]
\end{aligned}
\tag{3.5}
$$

Pair differencing gives

$$
\Delta d = d_{\text{A}} - d_{\text{B}} = \cos \delta\psi \, (Q\cos 2\psi + U\sin 2\psi)
\tag{3.6}
$$

that is, an error in the relative angle between the two arms simply results in a scaling of the measured Q/U — a comparatively benign effect. What about a *common mode* error (*i.e.,* co-rotation of ψ's)?

$$
d_{\text{A,B}} = \frac{1}{2}\Big[I \pm \big(Q\cos(2\psi + \delta\psi) + U\sin(2\psi + \delta\psi)\big)\Big]
\tag{3.7}
$$

$$
\begin{aligned}
\Delta d &= (Q\cos \delta\psi + U\sin \delta\psi)\cos 2\psi + (U\cos \delta\psi - Q\sin \delta\psi)\sin 2\psi \\
&= Q'\cos 2\psi + U'\sin 2\psi
\end{aligned}
\tag{3.8}
$$

As could be readily expected without the derivation, this gives a mixing between Q/U — potentially troublesome as this can result in $E \to B$ leakage.

Similarly with ϵ:

$$d_{\mathrm{A,B}} = \frac{1}{2} \left[I \pm \gamma_{\mathrm{A,B}} \left(Q \cos 2\psi + U \sin 2\psi \right) \right] \tag{3.9}$$

$$\Delta d = \frac{\gamma_{\mathrm{A}} + \gamma_{\mathrm{B}}}{2} \left(Q \cos 2\psi + U \sin 2\psi \right) \tag{3.10}$$

a simple scaling of Q/U as is the case for the error in the relative orientation angle.

3.1.2 Beam systematics

Again, ignoring all but the beam response functions, we have:

$$d_{\mathrm{A,B}} = \frac{1}{2} \int \mathrm{d}\Omega \, P_{\mathrm{A,B}}(\Omega) \left[I \pm \left(Q \cos 2\psi + U \sin 2\psi \right) \right] \tag{3.11}$$

$$\begin{aligned} \Delta d &= \int \mathrm{d}\Omega \left[P_{\delta} I + P_{\sigma} \left(Q \cos 2\psi + U \sin 2\psi \right) \right] \\ &= \int \mathrm{d}\Omega \, P_{\sigma}(\Omega) \left(\mathcal{P} I + Q \cos 2\psi + U \sin 2\psi \right) \end{aligned} \tag{3.12}$$

where $P_{\sigma,\delta} = \left(P_{\mathrm{A}} \pm P_{\mathrm{B}} \right)/2$ and $\mathcal{P} = P_{\delta}/P_{\sigma}$. Now there is direct leakage of I into Q/U for non-zero $\mathcal{P}$. Assuming elliptical gaussian beams, multipole expansion of $\mathcal{P}$ is convenient. Monopole, dipole and quadrupole then correspond to differential beam size, pointing and ellipticity, respectively, which are directly measured quantities.

Detailed study of these beam effects and the resulting distortions of E/B-modes is quite involved. We can make note of a few important observations without calculations, however. The monopole leakage of I into Q/U is invariant under rotation, and given sufficient coverage of ψ it can be accounted for. The dipole leakage is antisymmetric under $\psi \to \psi + \pi$, and, again, with sufficient cross-linking of the scan strategy, can be separated from the 2ψ sinuoidals in principle. (The ψ-dependence of $\mathcal{P}$ in sky coordinates is implicit.) However, this immunity to the dipole leakage is highly dependent on the scan-strategy, and anything less than an idealy cross-linked observation will result in significant systematic leakage of $\Delta T \to Q/U$.

Note that the quadrupole leakage is particularly dangerous, as it is symmetric under $\psi \to \psi + \pi$

(as are Q/U), and no amount of ψ coverage is sufficient to separate the temperature leakage into polarization without direct knowledge of $\mathcal{P}$. Although ground-based instruments with highly circular beams such as BICEP may contend with other, more immediate systematic hazards, for idealized experiments with less severe constraints in scanning (such as a satellite mission) the differential ellipticity may be the limiting effect among beam systematics.

There have been a number of efforts made to understand these beam systematics as pertains to CMB polarimetry, most recently by Shimon *et al.*[39] complementing a series of earlier works by Hu *et al.*[15] and others.

3.1.3 Spectral mismatch systematics

Let's look at a simplified form of Equation 3.4 assuming $\delta v \ll v_0$ such that $\lambda^2 \sim$ const., and ignoring all but the spectral response,

$$d_{\text{A,B}} = \frac{1}{2} \int \mathrm{d}v \, F_{\text{A,B}}^{\star} \left[I + (Q \cos 2\psi + U \sin 2\psi) \right] \tag{3.13}$$

$$\Delta d = \int \mathrm{d}v \, F_{\sigma}^{\star}(v) \left(\mathcal{F}(v) \, I + Q \cos 2\psi + U \sin 2\psi \right) \tag{3.14}$$

using analogous notation as in the discussion of beam systematics. Again there is direct $I \rightarrow Q/U$ leakage, but since $\mathcal{F}$ is independent of orientation and otherwise static, a well cross-linked scan strategy can in principle deal with this, and is unlikely to be harmful given the well-matched spectral response of PSB pairs co-located behind common feed structures and band-defining filters.

3.1.4 Relative gain and transfer function systematics

Similarly, given two PSBs with responsivities $s_{\text{A,B}}$,

$$d_{\text{A,B}} = \frac{s_{\text{A,B}}}{2} \left[I \pm (Q \cos 2\psi + U \sin 2\psi) \right] \tag{3.15}$$

$$\Delta d = \left[s_\delta I + s_\sigma \left(Q \cos 2\psi + U \sin 2\psi \right) \right] \tag{3.16}$$

where $s_{\sigma,\delta} = (s_{\text{A}} \pm s_{\text{B}})/2$, as before. The transfer function in this case can be simply seen as frequency-dependent responsivity, and absorbed into $s_{\text{A,B}}$. As with the beam effects, errors in correcting for the

relative gains/transfer functions can leak temperature into polarization. This may also be a dynamic problem, since both the responsivity and the complex transfer function are subject to variations as the optical loading on the PSB changes.

Whereas the relative gain errors result in a constant leakage of I into Q/U, errors in the transfer functions give a scan-speed dependent leakage that manifests as an ℓ-dependent contamination in the fourier domain. Both must be measured to similar accuracies given the specifications derived numerically. Because the transfer functions are not measured on a regular basis during scanning as is the case for relative gains, the characterization tests must further demonstrate that the loading-dependence is limited or known across the expected range encountered during observations.

3.1.5 Numerical specifications on systematic errors

A meaningful instrument characterization regime must be informed by the knowledge of how systematic errors affect the ultimate science goals. In the case of BICEP, we are guided by the desire to measure the B-modes down to an unprecedented limit of $r \sim 0.1$, and must verify that the accuracies with which we measure the parameters of Equation 3.3 are adequate to limit the contaminations of B below that level.

Numerical simulations were carried out taking into account the details of actual scanning strategy to derive such limits, using B-free input maps to quantify the contaminations for various levels of systematic effects. Table 3.1 lists the results of the simulations with a summary of actual achieved accuracies in calibrations. The characterization of BICEP meets the specifications for all major areas of systematic errors. The following sections of this chapter discuss the measurement processes and their results in more detail.

	Definition	Specification	Measurement
Relative gain mismatch	$(s_A - s_B)/\bar{s}$	$< 1.5 \times 10^{-2}$	$< 0.5 \times 10^{-2}$
Polarization orientation	$\Delta\psi$	$< 8.0°$	$\sim 0.3°$
Differential beam width	$(\sigma_A - \sigma_B)/\bar{\sigma}$	$< 4.0 \times 10^{-2}$	0.2×10^{-2}
Differential pointing	$\Delta\theta/2\bar{\sigma}$	$< 1.5 \times 10^{-2}$	1.0×10^{-2}
Differential ellipticity	$(e_A - e_B)/2$	$< 9.0 \times 10^{-2}$	0.1×10^{-2}

Table 3.1: Specified and measured systematic errors derived from numerical simulations of the scan strategy. The specifications correspond to a contamination magnitude of 0.1 μK at $\ell = 100$. The measured differential beam parameters correspond to the 75% quantile.

3.2 Spectral response & optical efficiency

Although the measured spectral response and optical efficiencies do not directly factor into the final data analysis in an appreciable manner, they are still crucial in the development and testing of the instrument, and it is important to verify them in some detail.

The spectral response and the end-to-end optical efficiency are not independent quantities, so it makes little sense to talk of one without defining the other unambiguously. The absolute transmission can be seen as a product of a normalized transmission and an effective efficiency: $F^\star(v) = \eta F(v)$. The separation is natural in the case of a simple top-hat transmission:

$$F^\star(v) = \eta_0 \qquad v_0 - \frac{\Delta v}{2} < v < v_0 + \frac{\Delta v}{2} \tag{3.17}$$

where $F(v)$ is just the normalized top-hat function. Given an arbitrary absolute transmission, it is convenient to define the normalization such that it is analogous to the above trivial case. We can impose the following condition:

$$\frac{\int dv\, F^2(v)}{\int dv\, F(v)} = 1 \tag{3.18}$$

which is to say, the self-weighted average of a normalized transmission function should be unity. We can then define the following for convenience:

$$v_0 = \frac{\int dv\, vF(v)}{\int dv\, F(v)} \qquad \text{and} \qquad \Delta v = \int dv\, F(v) \tag{3.19}$$

The optical efficiency η is then simply the direct ratio of the absolute and relative transmissions, as before:

$$\eta = \frac{\int dv\, F^{\star 2}(v)}{\int dv\, F^\star(v)} = \frac{F^\star(v)}{F(v)} \qquad \text{and} \qquad \int dv\, F^\star(v) = \eta \Delta v \tag{3.20}$$

which agrees with intuitive definitions of these quantities. The advantage of such a normalization scheme for spectra in general is that the expressions are fully analytical, simple to calculate, and do not make use of ad-hoc conventions that are ambiguous in their resulting definition of quantities such as Δv and η.
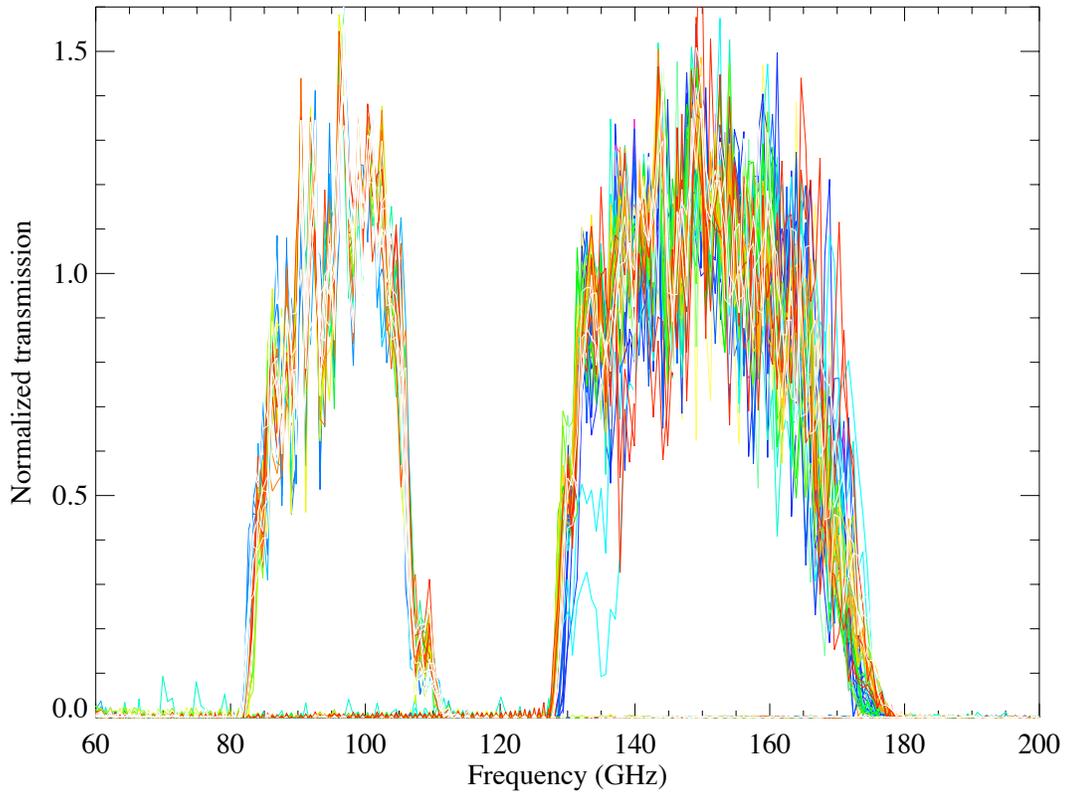
Figure 3.1: Normalized spectral response measured with Martin-Puplett FTS. The normalization convention is given in Equation 3.18.

The normalized transmission was measured using a Martin-Puplett type fourier transform spectrometer, coupled to individual beams one at a time. Multiple interferograms were measured for each channel, and averaged to achieve adequate S/N. Figure 3.1 shows the measured spectra for both frequency bands. With the exception of two 150 GHz channels that show degraded transmissions above the waveguide cut-on (possibly due to contaminations within the corrugations in the throat sections of the feedhorns), the spectra are largely repeatable across the focal plane with consistent edge definitions.

Figure 3.2 shows the bandwidth vs. bandcenter scatter diagrams. In a fractional sense, the 100 GHz channels have more consistency in both ν_o and $\Delta\nu$. The distributions are not only wider in the 150 GHz channels, but there is also a slight positive correlation between ν_o and $\Delta\nu$. This is suggestive of variations in the transmission performance of the low-pass filters across individual filter stacks. Such variations are tolerable since within PSBs pairs the spectra are still well-matched in general.
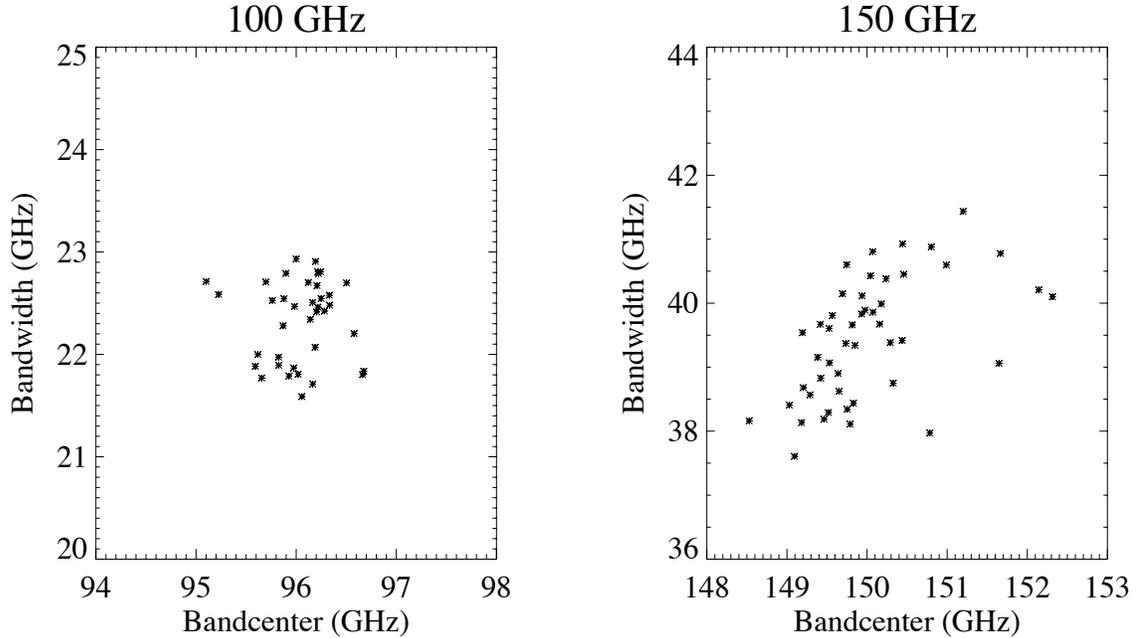
100 GHz

150 GHz

Figure 3.2: Distribution of band widths and band centers.

Small spectral leaks above the band-defining edges are difficult to measure accurately in the presence of relatively overwhelming optical power from the main transmission bands. Typically metal mesh filters exhibit leaks at multiples of the cut-off frequency. Even when employing multiple filters stacks with staggered edge designs that limit such problems, it is important to ascertain the level of high frequency leaks or set reasonable upper limits on them.

This is accomplished by using thick-grille filters, placed between a chopped thermal source and the instrument aperture stopped down to ~ 1 in. Two different TGFs were used in testing, with approximate cut-on edges at 5.5 cm^{-1} and 8.5 cm^{-1} — designed to be ideally placed halfway between the main transmission bands and expected locations of the leaks.

Figure 3.3 shows the resulting fourier transforms of the chopped signal for two pairs of PSBs at each frequency band as representative examples, normalized to the peak response. The thermal source was chopped at 3 Hz and baseline data were acquired without the TGFs in place (top-most traces in black). Data for 5.5 cm^{-1} and 8.5 cm^{-1} are shown in red and blue, respectively, accounting for the reduction factors due to the sub-unity geometric filling factors of the TGFs. The 5.5 cm^{-1} TGF cuts across the 150 GHz band, and as we expect we see a big response that we can otherwise disregard.
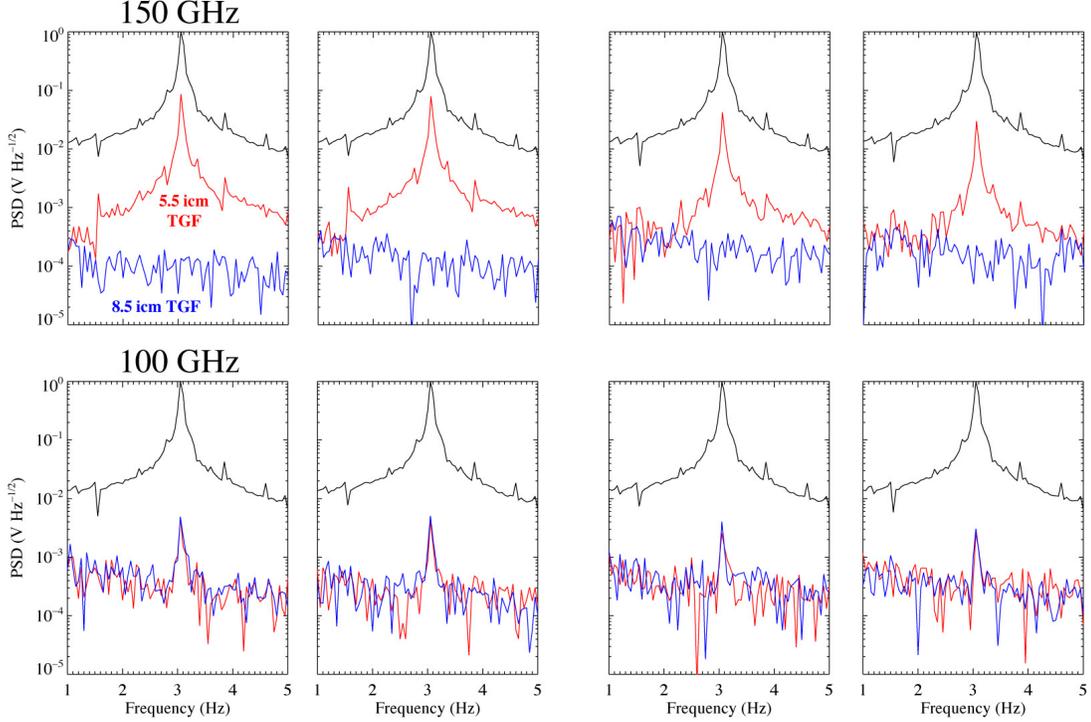
Figure 3.3: Thick-grille filter measurements of out-of-band leaks. Two TGFs at 5.5 cm^{-1} and 8.5 cm^{-1} were used (with the former cut-on well within the 150 GHz band as can be seen. Noise-limited upper limit on out-of-band leaks for 150 GHz is at < -30–40 dB; a small leak is measured at ~ -25 dB for 100 GHz channels.

8.5 cm^{-1} TGF results for that band show no evidence of leaks, noise-limited down to < -30–40 dB. A small positive detection in the 100 GHz channels are evident, however, at ~ -25 dB. The agreement of the leak magnitude between the two TGFs suggest that this small leak is above ~ 255 GHz. The magnitude of the leak is low enough that no adverse effects are expected from simply ignoring it.

Given measurements of the relative spectral transmissions we can then quantify the end-to-end optical efficiencies in a sensible manner. According to Equation 3.4, for a given beam-filling source with spectral radiance $B(v, T)$, the total optical power absorbed by a PSB is given by

$$Q_{\text{OPT}} = \frac{\eta}{2} \int dv\, \lambda^2 F(v) B(v, T) \tag{3.21}$$

The total power on the detector is $P_{\text{TOT}} = P_{\text{ELEC}} + Q_{\text{OPT}}$, where P_{ELEC} is the dissipated electric power from the detector current biasing. By varying the bolometer bias and measuring the resulting loadcurves for two different source temperatures, we can obtain the power difference ($-\Delta P_{\text{ELEC}} = \Delta Q_{\text{OPT}}$) across

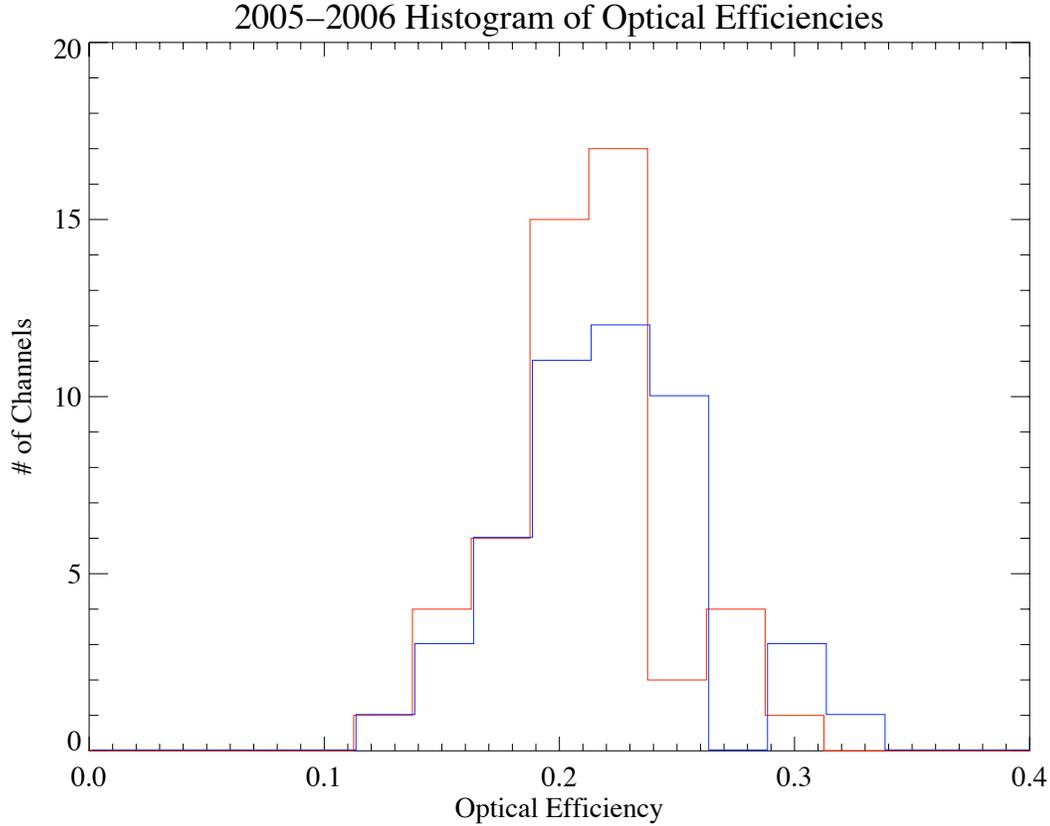## 2005–2006 Histogram of Optical Efficiencies

Figure 3.4: Measured optical efficiencies for 1st season. 100 GHz and 150 GHz are shown in red and blue, respectively.

equal bolometer temperatures (and hence equal P_{TOT}). The measured ΔQ_{OPT} allow us to solve for the optical efficiency η given $F(\nu)$.

After the integration of the instrument following the deployment for the first season, a series of loadcurves were measured with ambient and LN sources (~ 295 K and ~ 75 K, respectively). Figure 3.4 shows the histograms of measured optical efficiencies for both frequency bands, with typical percentage values in the low 20's. These are somewhat lower than what was expected at the beginning of the instrumental design process.

A number of channels show large differences in the measured efficiencies *within* PSB pairs, suggesting some of the spread in the measured values are due to inefficiencies in coupling of the incoming radiation to the metalized bolometer webs. Some of the degradation in efficiency is also to be attributed to the front-to-front coupling of the back-facing and PSB feedhorns where the band-

defining filters are situated. The coupling relies entirely on incidental overlap of the equivalent gaussian modes of the apertures of the facing feedhorns; no lenses are used to optimize the coupling of the beams that are axially separated by large multiples of the wavelengths.

3.3 Beam-mapping

To co-add maps appropriately and ascertain the level of systematic contaminations, we must understand the characteristics of each beam on the sky with sufficient accuracy. Beam measurements comprise two related, but distinct, general goals which are 'global' or 'local' in scope: (1) the construction of a radio pointing model which describes the locations of beams on the sphere in relation to each other and to the telescope attitude, and (2) the characterization of each beam as an elliptical gaussian, and the resulting measurements of differential beam width, pointing and ellipticity for each polarization pair of beams.

Ideally, a single set of measurements would provide both the global properties of beam positions and the local properties of the beam shape and differential parameters. In reality this is made difficult for an instrument like Bicep. Large degree-scale beams rule out many otherwise bright point-like sources, as they are too dim; Jupiter and the Moon are viable sources that meet some of the needs of the characterizations, but are not readily accessible without additional external flat mirrors at the South Pole site due to their low elevations. (Efforts have been made to take data in this configuration, however, and full analyses are pending.)

We have thus far relied to two disparate methods: the 'local' quantities of each beam are measured using an unpolarized chopped thermal source in the quasi-far-field region, and the 'global' radio pointing model is provided by an iterative fitting of individual channel's centroid position that maximizes the correlation between the observed CMB map of that channel and the focal plane-wide average map, performed separately for the two frequency bands.

There have been three major campaigns to characterize the beams using an unpolarized chopped thermal source: indoor high-bay measurements at a distance of ~ 41 m prior to initial deployment, and two outdoor measurements made in the field using a collapsible mast at a distance of ~ 11 m. Neither configurations are truly in the far-field ($\sim 2d_{\mathrm{APER}}^2/\lambda$) at 150 GHz. However, the high-bay con-
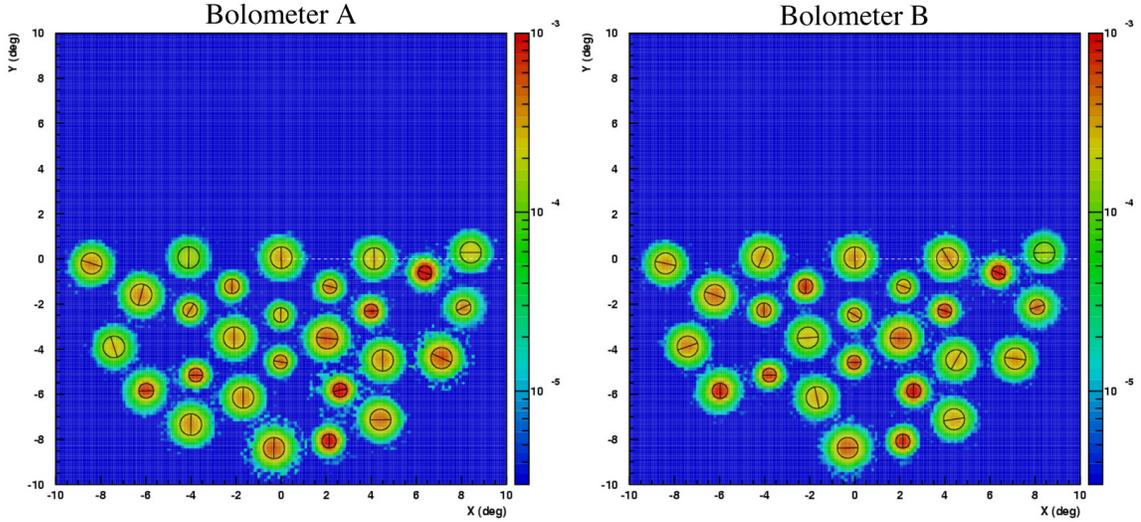
Figure 3.5: High-bay beam maps with an unpolarized chopped thermal source. The left/right panels show the measured beam profiles for polarization pairs. Multiple measurements were made at different boresight orientations to obtain complete coverage of the focal plane. The black circles represent the fitted ellipsoids with the orientation of the major axes shown by the lines.

figuration is at the transition region for 100 GHz, and the most trustworthy measurements to date have come from that data set — this despite a much higher optical loading due to the ambient background compared to the South Pole sky and the resulting loss of sensitivity. The beam profiles were measured with typical relative noise floor of -20 dB in the high-bay, and -30 dB with the outdoor mast at the South Pole.

Figure 3.5 shows beam maps made at a single boresight orientation in the high-bay (with the source at a very low elevation, multiple orientations were necessary to obtain complete coverage of all pixels). The beams are highly circular, with average ellipticity of 0.9×10^{-2}, and none exceeding 2.0×10^{-2}. Even under worst-case scenarios, the differential ellipticity would be well under the specified limit of 9.0×10^{-2}. The mean FWHM are $0.93°$ and $0.60°$, with no significant deviations.

The measured differential beam parameters from this data set are shown in Figure 3.6. Both the differential beam width and the differential ellipticity are well within the specified limits (see Table 3.1). The differential pointing is the most dominant measured beam systematics relative to specifications, with a number of channels near the allowed limit of 0.015. The bulk of the beams are still well within the allowed range.

Although more than adequate for BICEP's stated science goals, the achieved differential point-
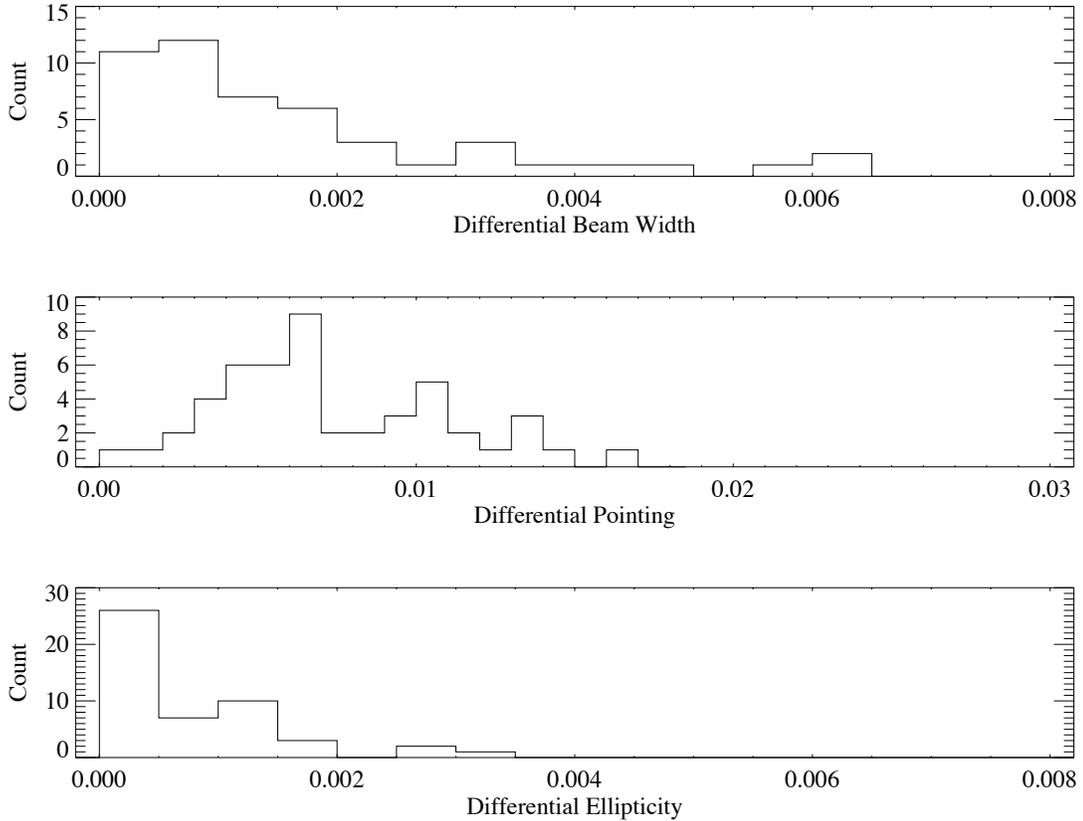
Figure 3.6: Histograms of measured differential beam width, pointing and ellipticity from the high-bay beam-mapping.

ing performance would be worrisome for the next-generation instruments with BICEP-like optics. The effect would have to be reduced with a more optimized optical design (provided the underlying mechanism for the beam separations are understood) or the quality of the beam characterization tests would have to be improved to achieve higher fidelity.

The high-bay data indicate that there is some correlation between the focal plane polarization orientation of a given PSB pair and the orientation of the beam separation vector. Instrument "Q" pixels tend to separate radially, and "U" pixels azimuthally, with the magnitude of the separation correlated with the distance of the pixel from the boresight, as would be expected from symmetry considerations. However, the near-field measurements at the South Pole are not completely consistent with this, and dominated by unknown systematics. Work is underway to both understand the underlying mechanism for the beam separation with lab testing and to construct a more robust beam measurement regime during the upcoming 2007-2008 season — such work would benefit and

inform the optical designs of the next-generation small aperture polarimeters.

3.4 Polarization response calibration

To characterize the polarization response of the PSBs, we use a dielectric sheet calibrator based on POLAR's design,[34] providing an absolute temperature calibration to ±10% and polarization orientation to within ±1°, on a monthly basis if needed.

A small partially polarized signal of known magnitude is created by using an 18-μm polypropylene film as a 45° beam splitter in front of the telescope aperture, reflecting a fraction of the beam onto an ambient load. The ambient load lining the inside surface of the cylindrical calibrator is exactly analogous to the Eccosorb HR/Volara layers used in the forebaffle, giving ~95% emissivity over the two bands and presenting a similar optical load as during normal observing. This particular setup produces a partial polarization of amplitude ~ 100 mK at 100 GHz and 250 mK at 150 GHz, which is small enough to ensure that the change in bolometer responsivity due to the calibration process itself is negligible (see Figure 3.8).

During calibration, the forebaffle is replaced with the dielectric sheet calibrator. Boresight rotation of the cryostat while pointed at zenith modulates the partially polarized signal induced by the dielectric sheet. Unlike POLAR's single on-axis beam, Bicep's off-axis beams see complicated but calculable deviations from the simple sinusoidal modulation.
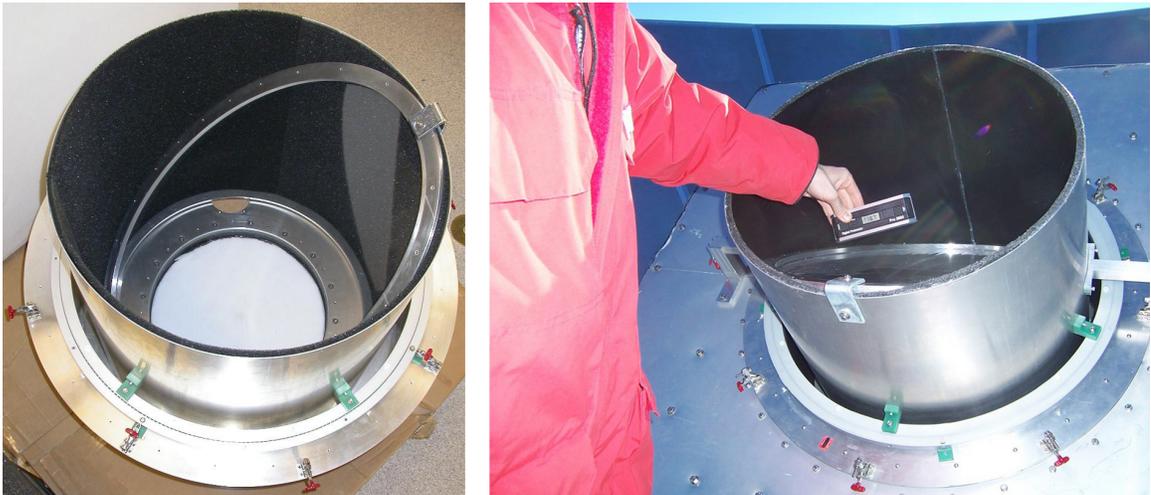

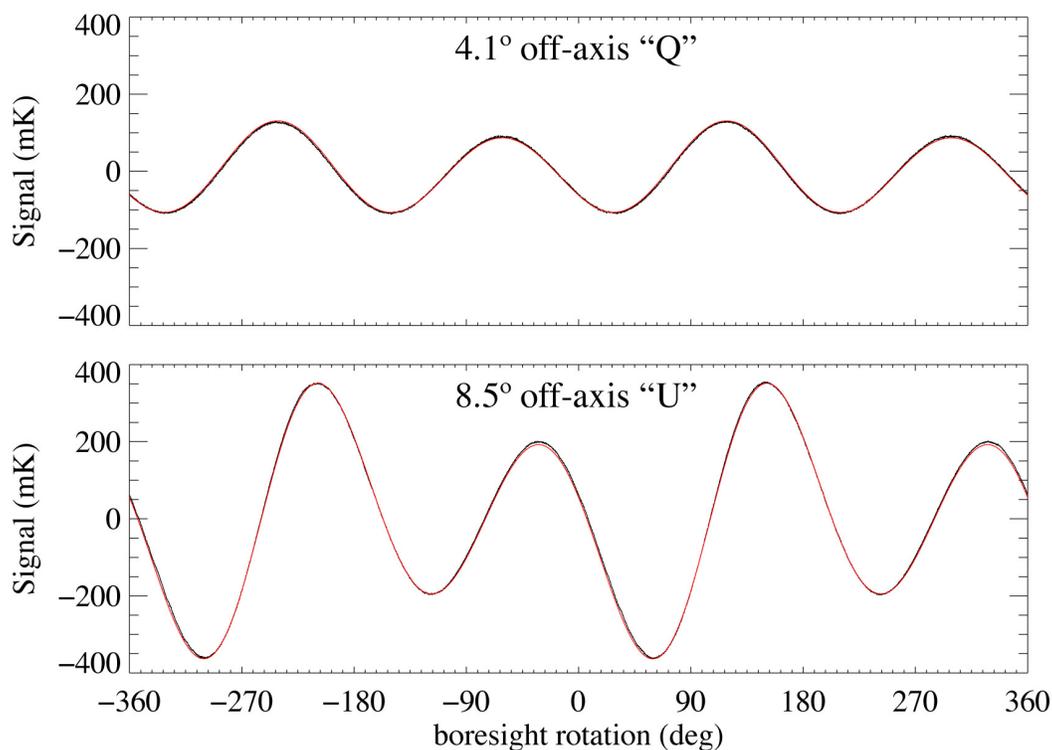Figure 3.7: The dielectric sheet calibrator.

Figure 3.8: Measured responses and model fits to the dielectric polarization calibrator.

The calibrator is used on a regular basis throughout the observing season. The measured signals are fitted to within a few percent of the theoretical model reliably, and the polarization orientations are determined to well within $1°$. Measurement-to-measurement stability is excellent, and there is no indication of any systematic drifts in the measured orientations. The dominant measurement systematics are associated with the repeatable referencing of the instrument orientation and the uncertainty with which that orientation is defined for each successive assembly of the cryostat with the mount. These are still at the sub-degree level, however, and do not pose a significant problem.

The uncertainty in the absolute gain is expected to be ~8%, mostly due to the ~3% uncertainty in the polypropylene film thickness. Although deriving the absolute gain with the dielectric calibrator is very useful, especially during early stages of the instrument characterization and testing, ultimately the definitive absolute gains of all pixels are derived with cross-calibration of observed CMB data with those of WMAP.

3.5 Bolometer transfer functions

BICEP depends entirely on pair-differencing the timestreams of orthogonally-polarized PSBs to measure polarization on the sky. Errors in the ratios of the measured transfer functions within a pair, therefore, directly result in ℓ-dependent $T \rightarrow Q/U$ leakages. Simulations of BICEP observations show that ~ 1% accuracy in transfer function measurements is necessary to limit the systematic B-mode contributions to below the $r = 0.1$ level.

Our measurements have largely relied on analyzing the step response to a fast-switching square-wave Gunn source operating at 10–100 mHz, while under optical loading conditions representative of CMB observations. Although the requirements derived from simulations apply strictly to the *relative* transfer functions within a pair (with far less stringent requirements on the individual absolute transfer functions, as is the case for the absolute DC calibrations), we have strived to achieve ~ 1% accuracy on single-ended measurements.
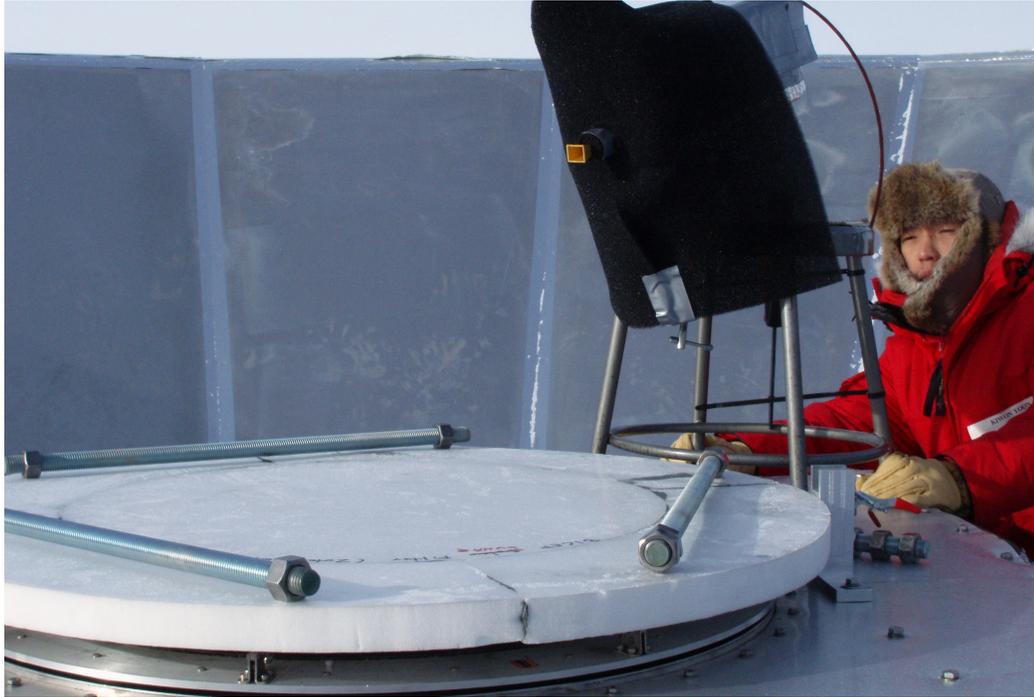

Figure 3.9: Gunn transfer function measurement set-up. The fore-baffle is removed and replaced with a Zotefoam sheet embedded with diffracting elements (*i.e.,* washers). The Gunn source is placed outside the field of view of the outer-most pixels for a small modulated signal against a low-background zenith sky.

During the measurements, the telescope is pointed at the zenith, with the aperture of the instrument covered by a sheet of Zotefoam. The Gunn source, either at 100 GHz or 150 GHz, is placed outside the field of view of the instrument, with the output pointed horizontally going across the aperture. This allows us to use small embedded washers on the Zotefoam sheet to diffract a controlled amount of the Gunn output into the beams across the entire focal plane while keeping the overall optical loading within the nominal ranges seen during CMB observing.

In addition to measuring the transfer functions, we explored the dependencies on modulated Gunn magnitude (to quantify non-linearity) and background loading. The amplitude of the Gunn source is directly controlled by an attenuator at the source. The optical loading was adjusted using weakly-emmissive foam pieces atop the Zotefoam sheet along with the diffracting washers.

Initial efforts to measure the transfer functions were made in 2006 February prior to the commencement of first-year observing, with an 100 GHz source only. Because the source had a spectral leak at a multiple of the base generator frequency, measurements for the majority of the 150 GHz channels were also possible at the same time. The transfer functions were measured down to 0.1 Hz with high S/N during this round of testing.

Evidence of significant transfer function roll-off from DC to ~ 0.1 Hz for a few of the channels — seen in the differenced PSB pair maps as a T-leakage, and hinted at by the above data-set — compelled follow-up measurements at the end of the first observing season, this time down to 0.01 Hz (below the lowest effective fourier mode of the elevation nods used to measure "DC" relative gains). Comprehensive measurements exploring the non-linearity/loading-dependence phase space were then made prior to the second season observing in 2007 February, this time with both 100 GHz and 150 GHz sources available.

It is important to note that the requirements on the frequency coverage of the transfer function measurements are directly tied to the strategy used to measure relative gains of PSB pairs during observing. In the case of BICEP, even though the spatial frequency range of interest ($30 < \ell < 300$) correspond roughly to the detection bandwidth of 0.1–1 Hz, because the process of relative gain measurement takes place over a minute timescale, the complex magnitude roll-off between the signal band and ~0.02 Hz must be known to within 1% accuracy. Otherwise any potentially unknown roll-

off between the signal band and the effective frequency at which the relative gains are "pegged" will result in a direct constant leakage of the temperature into polarization.

3.5.1 Analysis Technique

Ideally, the Gunn source presents a perfect square-wave optical signal, and analysis in this case is trivial: simply take the ratio of the fourier transforms of the response and the input square wave, keeping only the odd harmonics where power is present. In reality, the quality of the measurement is degraded by (1) background loading fluctuations during testing, and (2) additional Gunn source instabilities during the "on"-state. Both are well-described by $1/f$ spectra, but in otherwise good measurement conditions it is the latter that has dominated, preventing straightforward analysis of the test data.

Exploration of this problem has indicated that the instability may be due to sensitive geometric dependences of the scattered light paths and interferences thereof, which results from the monochromaticity and coherence of the source.

The method we employ in analyzing such data is to artificially reconstitute a clean, whole-period square-wave response using only the Gunn "off"-state portion of the data. Figure 3.10 shows simulated responses of a pair of bolometers with an unstable Gunn source as the input signal, with the two transfer functions given by the following toy model, as an example:

$$A(\omega) = A_0 \left[\frac{1 - \alpha}{(1 - i\omega\tau_1)(1 - i\omega\tau_2)} + \frac{\alpha}{(1 - i\omega\tau_c)} \right] \tag{3.22}$$

Bolometer A (green) has a simple single-pole RC profile, with $\tau_1 = 30$ ms and $\{\tau_2, \alpha, \tau_c\}$ set to zero. Bolometer B (blue) represents a more complex, pathological behavior, with two RC filters in series along with a significant slow additive component: $\tau_1 = 30$ ms, $\tau_2 = 5$ ms, $\alpha = 0.2$, $\tau_c = 3$ s. (The signals shown correspond to NTD bolometer outputs, with decreasing voltage corresponding to increasing optical input.)

The straightforward analysis is to simply take the ratio of the Fourier transforms of the bolometer timestream and the source input (assumed to be a perfect square-wave), keeping only those modes with non-zero power, i.e., odd harmonics of the fundamental frequency. But in the presence of excess
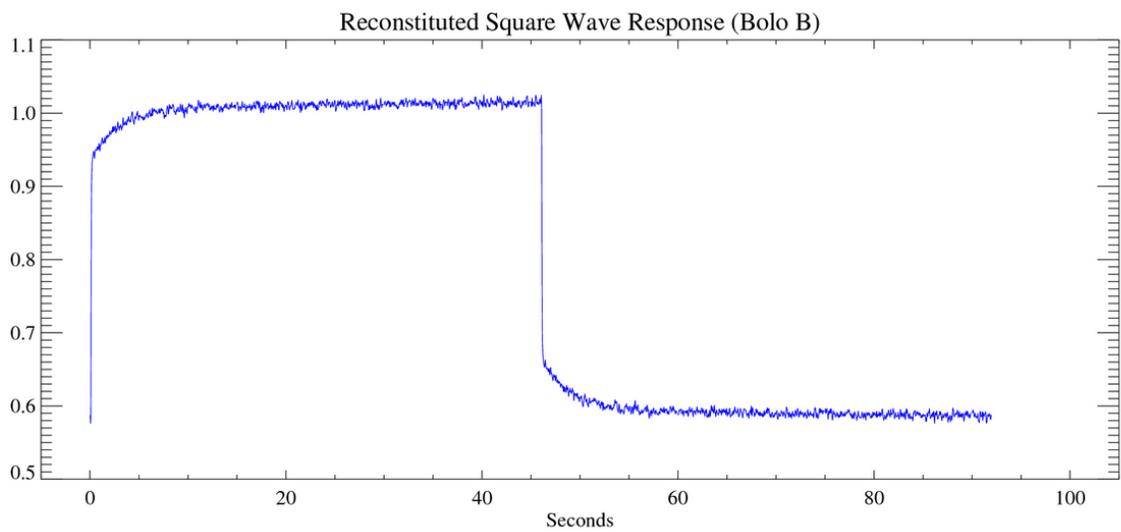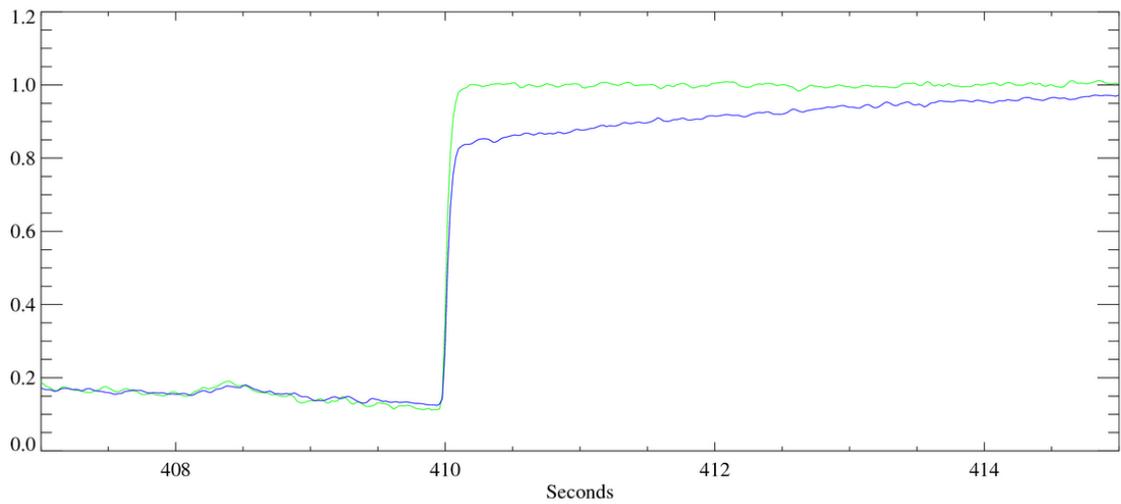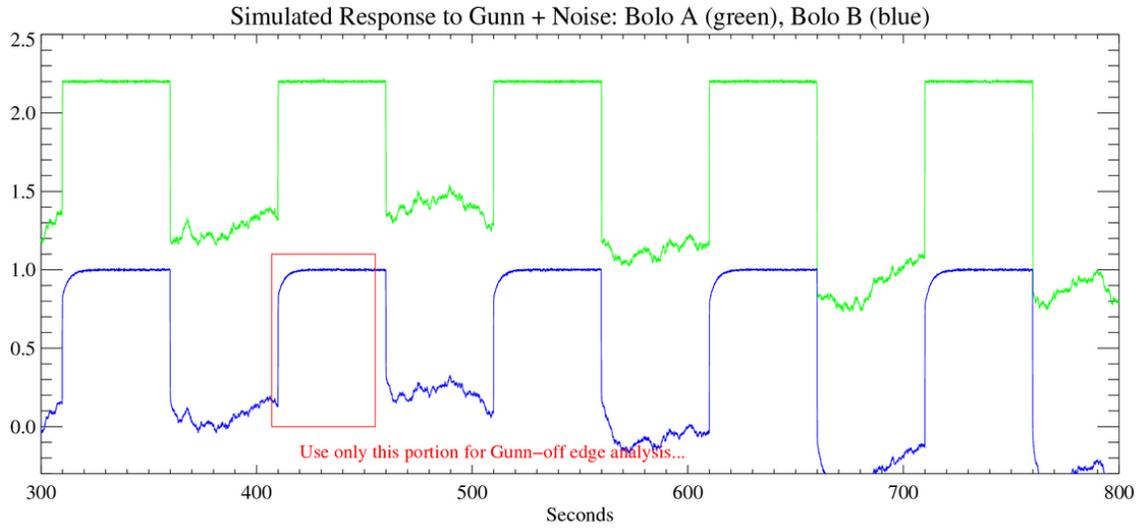
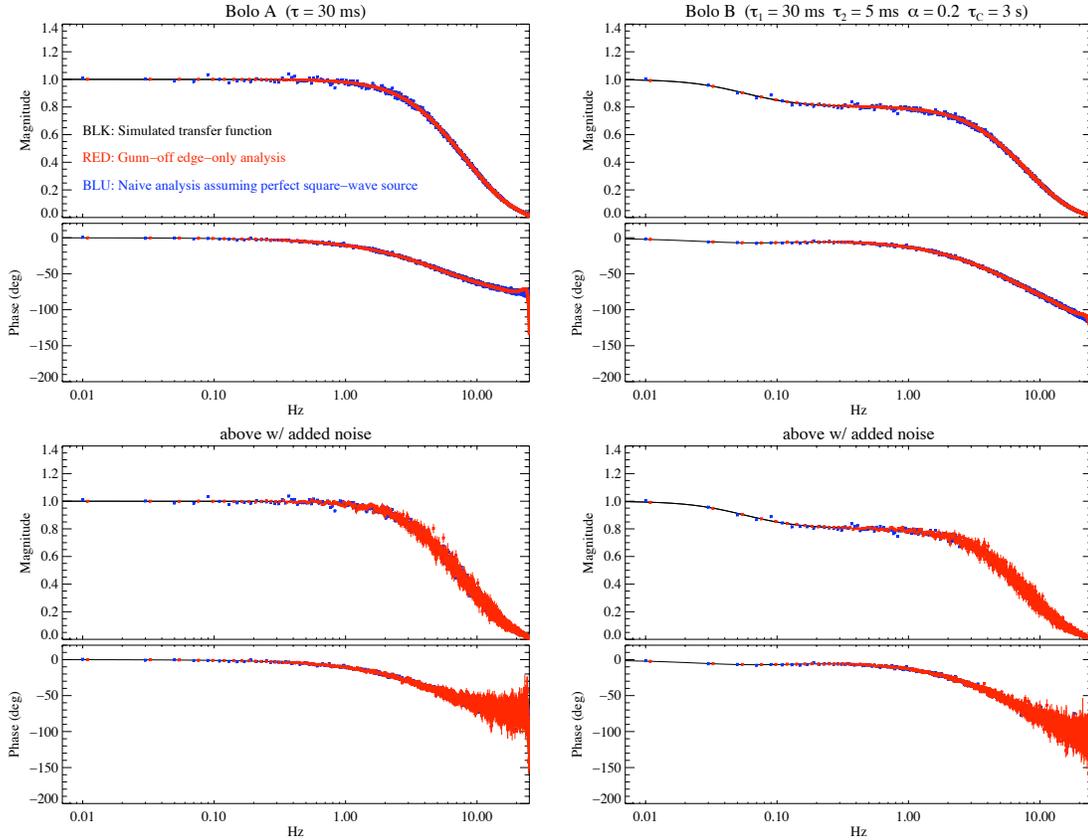Figure 3.10: Simulated responses to the Gunn source with on-state instability.

Figure 3.11: Comparison of simulated transfer function recovery between straightforward analysis and "off"-state-only analysis. The "off"-state-only analysis avoids contamination from "on"-state noise without any measurement bias. The second row shows the analysis results where an additional uniform white noise component has been introduced to the simulated source.

source instability, this method leaves the results of the analysis vulnerable to noise contamination.

The "off"-state-only analysis examines each Gunn-"off" step response separately (shown in red outline in the first panel of Figure 3.10), inverting and concatenating with the original to reconstruct a single square-wave period. The third panel of the same figure shows the resulting reconstructed response of bolometer B. The ratio of the FFTs for this given period then constitutes a single measurement of the transfer function, and the errors in the measurement can be derived from an ensemble of many such edge responses.

This aggressive windowing of the data to avoid contamination from "on"-state instabilities does not bias the measurement, however. Figure 3.11 compares the ability to recover the underlying simulated transfer functions between the straightforward analysis and the "off"-state-only analysis. Both A and B transfer functions are recovered accurately and without noise penalty by the latter method,
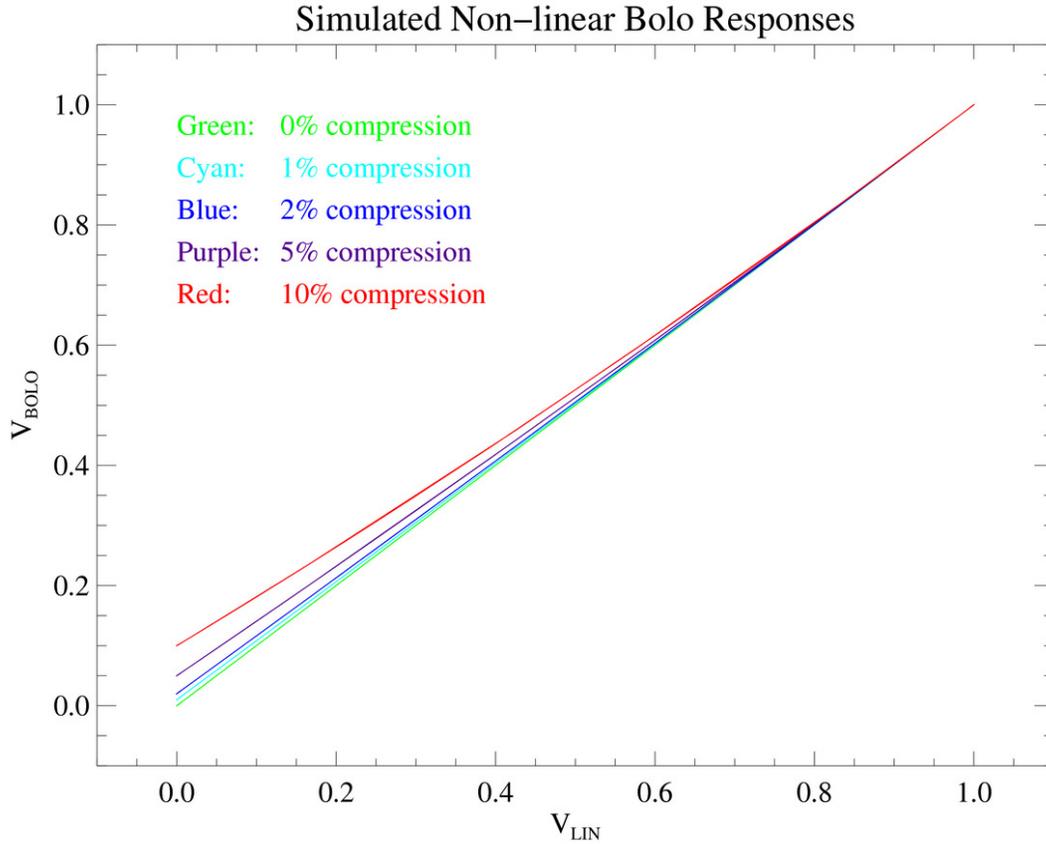
Figure 3.12: Simulated non-linear bolometer responses, for varying levels of peak response compression.

whereas the straightforward technique suffers from noise penalty due to the "on"-state fluctuations.

This will not be the case in general, since an arbitrarily complex thermal network will have an arbitrarily large "memory" (or, equivalently, higher dimensionality of initial conditions). Such windowing of the data as we have employed here — keeping only the "off"-state response and treating it as the response of a pure step function — will inevitably lead to a biased extrapolation of the underlying transfer function given sufficient levels of "on"-state fluctuations. To justify the usage of this analysis technique, it must be demonstrated that the bolometers are sufficiently described by a relatively simple model such as Equation 3.22 with a limited number of parameters.

3.5.2   Effects of Non-Linear Response

The dynamic distortion of the bolometer response as a result of the inherent non-linearity of the detectors is worth investigating, given the stringent requirements on the accuracy of the transfer

Figure 3.13: Contribution of a quadratic non-linear distortion *w.r.t.* the linear response to an input Gunn signal. Non-linear components expressible in even powers of the input (v^2, v^4, *etc.*) will always result in residuals at twice the input signal frequency.
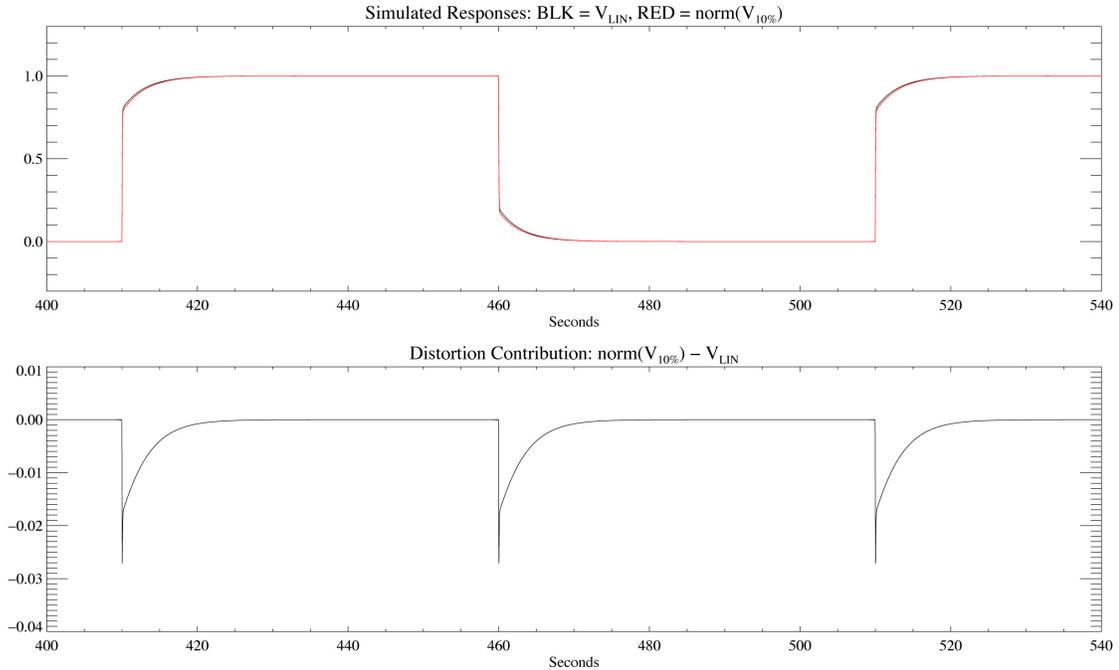
function measurements. Figure 3.12 shows the range of quadratic non-linearity, parametrized by the compression of peak response *w.r.t.* the linear response (in green), for which simulated analyses were carried out analogous to the results shown in Figure 3.11.

Figure 3.13 compares the square wave response of a linear detector (in black) with that of one with 10% peak compression resulting from a quadratic non-linear term. Once normalized, it can be seen that the residual between the two is strictly at twice the input frequency: the distortion contribution is exactly the same for the "on" and "off" halves of the square wave period. This means that the straightforward analysis of such waveforms to measure transfer functions will be immune to any biasing effects of non-linear response, as there is a clean separation in the fourier domain between the measured signal (in the odd harmonics) and the non-linear distortion component (in the even harmonics).

The same cannot be said for the otherwise advantageous "off"-state-only analysis technique, as the process of inverting and concatenating a half-period response to reconstruct a whole period renders the non-linearity residual to be at the same fundamental frequency as the signal source, and we

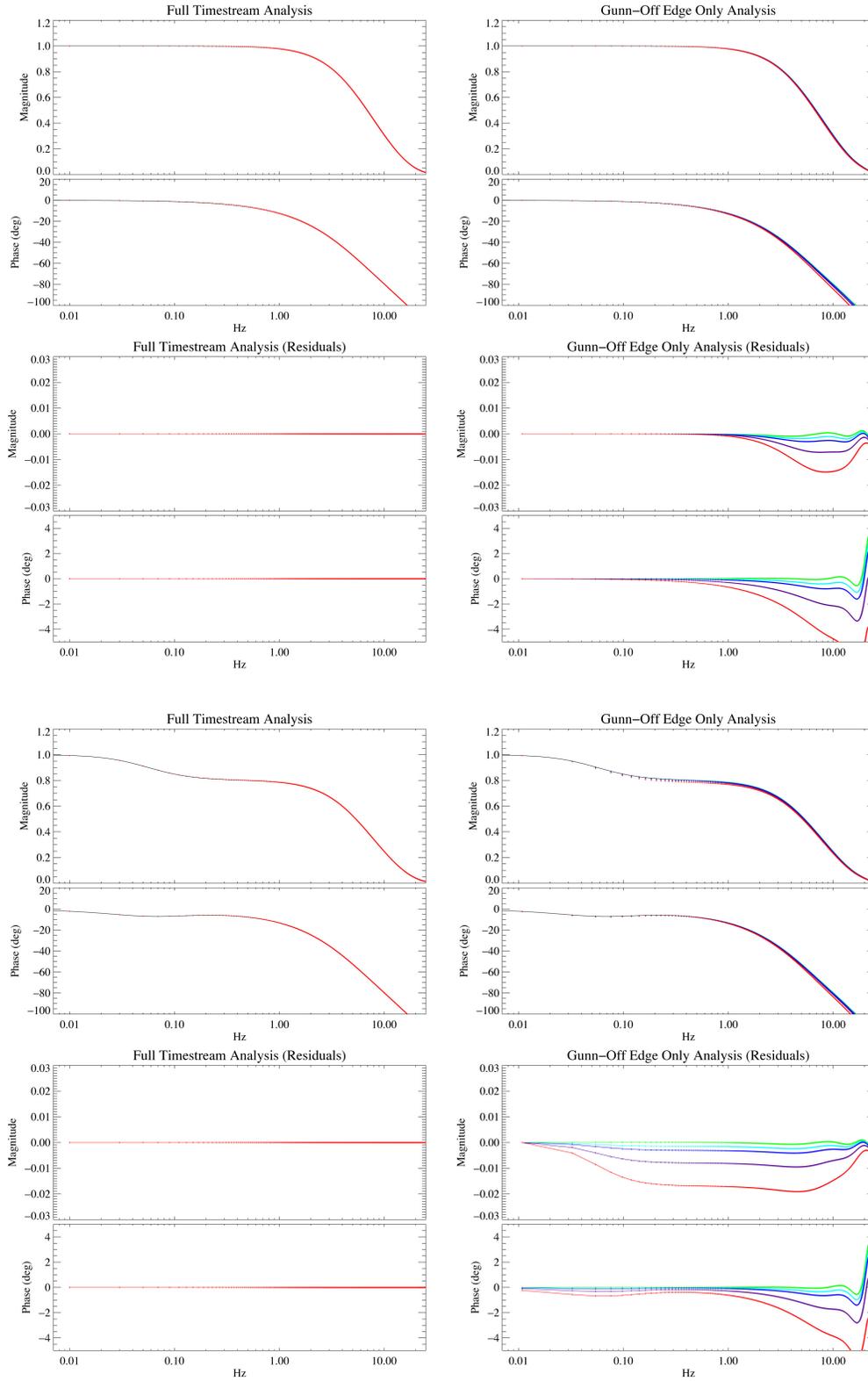Figure 3.14: The effect of non-linear bolometer response on the analysis of transfer function measurements, for the range of dynamic compression shown in Figure 3.12. The top two rows correspond to model bolometer A; the bottom two to model bolometer B. To achieve the specified accuracy of 1% on the transfer functions, the dynamic compression encountered during the measurements must be kept below ∼ 5%.

can expect the analysis results to be biased by the non-linear response.

Figure 3.14 shows the results of the simulated analyses using both methods, for the range of dynamic compression shown previously. As expected from the preceding argument, the straightforward analysis is totally immune to quadratic non-linearity. In reality, odd-power non-linear components of a bolometer response will result in biased measurements, but since this is at worst a third-order effect, we can expect this to be negligible.

The "off"-state-only analysis technique is vulnerable to being biased, also as expected, and 10% dynamic compression can lead to significant biases in the measured transfer functions above the allowed threshold of 1% accuracy. But the degree of this bias is also mediated by the actual magnitude of the underlying transfer function, such that for the model bolometer A which has near-unity transfer function up to ~ 1 Hz, the effect of non-linearity is minimal (top two rows in Figure 3.14).

The particular danger of non-linearity lies with those channels that have pathological behavior similar to model bolometer B (bottom two rows in Figure 3.14), with large roll-off between DC and the signal bandwidth of interest, and correspondingly large measurement/analysis bias over the same frequency range.

In all subsequent discussions of analysis of real measurement data, we have applied the above "off"-state-only analysis technique and have verified that the biases induced by the non-linearity, if any, are below the threshold of the requirement.

3.5.3   Initial Results from 2006 February

Figure 3.15 shows a representative selection of results from data taken in Feb 2006 with the 100 GHz Gunn source, along with model fits and residuals, for four pairs of 100 GHz PSBs. The measured transfer functions and errors are shown in black; model fits to Equation 3.22 along with the fitted parameters are shown in red. The blue and green lines are alternative best fit models with the constraints $\alpha = 0$ and $\tau_2 = 0$, respectively. Residual plots for both magnitude and phase are with respect to the red model fit.

The data fit the toy model for the transfer function to sub-% level for the most part, even for problematic channels such as 91 with a significant low frequency tilt. In otherwise "normal" channels,
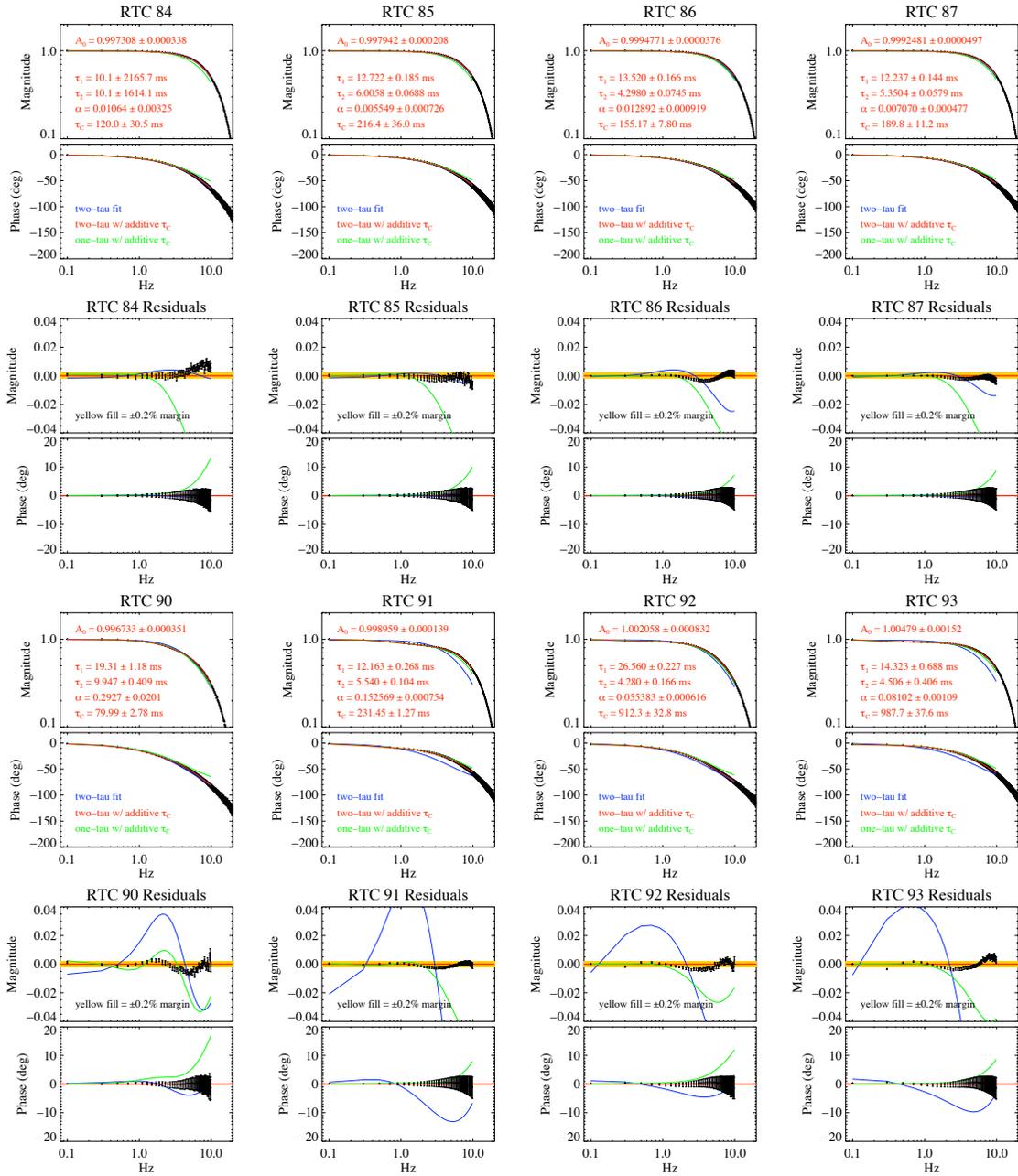
Figure 3.15: Transfer function results from Feb 2006 for a subset of the BICEP focal plane. The fits to Equation 3.22 are shown in red; In blue and in green are alternative best fit models with the constraints $\alpha = 0$ and $\tau_2 = 0$, respectively.
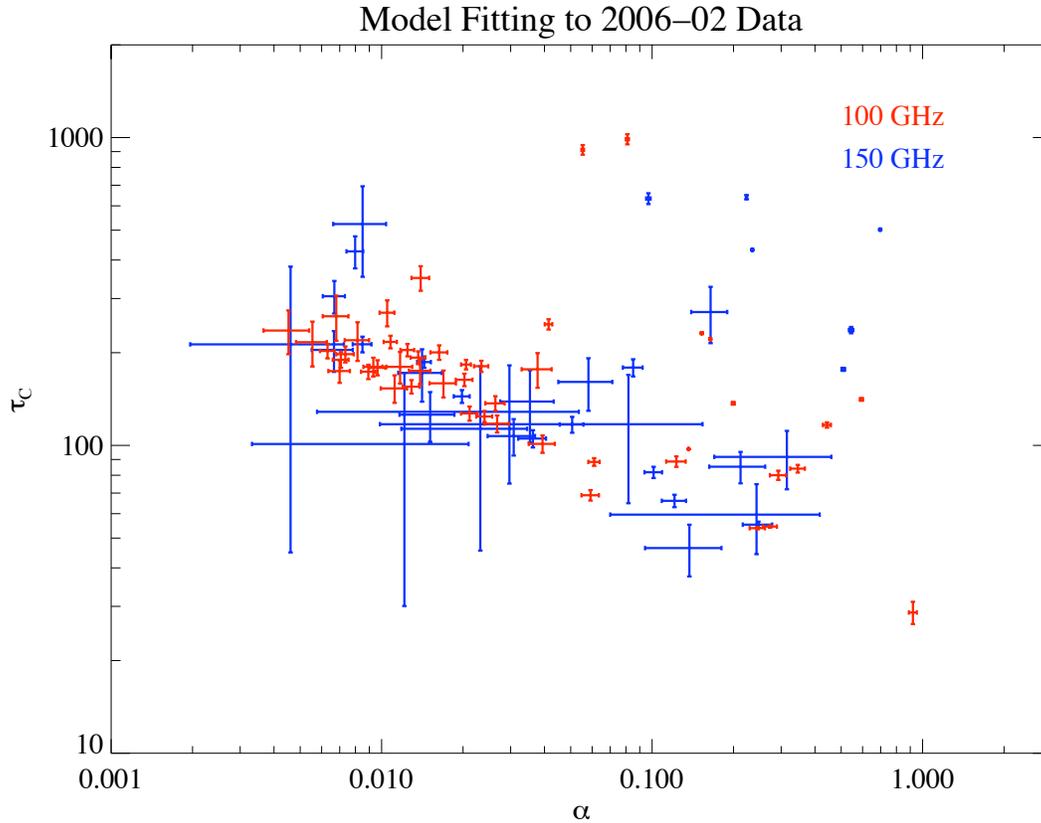
Figure 3.16: Scatter plot of fitted parameters to the toy model.

we typically see $\tau_1 \sim 20$ms and $\tau_2 \sim 5$ms, with negligible additive component ($\alpha \ll 1$). The lack of significant functional deviations from the simple toy model indicates that the analysis method of truncating the "on"-state responses would adequately avoid biasing the measurement.

Considering just the 100 GHz channels from the above data set (not all 150 GHz bolometers had acceptable levels of coupling to the source), ~ 10% of the channels had "medium" levels of additive tau ($0.03 < \alpha < 0.1$, $\tau_c > 100$ ms). Another ~ 10% of the channels had "high" levels of additive tau ($\alpha > 0.1$, $\tau_c > 100$ ms). Figure 3.16 shows τ_c vs. α, as derived from fitting to the full model (red curves/parameters in Figure 3.15). Note that the simple model of two RC filters in series (shown in blue in Figure 3.15) is not adequate to describe the behavior of all bolometers. Channels 90–93 all show modest to significant levels of an additive component in their transfer functions, as do several others channels not shown here.

For significant levels of α (> 0.03) there is a wide distribution of τ_c from channel to channel. Based
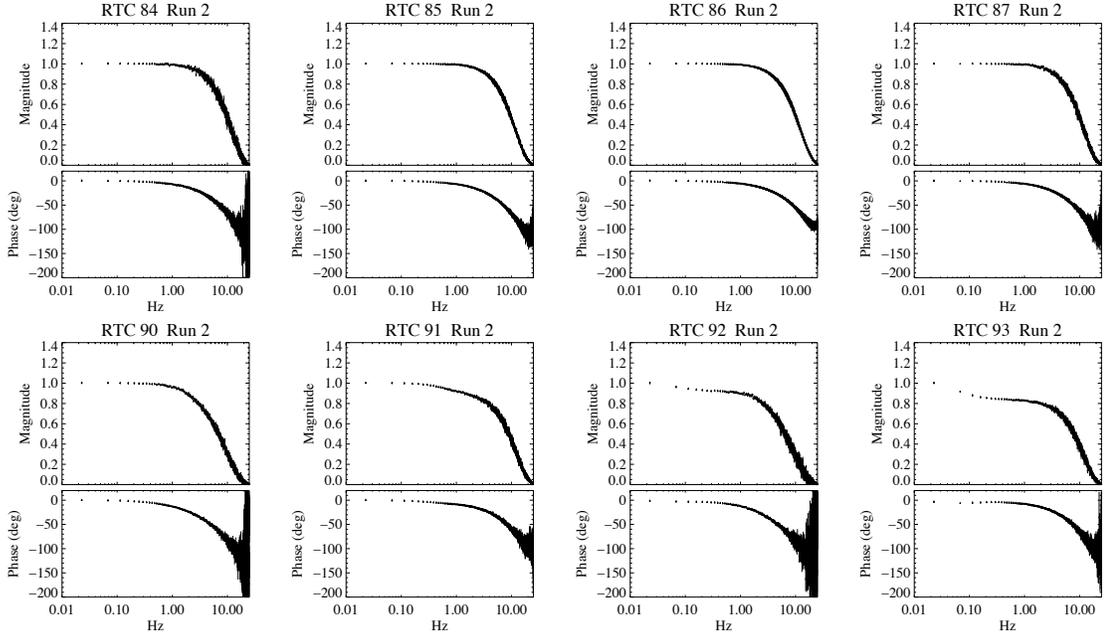
Figure 3.17: Nov 2006 measurements, this time down to 10 mHz. PSBs 92/93 show significant low frequency roll-offs which were not accessible with previous testing.

on this inconsistency we have made the assumption that the low frequency roll-offs from the additive components of the transfer function are driven by unique defects or contaminations on individual bolometers, and not an unanticipated feature of underlying design of the bolometers.

BICEP determines PSB pair relative gains using a slow elevation "nod" to induce a common-mode atmospheric signal at the ~ 50 s timescale. Because of the separation between the frequency at which the relative gains are measured (~ 20 mHz) and the science band (0.1 – 1 Hz), we are sensitive to any transfer function roll-off between 20 mHz and 0.1 Hz, which, if left unaccounted for, will result in $T \rightarrow Q/U$ leakage.

PSB pair 92/93 showed strong evidence of such a leakage in initial CMB maps from first year data, which could not be explained adequately with the 2006 February transfer function results. Figure 3.17 shows the results of second round of testing in 2006 November. Probing down to 10 mHz revealed significant roll-offs below 0.1 Hz for PSBs 92/93 due to extremely large τ_c components, the magnitudes of which were not fully visible with the initial testing due to the limited scope of its frequency coverage.

Because BICEP must deconvolve transfer functions to within 1% to meet its science goals, it is of

paramount importance to accurately characterize the spectra not only within the science band, but down to the low frequency at which the relative gains are fixed. Alternatively, in the future it would be beneficial to construct a calibration regime that takes place *within* the science band because of the inherent difficulty in measuring transfer functions to very low frequencies. A more thermally stable instrument would allow for quicker elevation nods within a ~ 10 s timescale without suffering from undue movement-induced instabilities. A built-in active calibration source with low intrinsic polarization and minimal effects on the background loading during the measurement process would be another alternative.

3.5.4 Follow-up measurements in 2007 February

Most recent measurements of the transfer functions sought to provide reliable and comprehensive results for both frequency bands, and establish confidence on the levels of dependence on loading and non-linearity. For each of the two frequency sources now at our disposal, data were taken with high/low optical loading and high/low modulated signal magnitude. Multiple sets of data were taken at various instrument orientation to ensure complete coverage of all pixels in the focal plane.

In tuning the level of background optical loading for these measurements, we were guided by the actual distributions of loadings seen during the entire first season of observing. The test set-up was adjusted to correspond to these measured ranges.

Figures 3.18 and 3.19 show subsets of the resulting data for 100 GHz and 150 GHz, respectively, for the four possible combinations of the test set-up: low-loading/high-magnitude (red), low-loading/low-magnitude (purple), high-loading/high-magnitude (blue), and high-loading/low-magnitude (green). The error bars shown correspond to the 1σ uncertainties over multiple measurements under identical set-up conditions.

This comparison indicates that there is no significant dependence of the transfer functions on the optical loading, across the range encountered during normal observing, and that any measurement bias due to non-linearity of the bolometers is at a level well below the specified threshold — at least for cases where sufficient S/N was achieved. For bolometers where the measurement uncertainty exceeded 1% for one or more of the four cases, there are no positive detections of a discrepancy
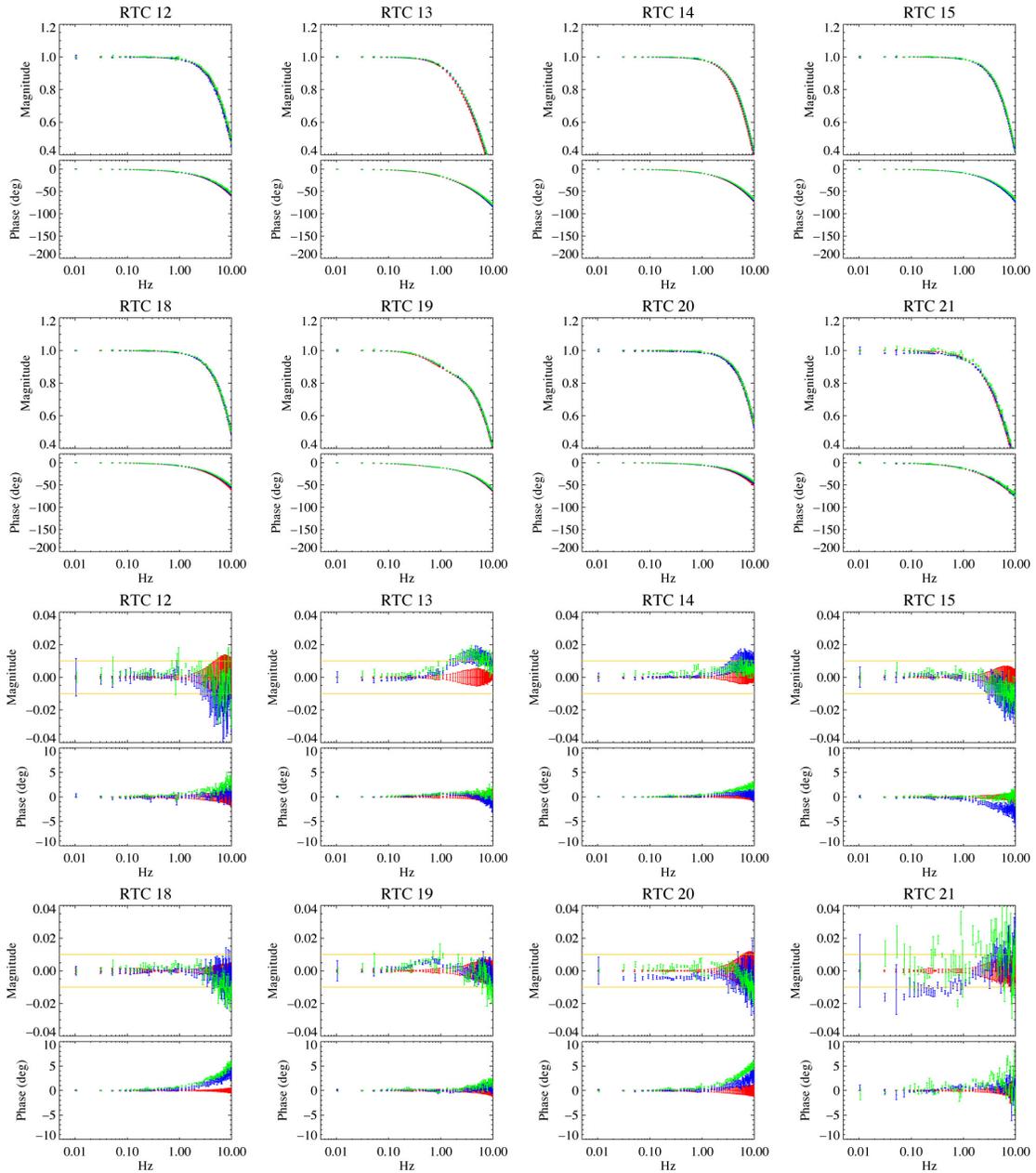
Figure 3.18: Dependency of measured 100 GHz transfer functions on optical loading and modulated signal magnitude. Low-loading/high-magnitude (red), low-loading/low-magnitude (purple), high-loading/high-magnitude (blue), and high-loading/low-magnitude (green). The measured transfer functions for the four cases are shown in the first two rows, for four pairs of bolometers; the bottom two rows show the relative residuals *w.r.t.* the low-loading/high-magnitude case (red).
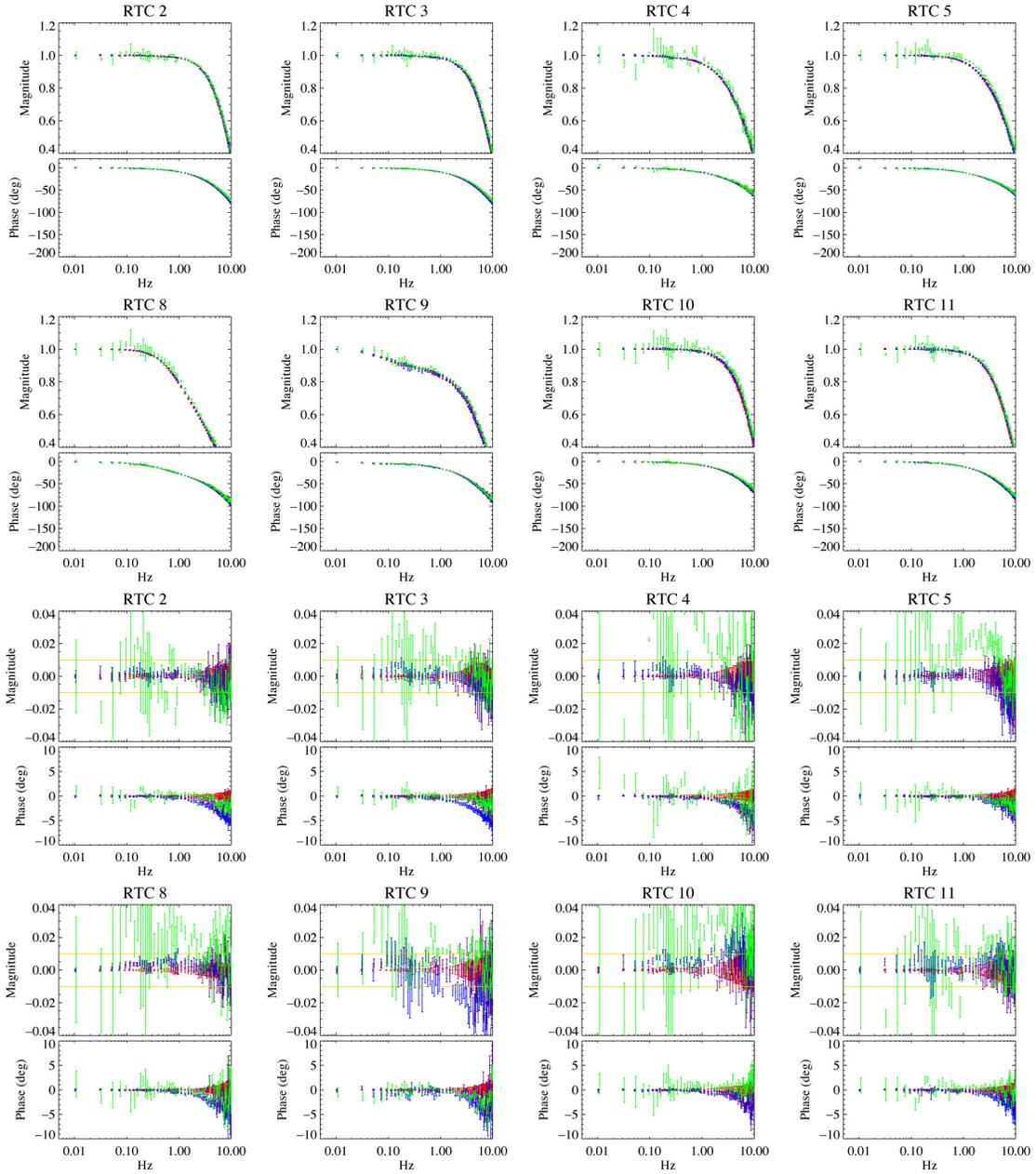
Figure 3.19: Dependency of measured 150 GHz transfer functions on optical loading and modulated signal magnitude. Low-loading/high-magnitude (red), low-loading/low-magnitude (purple), high-loading/high-magnitude (blue), and high-loading/low-magnitude (green). The measured transfer functions for the four cases are shown in the first two rows, for four pairs of bolometers; the bottom two rows show the relative residuals *w.r.t.* the low-loading/high-magnitude case (red).

Figure 3.20: Comparison between transfer function measurements in 2006 February (blue) vs. 2007 February (red).

Figure 3.21: Comparison between transfer function measurements in 2006 February (blue) vs. 2007 February (red) — residuals.

above the noise level.

There was insufficient S/N for the high-loading/low-magnitude measurements for some of the channels, but as there is redundancy in the coverage of the phase space (assuming the loading dependence and non-linearity effects are independent), this does not change the conclusions drawn from this analysis.
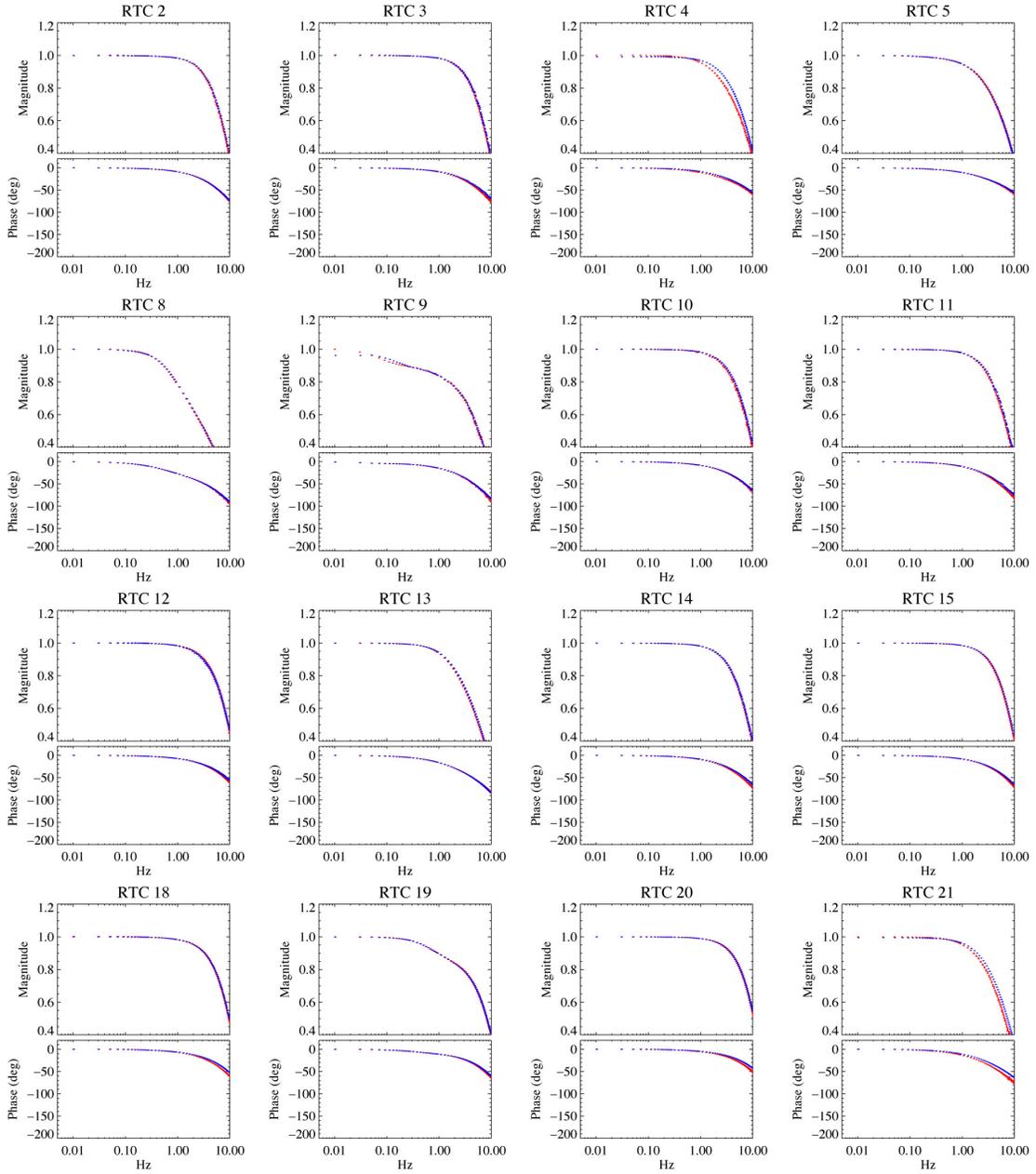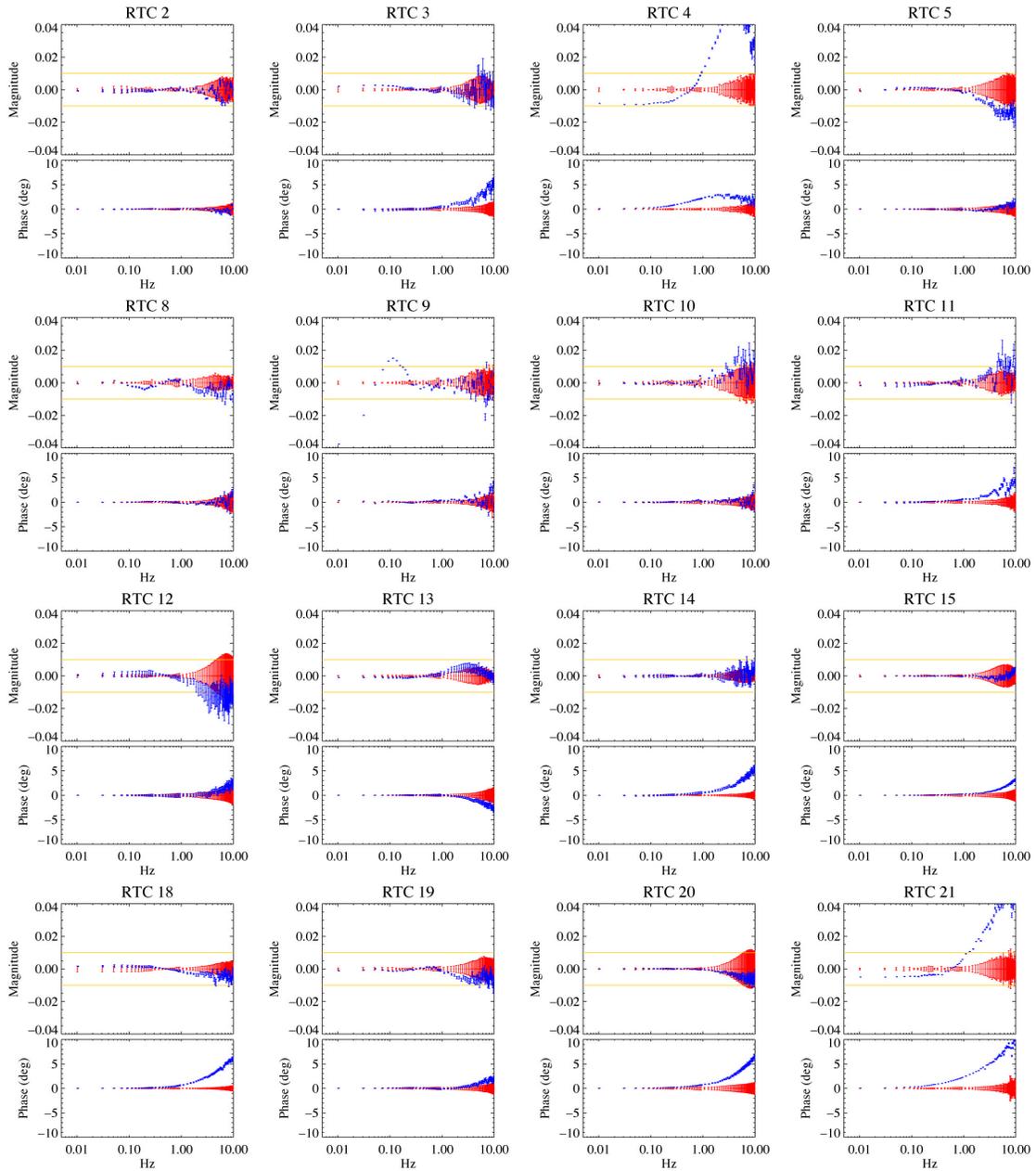
Figures 3.20 and 3.21 compare the transfer functions between the initial 2006 February measurements and the 2007 February measurements. Excluding those channels that had significant additive components — which were found to be unstable in magnitude over time in some cases — only 4 bolometers showed appreciable changes in their transfer function magnitudes exceeding 1% (one of these, bolometer channel 4, is shown here). The consistency of the transfer functions over a year time-scale for all but a few of the 98 light channels support the continuing strategy of using such measurements as year-end calibrations; there doesn't seem to be a compelling reason to carry out the measurements more frequently.

Rather than attempt to deconvolve less-than-ideal transfer functions, some of the channels were cut from the on-going initial CMB data analysis altogether. From the first season focal plane configuration, 7 channels were excluded (2 from 100 GHz and 5 from 150 GHz) for excessive low frequency roll-offs, and a further 4 channels were excluded due to significant inconsistencies between the 2006 and 2007 measurements (1 from 100 GHz and 3 from 150 GHz). One of the 150 GHz pairs with excessive roll-offs were replaced at the end of the season with spare bolometers. From the second season focal plane configuration, a total of 6 channels are excluded from analysis (2 from 100 GHz and 4 from 150 GHz).

Currently, instead of using parameter fits to an analytic model, the measured transfer functions are directly deconvolved from the raw data as one of the first steps in the low-level processing. The achieved S/N on the measurements is high enough that we do not expect the measurement noise to contribute significantly to the filtered and deconvolved timestream data.

Observing Strategy

4.1 The South Pole site

The National Science Foundation Amundsen-Scott Station is located at the geographic South Pole, on the interior ice plateau of Antarctica at an altitude of 2800 m. The extremely dry and stable sky above the South Pole[27] results in 150 GHz opacity of $0.03 < \tau < 0.04$ and atmospheric noise contamination far below Bicep's instrumental noise at least 80% of the time. As such, the South

Figure 4.1: The Dark Sector Laboratory at the South Pole Station, where Bicep is deployed. Further back to the left, the MAPO building houses the QUAD experiment on the DASI mount.
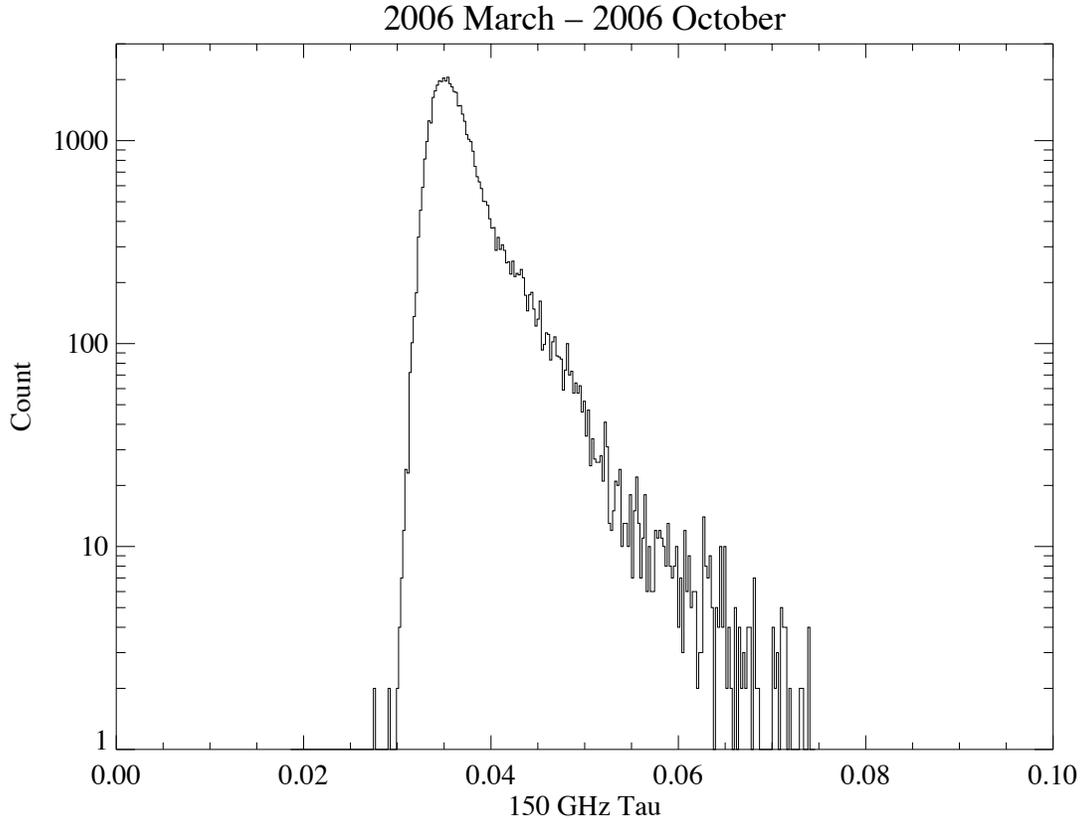
Figure 4.2: Distribution of 150 GHz atmospheric opacity during 2006 observing.

Pole station is one of the best available sites in the world for millimeter-wave observation, offering unparalleled potential sensitivities and observing efficiencies.

We use a 350-μm tipper to continuously monitor the atmospheric transmission, independent of once-a-day sky dip measurements performed at the beginning of every observation cycle. Figure 4.2 gives the histogram of 150 GHz opacity as measured by and extrapolated from the 350-μm tipper during the first season of observation, from 2006 March to 2006 October. The extrapolation is given by a simple linear scaling: $\tau_{150} = 0.0186 + 0.0112\,\tau_{350\mu m}$ as reported by ACBAR from data taken at the South Pole[37]. The $\{25\%, 50\%, 75\%\}$ quartiles for this distribution are $\{0.0345, 0.0360, 0.0382\}$, consistent with measured optical loading for BICEP.

In addition to the excellent atmospheric conditions, from the South Pole it is possible to track a given field continuously at constant elevation angle. The sky that is accessible for observation from the Pole includes some of the largest regions of minimal galactic foreground emission on the celes-

tial sphere. These characteristics of the Pole make it the ideal location for the long, deep integrations needed to study the CMB polarization signal. BICEP is designed to exploit these advantages in the course of extremely long integrations on selected fields. The design of the telescope also reflects the particular environmental challenges of South Pole observations. During the six months of the year for which the Sun (the strongest source of contamination) is below the horizon, presenting optimal observing conditions, the average ambient temperature is −60 °C. Very long integration times demand a design that can ensure reliable telescope performance during this period.

4.2   Observed fields

The mount is capable of observing down to a boresight elevation of 50°, providing access to the minimum foreground regions available from the South Pole. As illustrated in Figure 4.3, we have selected an ~ 800 deg² region centered at {RA = 0 hr, dec = −57.5°} as the main science field, where we spend a total 18 hours per day. A secondary field centered at {RA = 9 hr, dec = −57.5°}, encompassing the bright Eta Carina galactic plane region, is observed for 6 hours every other day, complementing our primary science target with a deep study of the galactic polarization. In addition, a third region at {RA = 15 : 42 hr, dec = −55.0°}, in a significantly brighter part of the galactic plane, serves as a daily calibration source, and we perform repeated fixed-elevation scans for 10 minutes at the beginning and end of every 9-hr observing block.

The selected 800 deg² CMB field is among the lowest in galactic foregrounds available of that size over the entire sky, and certainly the best region accessible from the South Pole. A recent study by the SPUD collaboration (an upcoming large-format CMB polarimeter with similar optical design as BICEP) confirms this[9]. Using the WMAP K-band polarized intensity map extrapolated to 150 GHz as a proxy for the estimate of the synchrotron emission, and the FDS dust brightness model with an assumed uniform 5% polarization fraction, no other region of comparable size is shown to have lower angular power spectra contributions from both synchrotron and dust foreground polarization. With the above assumptions, the B-mode contamination at 150 GHz from dust emission for this region is expected at the level of $r \sim 0.02$, far below the BICEP science target.

The galactic foregrounds have enormous dynamic range over the whole sky, and this is especially
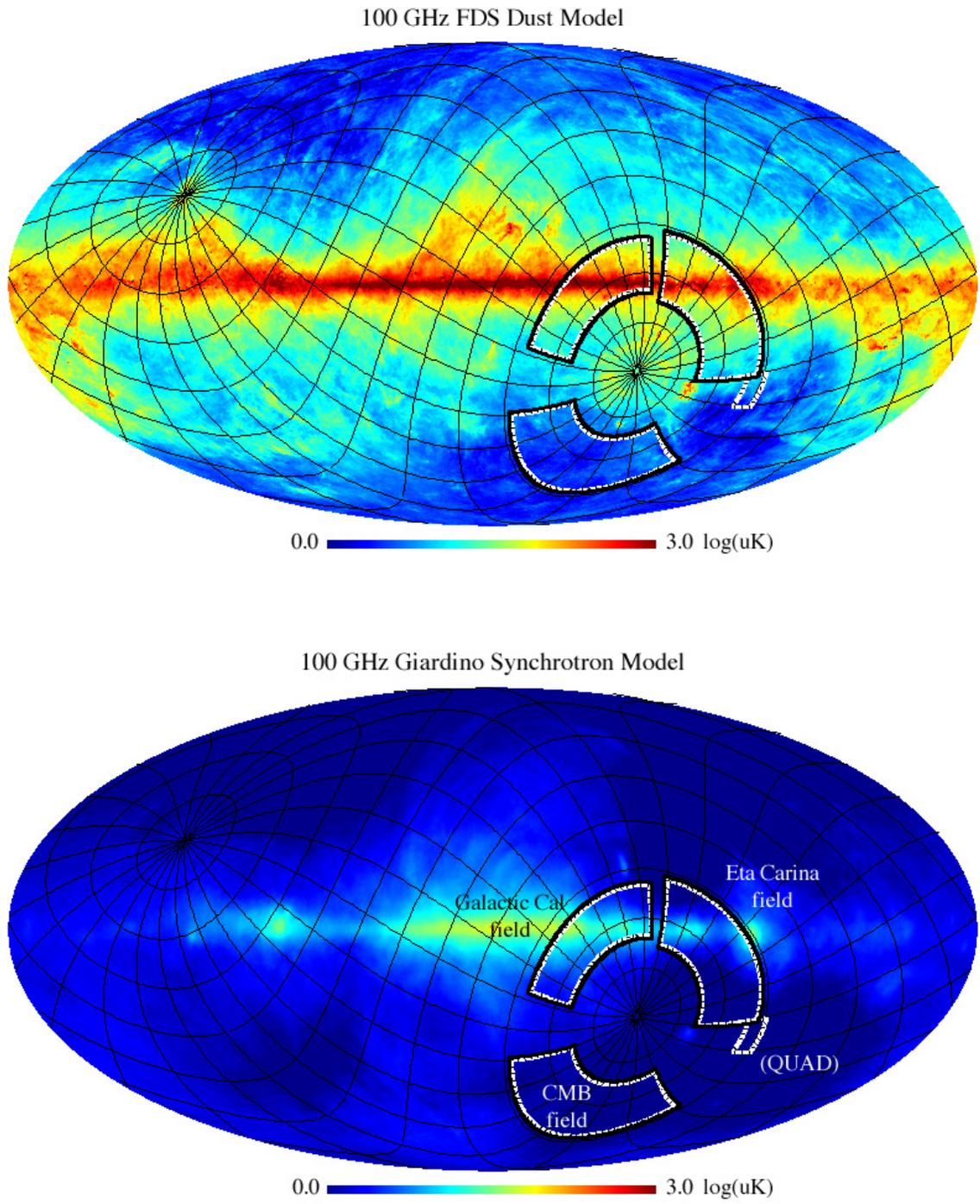
Figure 4.3: Observed CMB and galactic fields, shown against dust and synchrotron model maps.

AZ Scan Profile (v = 2.8 deg/s, a = 1.4 deg/s², j = 0.47 deg/s³)

Efficiency = 70 (78) %

Efficiency in parenthesis indicates cut at $V_{AZ} > 2.0$ deg/s
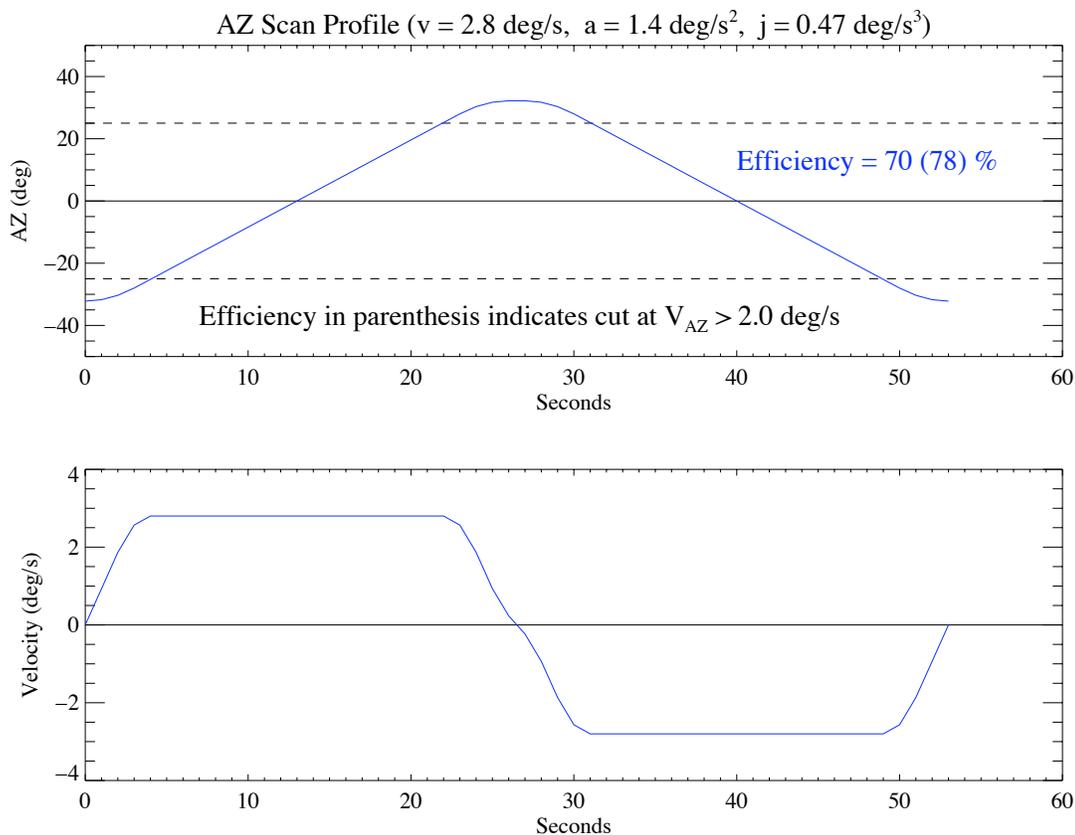
Figure 4.4: AZ scan profile used for both CMB and galactic plane observations. The acceleration during turn-arounds is limited to 1.4 deg/s²; the jerk is limited to 0.47 deg/s³. This results in a strict turn-around efficiency of 70%, keeping only the constant-velocity portions of the data (bounded by the dashed lines). The actual used tur-around cut results in an efficiency of ∼78%.

true for the dust emission. It is necessarily true that as the survey size is increased, the B-mode contamination from galactic foregrounds will also increase, pressuring the optimal sky coverage towards smaller sizes. Although at small enough scales, the gravitational lensing of the E-mode polarization into B-mode will begin to dominate over galactic foreground contaminations, BICEP is in little danger of truly pushing into this limit because of its large instantaneous FOV (17°) and degree-scale beams.

4.3   Scan strategies

In practice, the desire for a high scanning efficiency, rapid scan-modulation of the sky signal, and other operational concerns play not-so-insignificant additional roles in determining the size of the scan region. Fixed-elevation scans at 2.8 azimuth deg /s provide the primary signal modulation, with

Raster Scan Pattern
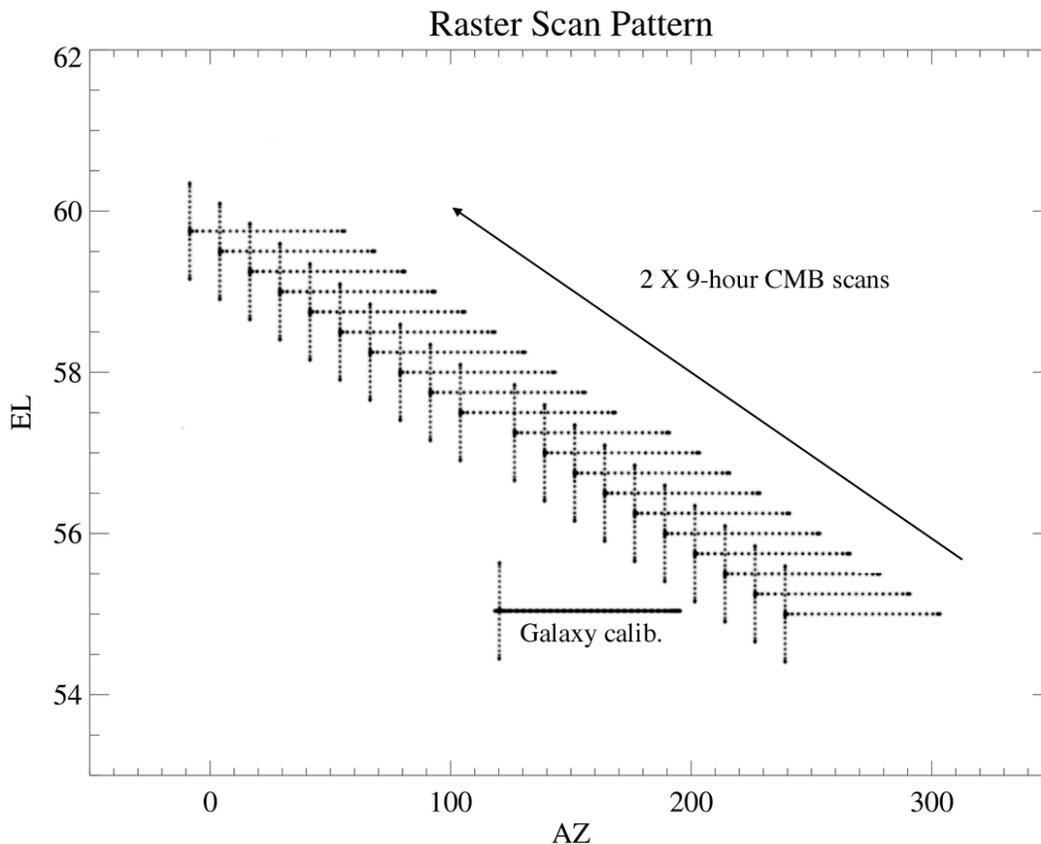
Figure 4.5: Raster scan pattern for an 18-hour observing block. The iso-declination galactic plane calibrations occur at the beginning and end of every 9-hour CMB observing block (only one such set is illustrated here). Each 50-minute scan-set at a fixed elevation is bracketed by 1-degree elevation nods at the beginning and end to measure relative gains.

the selection of this rate driven by both sufficient modulation of the signal against the $1/f$ sky fluctuations, and as an especially quiet speed that does not excite microphonic-induced thermal instabilities on the focal plane.

The constant-velocity span used in observations of the CMB and the Eta Carina fields is $50°$ in AZ, with additional overshoots from smooth turn-arounds with acceleration and jerked capped at reasonable maximum values. The resulting scanning efficiency from this profile is 78%. Deeper integrations on the sky are possible with a more compact observing region, but for the practical limitations of the turn-around efficiency and the desire to avoid keeping data during mount accelerations.

This scan rate maps power on the sky on the angular scales of interest ($\ell \sim 30\text{--}300$) to time domain signals in the range of 0.1–1.0 Hz, above any residual $1/f$ fluctuations. For a given field, we

Field differencing (blue) vs. AZ–fixed Subtraction (red)
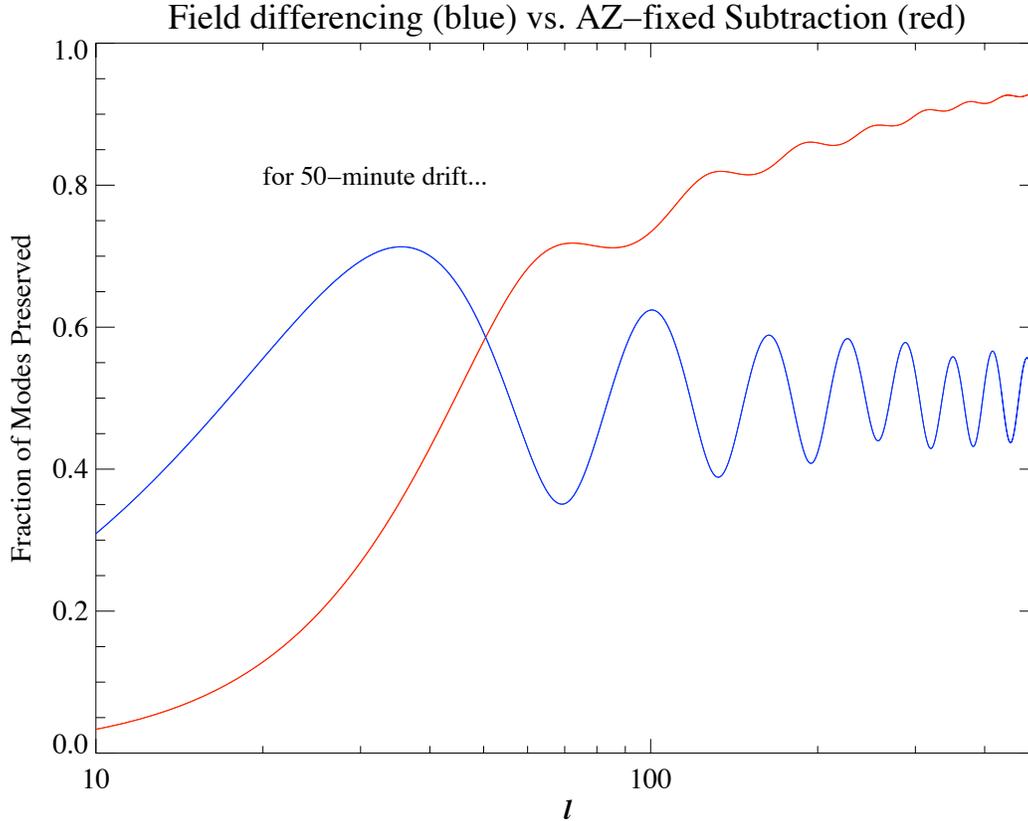
Figure 4.6: Field differencing vs. AZ-fixed Subtraction. While field differencing is commonly used to remove ground-fixed contaminations, the filter function for such method asymptotes to 0.5 at higher spatial frequencies. By fixing the scan *w.r.t.* the ground for 50-minute observing blocks, we can form a model of the contamination as the sky drifts through a fixed opening angle. This preserves more information at the ℓ-range of interest for BICEP.

perform a raster scan, stepping up in elevation by $15'$ at the end of every 50 minutes of azimuth scan and eventually covering $5°$ in boresight elevation, from $55°$ to $60°$.

We have chosen not to track the field center in RA while scanning; rather, we scan about a fixed azimuth and update the tracking to catch up with the field once per elevation step. This has the advantage of making AZ-synchronous and scan-synchronous signals to be degenerate with each other, and separable from the signal on the celestial sphere. We can, if we so choose, project out a model of the AZ/scan-synchronous signal from each scan in RA in the final analysis. This approach is superior to a simple lead-trail field differencing in preserving information on angular scales corresponding to $\ell >\sim 40$. Figure 4.6 shows the numerically-calculated filter functions comparing the lead-trail field differencing (in blue) and the AZ-fixed subtraction method (in red), for an opening angle of $12.5°$
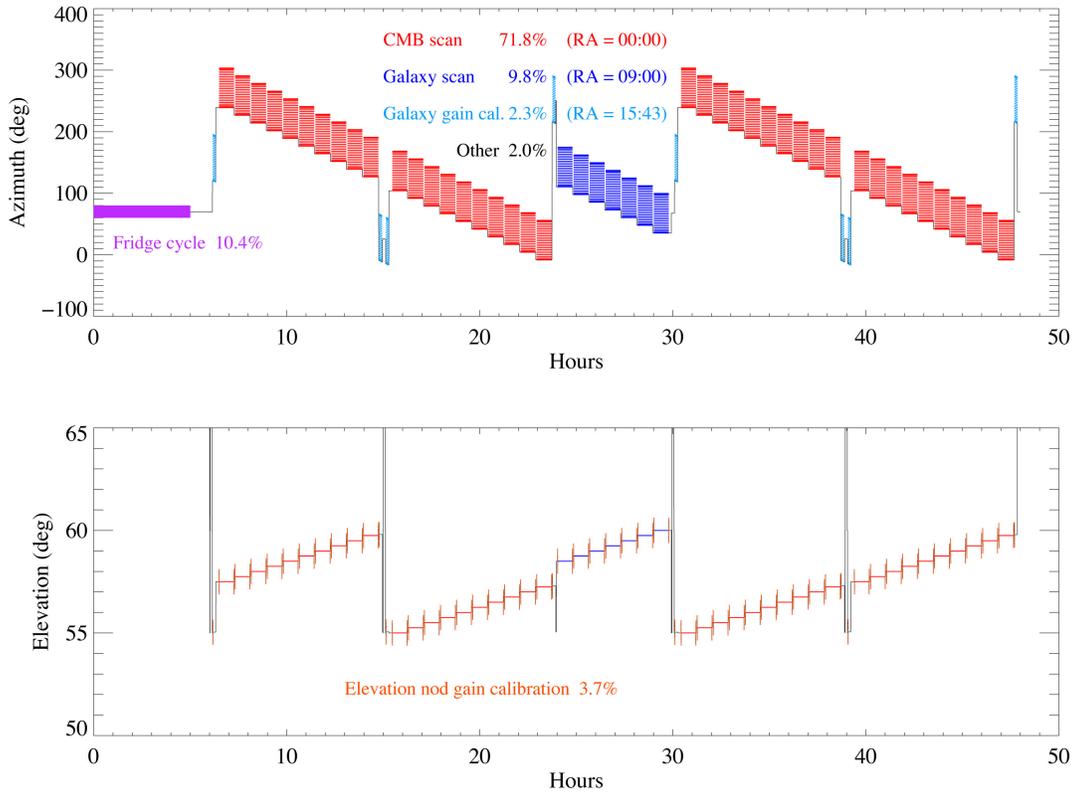
Figure 4.7

in AZ. The direct differencing of two different fields separated by a constant opening angle leads to a factor of 2 in sensitivity loss. While the low-frequency information loss is greater for the AZ-fixed subtraction, information is preserved far better above the cross-over point of $\ell \sim 50$.

Note that there is no penalty associated with the fixed-AZ strategy if we decide against the baseline subtraction. In the analysis of the CMB data so far we have not made use of this baseline subtraction since there has been no indication of detectable levels of ground- or scan-synchronous contaminations.

Bicep operates in blocks of 48 siderial hours. Each observing block is broken up into four distinct phases. The first 6 hours are spent cycling the sub-Kelvin fridge back to 250 mK and servicing the cryogens. Then an 18-hr block of CMB observation completes the first day of the block. The beginning 6 hours of the second day are used to observe the Eta Carina galactic region, then another 18-hr CMB scan follows. The beginning times are arranged such that the 6-hour blocks of servicing

and galactic observing correspond to when the main science field is behind the neighboring SPT, so as to avoid any ground contaminations associated with the large SPT shields.

The order in which the upper and lower halves of the elevation range are covered for the CMB field is swapped between the first and second days, allowing a jackknife to be performed to check for any time-variable AZ-fixed contamination. Each 48-hr block is executed at one of four instrument boresight orientations, at $\theta = \{-45, 0, 135, 180\}^\circ$, giving two independent and complete Q/U coverages of the field. (Because each of the six hextants of the focal plane alternate in polarization orientation of instrument Q and U, a 180-degree rotation about the boresite provides a complete Q/U coverage switch on the sky.) With 78% scan turn-around efficiency and actual CMB observing of 16.7 hr/day, the total observing efficiency is ~ 54% for the CMB science region.

4.4   Gain calibrations

4.4.1   Elevation nods

At the beginning and end of every 50-min fixed-elevation scans across the science target, we perform "elevation nods" for the purpose of tracking the relative response of the bolometers. An elevation nod consists of a sinusoid-like "up-down-return" (normal) or "down-up-return" (inverse) elevation motion of the telescope with total amplitude of 1° and duration of 1 min. We measure $dV_i/d(\csc E_i)$, the voltage response of each bolometer i to the change in airmass at elevation E_i, to correct for the different radiation response of the bolometers. The elevation nods are centered on the same elevation as the contemporaneous science azimuth scan, and they produce a signal of 10–20 mK across the focal plane for a typical atmospheric zenith loading of 10 K. The atmosphere is believed to have negligible linear polarization.[20][14]

The primary purpose of the elevation nods is to determine the relative response of the bolometers within a PSB pair so that atmospheric emission and CMB temperature anisotropy are rejected by the bolometer difference (see Figure 4.7). Over a month of observation, we have measured a typical 1σ repeatability of 0.6% in the gain ratio $\left(\frac{dV_A}{d(\csc E_A)} \right) / \left(\frac{dV_B}{d(\csc E_B)} \right)$, after subtracting systematic trends with atmospheric loading. The elevation nods serve an additional purpose of measuring the relative gains of the detectors over the focal plane, thereby allowing the construction of co-added maps from all of

IR Flash Cal & Elevation Nod
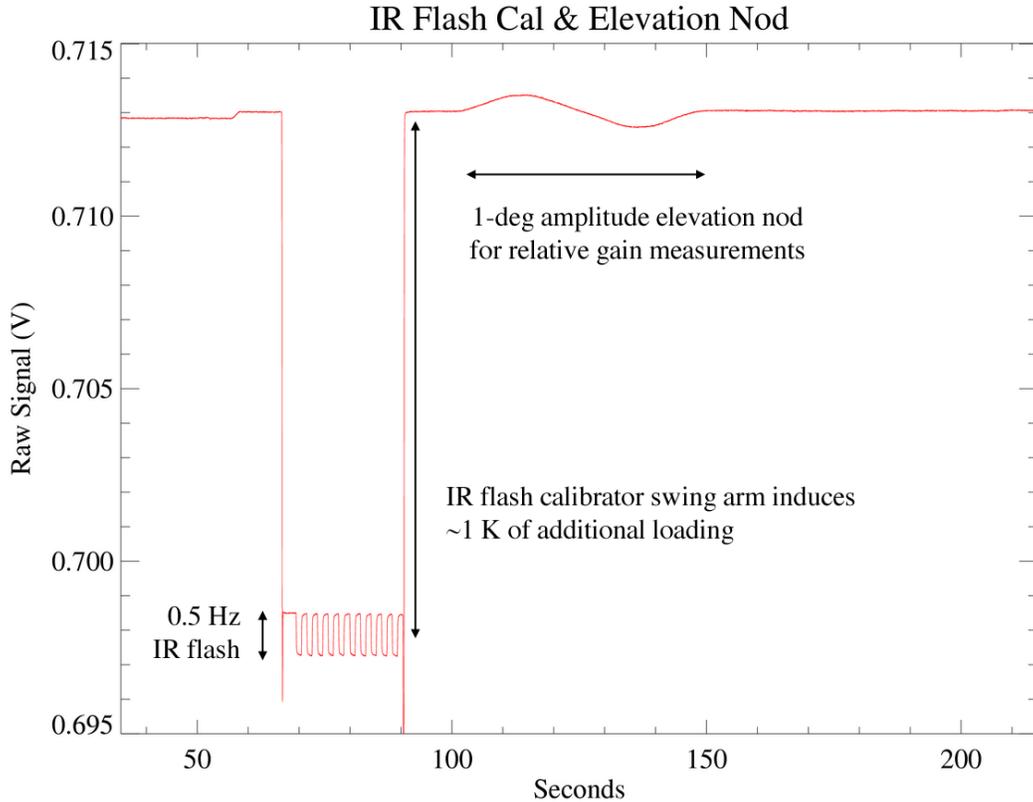
Figure 4.8

the pixels at a given frequency.

In principle, atmospheric emission is rejected perfectly by the elevation nod technique since an atmospheric signal is used to measure the gains. However, since the CMB has a different spectral slope within our bands compared to the atmosphere, good rejection of CMB temperature anisotropy requires good spectral matching of the bolometers. From model atmospheric spectra and typical measured spectral mismatch, we estimate that temperature anisotropy is rejected by a factor of 10^2 for a single PSB. Rejection is improved by an additional factor of ~ 10 since the map pixels are visited by multiple detectors with multiple rotation angles during the scan.

The elevation nod motion produces a thermal disturbance of the focal plane that is detected as a false $\frac{dV}{d(\csc E)}$ in dark bolometers at a level 0.3% of the response in the light bolometers. Alternating between normal and inverse elevation nods allows us to partially subtract this effect. Without accounting for the thermally-induced response and spectral matching, we expect residual CMB temperature anisotropy to appear in our polarization maps at the 0.1 μK level.
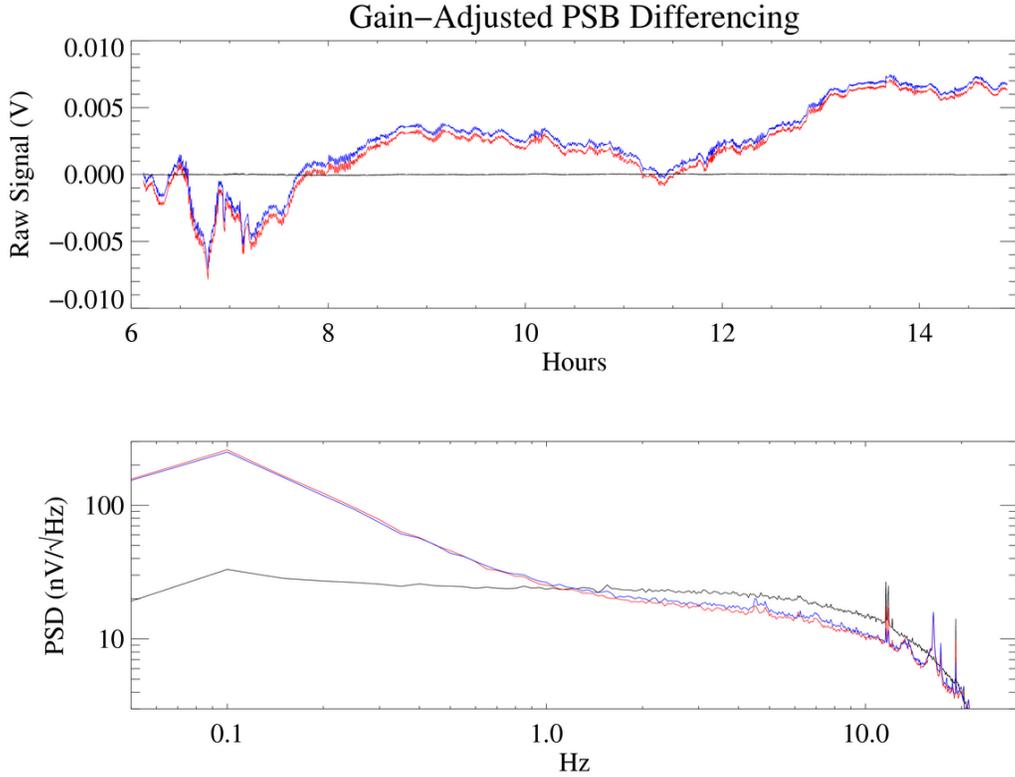
Figure 4.9: Common-mode rejection of the atmospheric fluctuation with gain-adjusted PSB pair differencing. In red and blue are the two PSBs within a pair. After adjusting for the relative gain, the $1/f$ fluctuations are largely nulled out. The differenced signal is shown in black.

The relative gain can be measured directly within a pair, fitting for dV_A/dV_B, instead of a focal plane-wide fit to the airmass model. While this would provide immunity to adverse atmospheric fluctuations during the elevation nods — any unpolarized common-mode input would provide a measurement of the relative gain within a pair, induced by the elevation movement or not — a review of all elevation nod measurements to date and comparison between the pair-derived relative gains and those derived referenced to the airmass show that the two methods agree to well within 1%.

For the current on-going analysis of the first year CMB data, we employ the airmass model fits to derive relative gains for the entire focal plane (scaling the measured relgains such that the mean value over each frequency band is unity, and applying map-derived absolute gains to convert to T_{CMB} as a separate process).

4.4.2 IR flash calibrator

In addition to the elevation nods, we have implemented an infrared source as an independent relative calibrator. An electrically modulated 2.25 mm² infrared emitter packaged into a compact collimating optics[1] is embedded at the end of a Zotefoam arm on the side of the BICEP window. The Zotefoam arm swings into the center of the beam on demand from the control system. Once in the beam, the IR source is pulsed at 0.5 Hz for a period of ~ 1 min, producing a typical optical signal of ~ 100 mK. The flash calibration precedes every elevation nod for redundancy.

We have found that the reliability with which the relative gain is determined compares favorably with that of the elevation nod method, giving us added leverage and redundancy in dealing with potential systematic issues in gain measurements. The flash calibrator-derived relative gains have not been used in the analysis thus far, however, because of concern over biasing due to the extra optical loading introduced by the swing arm, and the unknown polarization of the IR source, however small.

---

[1]IR-55 — Hawkeye Technologies LLC, Milford, CT 06460. Web: http://www.hawkeyetechnologies.com.

CHAPTER 5
Data Analysis

5.1 Summary of collected data

BICEP commenced regular observations of the science CMB field in the beginning of 2006 March, concluding the first year of observation at the end of 2006 October. Excluding aborted or otherwise partial observing blocks, a total of 362 blocks of 9-hour CMB observations were accumulated, equivalent to 181 operational days, or more than 2400 hours of actual data represented in the analysis, taking into account the end-to-end observing efficiencies.

In addition 94 blocks of 6-hour Eta Carina field observations were made, or more than 400 hours of actual data including all cuts, providing unprecedented investigation into the on-plane and off-plane galactic polarization.

After minor upgrades the second season of observing began in 2007 mid-February, and has continued to date, amassing more than 210 operational days of CMB observing. We expect to achieve ~ 250 days before the current winter season comes to a close.

A number of channels out of 98 total light bolometers are excluded from the initial analysis. From the 2006 data, we have excluded 25 channels (11 from 100 GHz and 14 from 150 GHz), including all 12 used in the FRM pixels, for various reasons ranging from excessive noise to abnormal transfer functions. From the 2007 data, we have excluded 12 channels (5 from 100 GHz and 7 from 150 GHz), mostly for abnormal transfer functions. These are conservative cuts; and we can expect some of these channels to be included back as the analysis of the data matures.

5.2 Preliminary CMB maps

The raw data are parsed, cleaned and downsampled into an intermediate time-ordered data (TOD) and stored on disk as inputs to map-making and noise-modelling codes. The transfer functions are deconvolved for each contiguous, uninterrupted block of AZ scanning as a first step, including the portions of the data used for elevation nods. This is so that the nominal normalizations of the measured transfer functions are non-critical, as the relative gains are derived subsequently with deconvolved timestreams.

After deconvolution, the TODs are low-pass filtered and glitch detection is run, flagging every half-scan above a certain skew/kurtosis threshold *w.r.t.* each pair-differenced timestreams. Instead of forming a noise realization of the missing data from glitches, we simply throw away the entire half-scan from map-making. The surviving data are downsampled from 50 Hz to 10 Hz, and relative gains are derived and stored separately.

The CMB maps shown in Figure 5.1 represents data from the beginning of first season observing through 2007 mid-May. The AZ raster scan strategy employed results in a nicely-tapered spatial coverage, with deep integration concentrated in the center $\sim$ 800 deg^2 region. The temperature anisotropy is measured with high signal to noise, as evidenced by the smoothness of the 100-150 GHz jacknife difference map. The WMAP W band 3-year map was scanned with a model of the Bicep instrument and filtered identical to the real data for comparison. There is good agreement in morphologies and their registration, providing an effective way of deriving absolute calibrations of the Bicep maps to within $\sim$ 10%.

The E/B maps are calculated from coverage-weighted input Stokes Q/U maps using PolSpice[8][41]. As shown in these plots, the E/B maps were Wiener filtered according to the E-mode S/N using the B-mode map as the estimate of the noise model.

The data as shown here are aggressively filtered in the time domain to remove $1/f$ fluctuations, as a full analysis of the noise properties and their correlations are still pending. We expect that a more moderate time domain filtering will be possible as the analyses progress, preserving the underlying power spectra better at lower spatial frequencies. Even so, it is notable that we are beginning to see
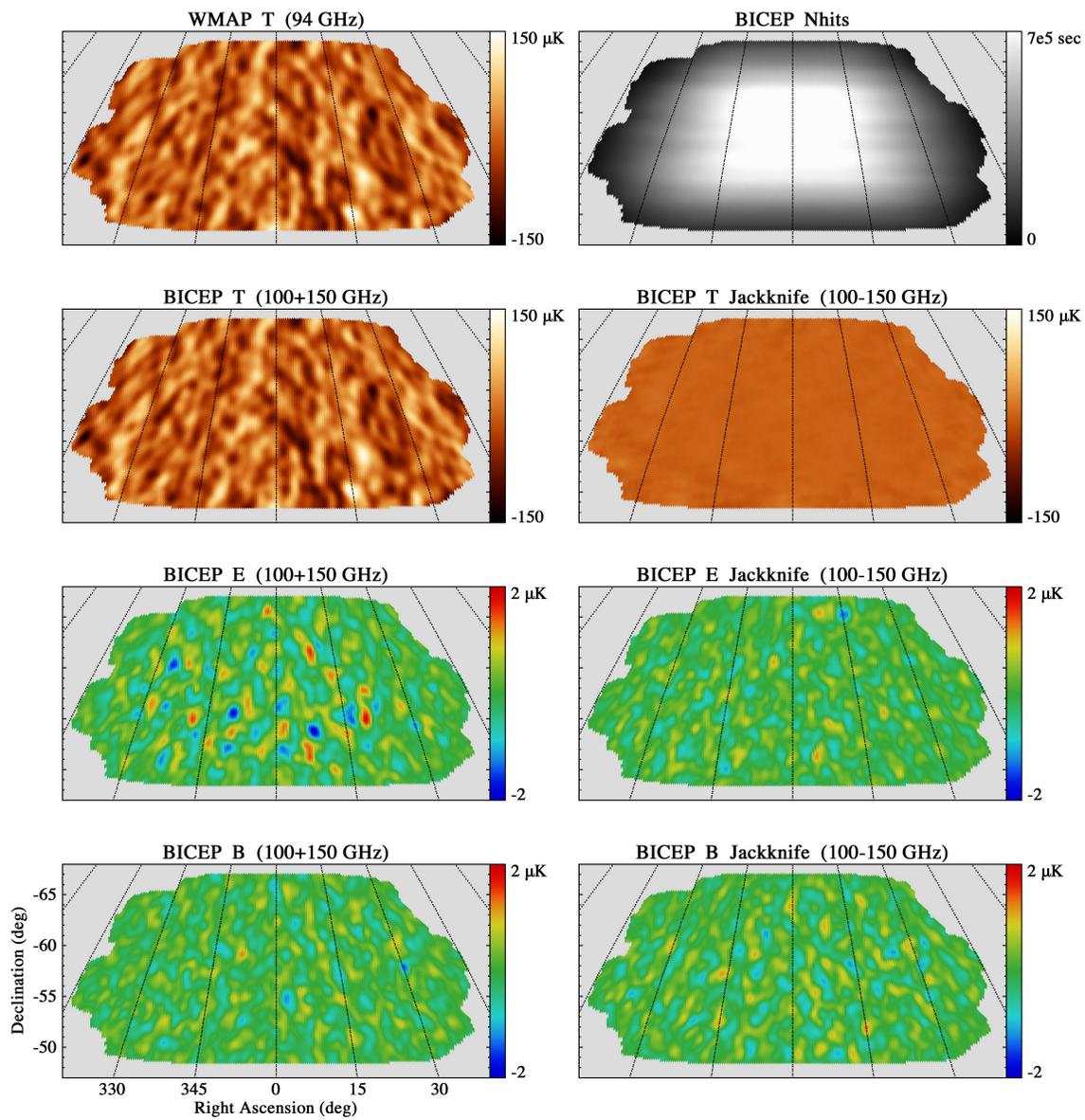
Figure 5.1: Preliminary T/E/B maps from 2006/03–2007/05.
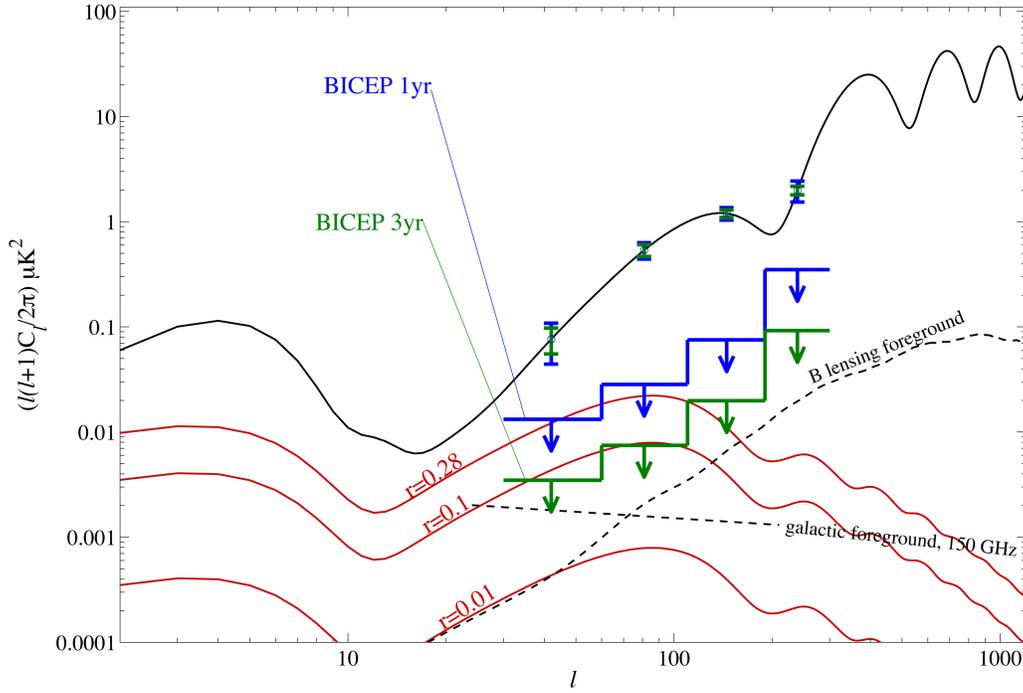
Figure 5.2: Projected performance of BICEP given measured NETs for 1-year and 3-year.

degree-scale features in the *E* map at the expected level, while the *E/B* jacknife maps and the *B* signal map are consistent with noise. The *r.m.s.* 1 deg² noise in 100 GHz is 0.89 μK and 0.77 μK for 150 GHz, in line with expectations.

Figure 5.2 shows expected performance of BICEP for the pending first-year analysis and for 3 years of observations. Given the achieved sensitivities and observing efficiency at the South Pole, we expect to reach the current best upper limits on *r* with the first-year data, and probe down to unprecedented limits for the full duration of the experiment.

5.3 Galactic polarization

Polarized emissions from our own galaxy is of particular interest looking ahead to future experiments, as they will likely set the ultimate limit to the detection of *B*-mode polarization at large angular scales. BICEP has thus far devoted ~13% of total observing to mapping the temperature and polarization of the Eta Carina region, achieving deep integrations on both the galactic plane and the diffuse emissions at moderate galactic latitudes. Figure 5.3 shows the collected data up to 2007 May for this
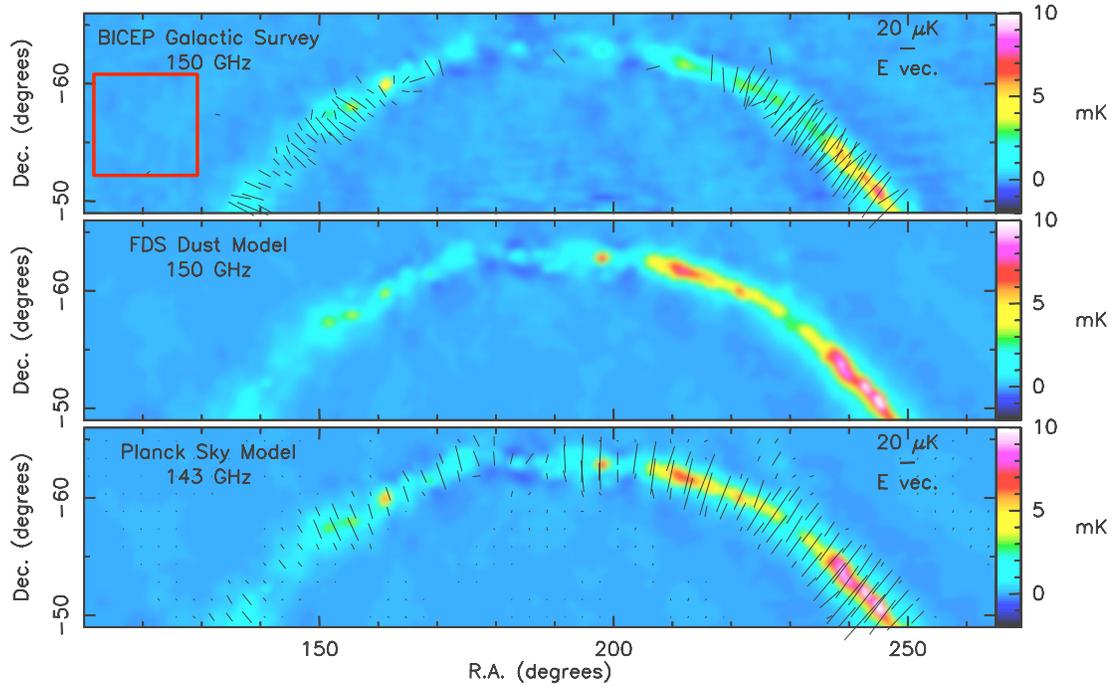
Figure 5.3: 150 GHz survey of galactic polarization compared with FDS and Planck models. Bicep has achieved deep integration over the Eta Carina region encompassing both the galactic plane and the diffuse dust emission at moderate galactic latitudes. The red box outlines such a region where dust structures are seen at the ~ 50 μK level, consistent with the FDS model. Preliminary constraints on dust polarization in this region are < 5%, consistent with recent WMAP all-sky estimates. Bicep measures the polarized emission on the galactic plane itself with high S/N.

field (the left half of the maps as shown) along with shallower coverages elsewhere. For comparison, the FDS model 8[11] and the Planck Sky Model[42] are shown.

The WMAP collaboration has constructed a full-sky model of polarized galactic emission from three years of observations using the 5 frequency channels to separate the contributions from synchrotron and dust polarizations, reporting fractional dust polarization of 0.036 ± 0.011 outside the P06 mask[22]. Preliminary constraints on the dust polarization as derived by Bicep are < 5% at moderate galactic latitudes, consistent with the WMAP estimates. We expect to provide one of the most sensitive characterizations of dust polarization levels at these angular scales pending full analysis of the Bicep data.

APPENDIX A

Instrument Loading & Noise Model

A.1 Thermal model of the NTD bolometer

The behavior of NTD bolometers can be estimated as a suspended thermal mass linked to a fixed bath temperature T_B through a thermal link with its conductance given by

$$G(T) = G_0 \left(\frac{T}{T_0} \right)^{\beta} \tag{A.1}$$

where T is the bolometer temperature and T_0 is just a reference point, often taken to be 300 mK. The NTD thermistor has a temperature-dependent impedance given by

$$R(T) = R_0 e^{\sqrt{\Delta/T}} \tag{A.2}$$

which is biased in series with a fixed load resistor R_L by a bias voltage V_B. The dissipated electrical power across the bolometer then is

$$P_{\mathrm{ELEC}} = \frac{V^2}{R(T)} = \frac{V_\mathrm{B}^2 R}{(R + R_\mathrm{L})^2} \tag{A.3}$$

Typical values for BICEP are: $\Delta = 41.8$ K, $R_0 = 100$ Ω, $G_0 = 60$ pW/K, and $\beta = 1.5$.

The bolometer absorbs incident optical loading Q_{OPT}, and in equilibrium,

$$Q_{\text{OPT}} + P_{\text{ELEC}} = \int_{T_{\text{B}}}^{T} G(T')\,dT' = \frac{G_0 T_0}{(\beta + 1)}\left[\left(\frac{T}{T_0}\right)^{\beta+1} - \left(\frac{T_{\text{B}}}{T_0}\right)^{\beta+1}\right] \tag{A.4}$$

Given a small change in the input optical power:

$$
\begin{aligned}
\delta Q_{\text{OPT}} &= G(T)\delta T - \delta P_{\text{ELEC}} \\
&= G(T)\delta T - \frac{V_{\text{B}}^2}{(R + R_{\text{L}})}\left(1 - \frac{2R}{R + R_{\text{L}}}\right)\delta R \\
&= G(T)\delta T + \frac{R}{2T}\sqrt{\frac{\Delta}{T}}\frac{V_{\text{B}}^2}{(R + R_{\text{L}})^2}\left(1 - \frac{2R}{R + R_{\text{L}}}\right)\delta T
\end{aligned}
\tag{A.5}
$$

The temperature response to a small change in the input optical loading is then given not by $G(T)$ but by an effective thermal conductance G_{EFF}:

$$\delta Q_{\text{OPT}} = G_{\text{EFF}}(T)\delta T \tag{A.6}$$

where

$$G_{\text{EFF}}(T) = G(T) + \frac{R}{2T}\sqrt{\frac{\Delta}{T}}\frac{V_{\text{B}}^2}{(R + R_{\text{L}})^2}\left(1 - \frac{2R}{R + R_{\text{L}}}\right) \tag{A.7}$$

In turn, let's consider the voltage response to a small change in the bolometer temperature T. We have $V = V_b\left(\frac{R}{R + R_{\text{L}}}\right)$, so

$$
\begin{aligned}
\delta V &= \frac{V_{\text{B}}}{R + R_{\text{L}}}\left(1 - \frac{R}{R + R_{\text{L}}}\right)\delta R \\
&= \frac{-V_{\text{B}}}{R + R_{\text{L}}}\left(1 - \frac{R}{R + R_{\text{L}}}\right)\frac{R}{2T}\sqrt{\frac{\Delta}{T}}\delta T
\end{aligned}
\tag{A.8}
$$

We can now express the voltage responsivity to input optical fluctuation strictly in terms of measured bolometer parameters and set values of R_{L} and V_{B}:

$$S = \frac{\delta V}{\delta Q} = -\frac{R}{2T}\sqrt{\frac{\Delta}{T}}\frac{V_{\text{B}}}{R + R_{\text{L}}}\left(1 - \frac{R}{R + R_{\text{L}}}\right)\frac{1}{G_{\text{EFF}}(T)} \tag{A.9}$$

A.2 Optical loading and noise

The spectral radiance of a source at temperature T is

$$B(v) = \frac{2hv^3}{c^3} n_o \qquad \text{where } n_o = \frac{1}{e^{hv/kT} - 1} \tag{A.10}$$

The incident optical load on the bolometer is then

$$Q_{\text{OPT}} = \frac{1}{2} \int \lambda^2 \eta F(v) B(v) \, dv \approx \frac{1}{2} \lambda^2 \eta B(v) \Delta v = hv\eta n_o \Delta v \tag{A.11}$$

making the approximation $\Delta v \ll v_o$. The optical efficiency η and the normalized spectral response $F(v)$ are defined in Section 3.2. Since the average energy of the arriving photons is hv, the photon count per unit time is simply

$$\frac{dN_\gamma}{dt} = \Delta v \eta n_o \tag{A.12}$$

Variance in the arrival rate of photons [44] given integration time Δt is

$$\sigma^2 = \frac{\Delta v}{\Delta t} \eta n_o \left(1 + \eta n_o\right) \tag{A.13}$$

The uncertainty in power at the bolometer is then

$$hv\sigma = \frac{hv\sqrt{\Delta v}}{\sqrt{\Delta t}} \left[\eta n_o \left(1 + \eta n_o\right)\right]^{1/2} \tag{A.14}$$

Evaluating this for $\Delta t = 0.5$ s gives the photon NEP in $\text{W}/\sqrt{\text{Hz}}$:

$$NEP_{\text{PHOTON}} = hv\sqrt{2\Delta v} \left[\eta n_o \left(1 + \eta n_o\right)\right]^{1/2} \tag{A.15}$$

This can be separated into two terms that add in quadrature, and we see that the first dominates over the other if $n_o \ll 1$, and vice versa. For very low photon occupation number n_o, the uncertainty is given by counting statistics; conversely, given high photon occupation number (as is typical in radio astronomy), the noise is proportional to the source temperature. Millimeter measurements of the

CMB in general must account for both.

The two photon noise terms are:

$$NEP^2_{\text{SHOT}} = 2\left(h\nu\right)^2 \Delta\nu\eta n_0 = 2h\nu Q_{\text{OPT}} \tag{A.16}$$

$$NEP^2_{\text{BOSE}} = 2\left(h\nu\right)^2 \Delta\nu\left(\eta n_0\right)^2 = \frac{2Q^2_{\text{OPT}}}{\Delta\nu} \tag{A.17}$$

The Johnson and phonon noises also contribute to the total NET. With the bias voltage constrained, the bolometer impedance is effectively in parallel with the load resistor, and the Johnson noise is

$$NEP^2_{\text{JOHNSON}} = \frac{4kTR_\star}{S^2}\left(\frac{G(T)}{G_{\text{EFF}}(T)}\right) \times 2, \quad \text{where } R_\star = \frac{RR_{\text{L}}}{R + R_{\text{L}}} \tag{A.18}$$

We can estimate the effective temperature of the thermal link to the bath as $T_\star = \left(T + T_{\text{BATH}}\right)/2$, which gives

$$NEP^2_{\text{PHONON}} = 4kT_\star G(T_\star) \tag{A.19}$$

Lastly, the amplifier noise is simply a measured constant, and in BICEP this is

$$NEP^2_{\text{AMP}} = \left(\frac{7\,\text{nV}/\sqrt{\text{Hz}}}{S}\right)^2 \times 2 \tag{A.20}$$

Note the extra factors of 2 for the amplifier and Johnson noises accounting for the post-demodulation bandwidths from AC-biasing of the bolometers.

APPENDIX B

Pointing Reconstruction & Beams

B.1 Coordinate systems

The pointing model describes the orientations of the telescope mount axes relative to the ideal topocentric coordinates with the following set of seven parameters derived from optical star pointing:

$$\{\text{flex}_{\text{COS}}, \text{flex}_{\text{SIN}}, \text{tilt}_{\text{HA}}, \text{tilt}_{\text{LAT}}, \text{tilt}_{\text{EL}}, \text{zero}_{\text{AZ}}, \text{zero}_{\text{EL}}\}$$

The forward pointing model transforms from ideal topocentric azimuth, elevation, and deck orientation $\{A, E, K\}$ of the instrument boresight to raw mount coordinates $\{A, E, K\}_{\text{o}}$. The inverse pointing model transforms from $\{A, E, K\}_{\text{o}}$ back to topocentric $\{A, E, K\}$.

In addition, there are temporary coordinate systems ($\{A, E, K\}'$, $\{A, E, K\}''$, *etc.*) used in the course of applying the pointing model, which I differentiate here explicitly to avoid any confusion in discussing the order of operations. Furthermore, because the raw mount coordinates are not suitable for practical usage nor for making pointing-uncorrected maps ($E_{\text{o}} \approx 7.6°$ at zenith, for example), we regularly make use of yet another coordinate system $\{A, E, K\}_{\text{C}}$ where constant offsets have been subtracted from $\{A, E, K\}_{\text{o}}$. These are stored in the data register `antenna0.tracker.encoder_off`, and updated roughly once every re-leveling of the mount such that $\{A, E, K\}_{\text{C}}$ approximate ideal topocentric values. In successive single transformations starting from J2000 equatorial coordinates, we have:
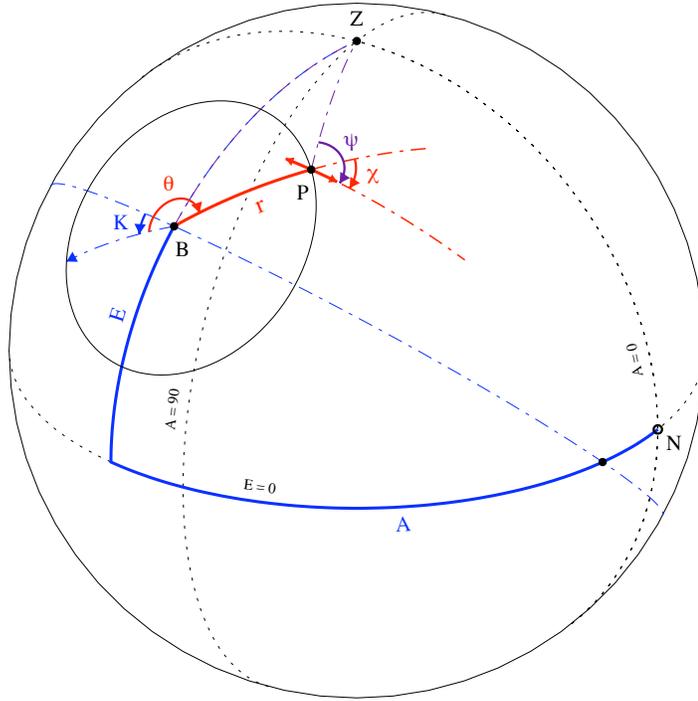
Figure B.1: The relationship between deck orientation angle K about the boresight B and co-moving focal plane coordinates $\{r, \theta, \chi\}$ of pixel P.

$\{\alpha, \delta, \kappa\}$	J2000 equatorial coordinates and DK orientation.
$\{A, E, K\}$	Topocentric ideal horizontal coordinates.
$\{A, E, K\}'$	Horizontal coordinates defined by the actual tilted AZ axis.
$\{A, E, K\}''$	Coordinates given the non-orthogonal tilt of the EL axis.
$\{\ , E, \ \}^*$	Expected (not actual) EL coordinate given flexure terms.
$\{A, E, K\}_\text{o}$	Raw mount coordinates without zero offsets applied: $\{A'', E^*, K''\}$ + offsets.
$\{A, E, K\}_\text{c}$	"Command" coordinates: $\{A, E, K\}_\text{o}$ − `encoder_off[0, 1, 2]`.

Note that because of the transformation involving the non-orthogonal tilt of the EL axis and the large angular extent of the BICEP field-of-view, the pointing model and its inverse should only be applied to the boresight coordinates, and not to coordinates of individual beams.

It is worth reviewing the connection between the DK angle $\{\kappa, K, K', \dots\}$ and the co-moving coordinates of the focal plane. Figure B.1 illustrates this relationship. The instrument boresight B

(defined by the DK rotation axis) is the origin of the focal plane coordinates $\{r, \theta\}$, with $d\vec{\theta} < 0$.[1] The angle χ specifies the polarization orientation *w.r.t.* the radial vector $\vec{r}$ at P, also with $d\vec{\chi} < 0$.

The location of the $\theta = 0$ axis is arbitrary and not physically defined on the instrument *a priori*, but instead referenced to the meridian at $K = 0$. To complete the definition, we need to establish two quantities by conventions: (a) the bearing angle[2] of the $\theta = 0$ direction for $K = 0$ ($\alpha_{B\to\theta_0}$) and (b) the direction of increasing K. The current choices are

$$\alpha_{B\to\theta_0} = -90 \quad \text{and} \quad d\vec{K} > 0 \tag{B.1}$$

which then clearly define the bearing towards P:

$$\alpha_{B\to P} = \theta - K + \alpha_{B\to\theta_0} \tag{B.2}$$

Solving for the reverse bearing $\alpha_{P\to B}$ gives the polarization orientation referenced to the zenith:

$$\psi_P = \chi_P + \alpha_{P\to B} \tag{B.3}$$

Given $\alpha_{B\to P}$ we can solve for $\{A_P, E_P\}$. Together with ψ_P, these coordinates completely determine P on the sky.

However, there is still the arbitrary choice to be made about the zero point of the DK encoder — unlike AZ and EL, the DK angle is a measure of relative orientation and *not* a direction of a vector. This offset is not provided by the pointing model parameters from star pointing, but set by convention:

$$K'' = K_0 - \text{zero}_{\text{DK}}, \qquad \text{zero}_{\text{DK}} = \texttt{antenna0.tracker.encoder\_off[2]} \tag{B.4}$$

which means $K_c = K''$ by definition. To correctly apply the inverse pointing model, we need to augment the five measured model parameters with zero_{DK}. *This is important! Using just the measured parameters will result in the pointing-corrected topocentric DK orientation being off by $\sim 0.9°$.*

---

[1] *i.e.,* angle increases CW looking down.

[2] Bearing at point B is the angle measured CW from zenithal direction.

B.2 Forward pointing model

We start from topocentric ideal $\{A, E, K\}$ and work towards raw mount coordinates $\{A, E, K\}_0$.

B.2.1 AZ axis tilt

The first transformation addresses the tilt of the AZ rotation axis *w.r.t.* the true zenith. The parameters $\{\text{tilt}_{\text{LAT}}, \text{tilt}_{\text{HA}}\}$ — or $\{x, y\}$ for short — measure southward and eastward tilt, respectively, as shown in Figure B.2a. The intersection of the x- and y-tilt great circles (in dotted blue) locates the transformed zenith Z'.

It is convenient to express $\{x, y\}$ in terms of magnitude and azimuth of the tilt $\{\Theta, \Omega\}$. A simple derivation is to apply gnomonic projection[3] centered at Z, which maps $XZYZ'$ onto a rectangle with diagonal $\tan \Theta$. Using $\psi = 180 - \Omega$ and the shorthand $\tilde{\phi} = \tan \phi$ for convenience, then,[4]

$$\tilde{x} = \tilde{\Theta} \cos \psi, \quad \tilde{y} = \tilde{\Theta} \sin \psi \quad \Longrightarrow \quad \tilde{\Theta} = \sqrt{\tilde{x}^2 + \tilde{y}^2}, \quad \tan \psi = \frac{\tilde{y}}{\tilde{x}} \tag{B.5}$$

This is slightly different from the solution cited by CBI and used in QUAD's pointing code, which can be recovered with spherical trigonometry by making the approximation

$$y' \approx y \cos x \quad \Longrightarrow \quad \cos \Theta = \cos(y \cos x) \cos x, \quad \tan \psi = \frac{\tan(y \cos x)}{\sin x} \tag{B.6}$$

valid only for small y.

Typically, $\Theta \sim$ arcmin so that even cartesian approximations $\Theta = \sqrt{x^2 + y^2}$ and $\tan \psi = y/x$ are sufficient, but in other contexts involving large $\{x, y\}$-type angles (*e.g.,* using large x-y offsets in observations, describing the focal plane in cartesian coordinates, *etc.*), the exact solution shown in (B.5) should be used.

Given $\{\Theta, \Omega\}$ and ideal topocentric $\{A, E, K\}$ of point P, we can get $\{A, E, K\}'$ by solving $\triangle ZPZ'$ as shown in Figure B.2b. The sign convention is $d\tilde{\alpha} < 0$ as is for β and γ, and since the coordinates of

---

[3] The projection from the origin onto a plane tangent to the sphere at Z.
[4] I assume the availability of a 4-quadrant range function $\tan^{-1}(\sin \phi, \cos \phi) = \phi$ whenever both arguments are known.
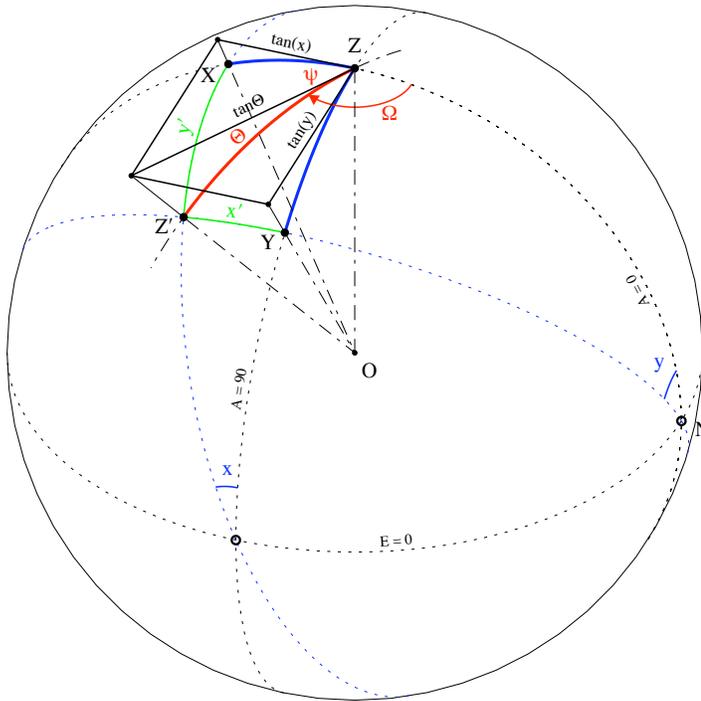
(a) The AZ axis tilt is described by angles $\{x, y\}$, or alternatively in magnitude and azimuth $\{\Theta, \Omega\}$.
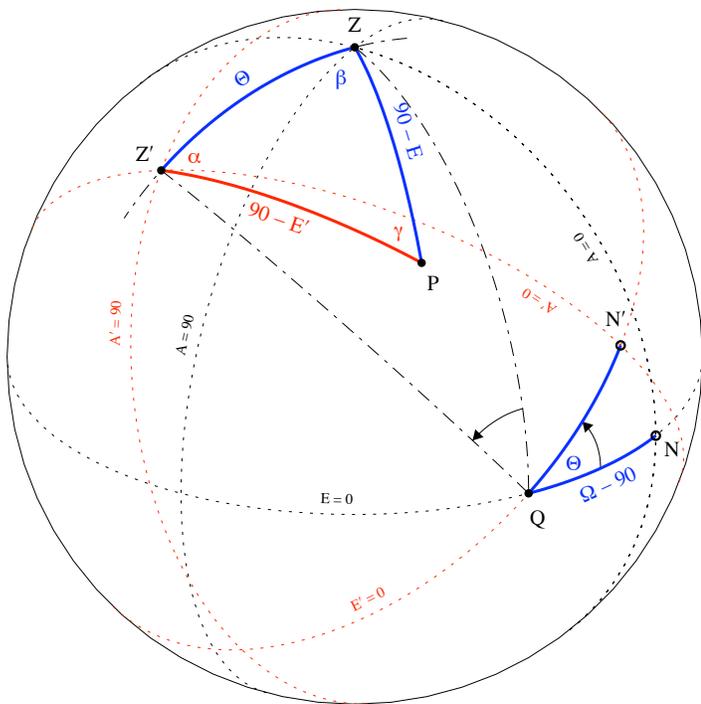
(b) The coordinates of P in the tilted basis is given by solving $\triangle ZPZ'$ on the sphere.

Figure B.2

Q (at the axis of rotation $A = \Omega - 90$) do not transform,

$$\alpha = A' - \Omega + 180, \qquad \beta = \Omega - A, \qquad \gamma = K - K' \tag{B.7}$$

Applying the spherical cosine and sine rules to solve for α, γ, and E',

$$E' = \sin^{-1}\left(\cos\Theta \sin E + \sin\Theta \cos E \cos\beta\right) \tag{B.8}$$

$$A' = \Omega - 180 + \alpha, \qquad \alpha = \tan^{-1}\left(\frac{\sin\beta \cos E}{\cos E'}, \frac{\sin E - \cos\Theta \sin E'}{\sin\Theta \cos E'}\right) \tag{B.9}$$

$$K' = K - \gamma, \qquad \gamma = \tan^{-1}\left(\frac{\sin\beta \sin\Theta}{\cos E'}, \frac{\cos\Theta - \sin E \sin E'}{\cos E \cos E'}\right) \tag{B.10}$$

where $\beta = \Omega - A$.

B.2.2 EL axis tilt

The second transformation addresses the tilt of the EL rotation axis ($\text{tilt}_{\text{EL}} = \Theta_{\text{E}}$) *w.r.t.* the tilted AZ plane (Figure B.3). We only consider rotation about $\overline{OQ}$ since rotation about other axes are degenerate with $\{\text{zero}_{\text{AZ}}, \text{zero}_{\text{EL}}\}$. The direction of $\overline{OQ}$ is defined to be perpendicular to the physical AZ and EL rotation axes, co-moving with the instrument. Note the sign convention $\vec{d\Theta}_{\text{E}} > 0$ at Q.

The internal angles are

$$\alpha \equiv 90, \qquad \beta = 90 - \left(A' - A''\right), \qquad \gamma = K' - K'' \tag{B.11}$$

with α fixed by construction. Gnomonic projections are very useful when right angles are involved, and in this case projecting to a tangent plane at Z' right away gives

$$\cos\beta = \sin\left(A' - A''\right) = \tan\Theta_{\text{E}} \cot\left(90 - E'\right) = \tan\Theta_{\text{E}} \tan E' \tag{B.12}$$

Solving the rest of $\triangle Z'BZ''$,

$$E'' = \sin^{-1}\left(\frac{\sin E'}{\cos\Theta_{\text{E}}}\right), \qquad A'' = A' - \sin^{-1}\left(\tan\Theta_{\text{E}} \tan E'\right), \qquad K'' = K' - \sin^{-1}\left(\frac{\sin\Theta_{\text{E}}}{\cos E'}\right) \tag{B.13}$$
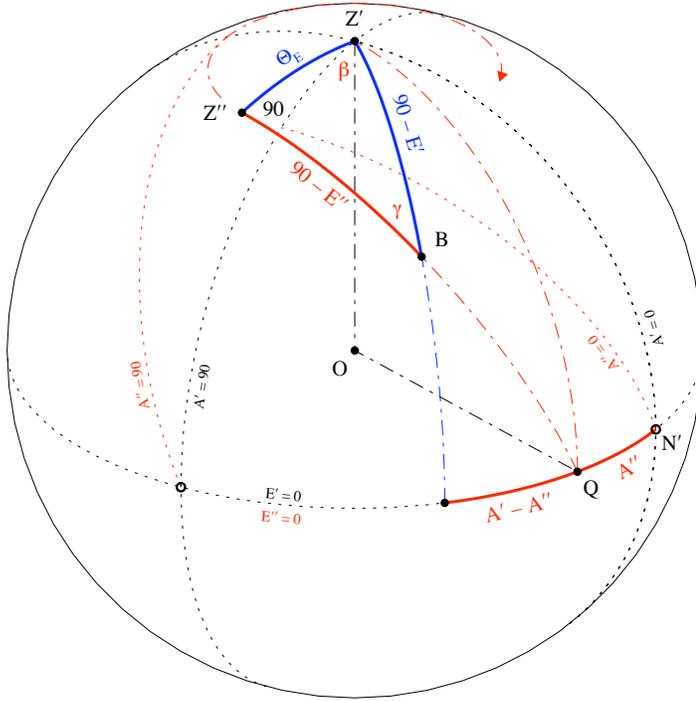
Figure B.3: Tilted EL axis coordinate transformation

B.2.3   EL flexure

The displacement of the center-of-mass (CM) of the cryostat from the EL axis — as well as CM-displacements of substructures from their support points — results in a gravitational torque-induced flexure, and an offset between actual and expected elevation.

A displacement along the DK axis induces an offset $\propto \cos E$, whereas a displacement orthogonal to both the DK axis and the EL axis gives $\propto \sin E$. Defining E_{CM} as the elevation of the effective CM:

$$\Delta E = \rho_f \cos E_{\mathrm{CM}} = \rho_f \cos \left(E - \delta E_{\mathrm{CM}} \right)$$
$$= \rho_f \left(\cos \left(\delta E_{\mathrm{CM}} \right) \cos E + \sin \left(\delta E_{\mathrm{CM}} \right) \sin E \right) \tag{B.14}$$

where δE_{CM} is the downward EL offset of the CM from the DK axis, and the constant $\rho_f < 0$ such that $\Delta E = E_{\mathrm{ACTUAL}} - E_{\mathrm{EXPECTED}}$. Assuming $\Delta E \sim$ small, the transformation from E'' to E^* is then given by

$$E^* \approx E'' - \rho_f \cos \left(\delta E_{\mathrm{CM}} \right) \cos E'' - \rho_f \sin \left(\delta E_{\mathrm{CM}} \right) \sin E'' \tag{B.15}$$

Or, in terms of the fitted parameters:

$$E^* \approx E'' - \text{flex}_{\text{COS}} \cos E'' - \text{flex}_{\text{SIN}} \sin E'' \qquad (\text{B.16})$$

B.2.4 Zero offsets

$$A_{\text{O}} = A'' + \text{zero}_{\text{AZ}}, \qquad E_{\text{O}} = E^* + \text{zero}_{\text{EL}}, \qquad K_{\text{O}} = K'' + \text{zero}_{\text{DK}} \qquad (\text{B.17})$$

Again, $\{\text{zero}_{\text{AZ}}, \text{zero}_{\text{EL}}\}$ come from star pointing fits; $\{\text{zero}_{\text{DK}}\}$ is an arbitrary quantity that reflects the chosen $\theta = 0$ axis of the focal plane, stored in the register `antenna0.tracker.encoder_off[2]`.

B.3 Inverse pointing model

We start from raw mount coordinates $\{A, E, K\}_{\text{O}}$ and transform towards ideal topocentric $\{A, E, K\}$. The order of operation is in reverse. The first three are trivial:

$$A'' = A_{\text{O}} - \text{zero}_{\text{AZ}}, \qquad E^* = E_{\text{O}} - \text{zero}_{\text{EL}}, \qquad K'' = K_{\text{O}} - \text{zero}_{\text{DK}} \qquad (\text{B.18})$$

$$E'' = E^* + \text{flex}_{\text{COS}} \cos E^* + \text{flex}_{\text{SIN}} \sin E^* \qquad (\text{B.19})$$

$$E' = \sin^{-1}\left(\sin E'' \cos \Theta_{\text{E}}\right), \quad A' = A'' + \sin^{-1}\left(\tan \Theta_{\text{E}} \tan E'\right), \quad K' = K'' + \sin^{-1}\left(\frac{\sin \Theta_{\text{E}}}{\cos E'}\right) \quad (\text{B.20})$$

The inverse of the AZ axis tilt transformation can be derived from (B.7)–(B.10) with the substitutions

$$\{A, E, K\} \leftrightarrows \{A, E, K\}', \qquad \alpha \leftrightarrows -\beta, \qquad \gamma \leftrightarrows -\gamma, \qquad \Omega \leftrightarrows \Omega + 180 \qquad (\text{B.21})$$

which give

$$E = \sin^{-1}\left(\cos \Theta \sin E' + \sin \Theta \cos E' \cos \alpha\right) \qquad (\text{B.22})$$

$$A = \Omega - \beta, \qquad \beta = \tan^{-1}\left(\frac{\sin \alpha \cos E'}{\cos E}, \frac{\sin E' - \cos \Theta \sin E}{\sin \Theta \cos E}\right) \qquad (\text{B.23})$$

$$K = K' + \gamma, \qquad \gamma = \tan^{-1}\left(\frac{\sin \alpha \sin \Theta}{\cos E}, \frac{\cos \Theta - \sin E' \sin E}{\cos E' \cos E}\right) \qquad (\text{B.24})$$

where $\alpha = A' - \Omega + 180$.

Bibliography

[1] D. Barkats, C. Bischoff, P. Farese, L. Fitzpatrick, T. Gaier, J. O. Gundersen, M. M. Hedman, L. Hyatt, J. J. McMahon, D. Samtleben, S. T. Staggs, K. Vanderlinde, and B. Winstein. First Measurements of the Polarization of the Cosmic Microwave Background Radiation at Small Angular Scales from CAPMAP. *Astrophysical Journal Letters*, 619:L127–L130, February 2005.

[2] D. J. Benford, M. C. Gaidis, and J. W. Kooi. Transmission Properties of Zitex in the Infrared to Submillimeter. In *Tenth International Symposium on Space Terahertz Technology*, page 405, March 1999.

[3] R. S. Bhatia, S. T. Chase, S. F. Edgington, J. Glenn, W. C. Jones, A. E. Lange, B. Maffei, A. K. Mainzer, P. D. Mauskopf, B. J. Philhour, and B. K. Rownd. A Three-Stage Helium Sorption Refrigerator for Cooling of Infrared Detectors to 280 mK. *Cryogenics*, 40:685–691, 2001.

[4] J. J. Bock. The promise of bolometers for CMB polarimetry. In S. Fineschi, editor, *Polarimetry in Astronomy. Edited by Silvano Fineschi . Proceedings of the SPIE, Volume 4843, pp. 314-323 (2003).*, volume 4843 of *Presented at the Society of Photo-Optical Instrumentation Engineers (SPIE) Conference*, pages 314–323, February 2003.

[5] J. J. Bock, D. Chen, P. D. Mauskopf, and A. E. Lange. A Novel Bolometer for Infrared and Millimeter-Wave Astrophysics. *Space Science Reviews*, 74:229–235, October 1995.

[6] M. Bowden, A. N. Taylor, K. M. Ganga, P. A. Ade, J. J. Bock, G. A. Cahill, J. E. Carlstrom, S. E. Church, W. K. Gear, J. R. Hinderks, W. Hu, B. G. Keating, J. Kovac, A. E. Lange, E. M.

Leitch, B. Maffei, O. Mallie, S. J. Melhuish, J. A. Murphy, G. Pisano, L. Piccirillo, C. Pryke, B. A. Rusholme, C. M. O'Sullivan, K. L. Thompson, and M. Zemcov. Measuring the cosmic microwave background polarization with the QUaD experiment. In J. M. Oschmann, Jr., editor, *Ground-based Telescopes. Edited by Oschmann, Jacobus M., Jr. Proceedings of the SPIE, Volume 5489, pp. 84-94 (2004).*, volume 5489 of *Presented at the Society of Photo-Optical Instrumentation Engineers (SPIE) Conference*, pages 84–94, October 2004.

[7] G. E. Childs, L. J. Ericks, and R. L. Powell. Thermal conductivity of solids at room temperature and below. *National Institute of Standard and Technology*, 1973.

[8] G. Chon, A. Challinor, S. Prunet, E. Hivon, and I. Szapudi. Fast estimation of polarization power spectra using correlation functions. *Monthly Notices of the Royal Astronomical Society*, 350:914–926, May 2004.

[9] SPUD Collaboration, 2007.

[10] L. Duband, L. Hui, and A. Lange. Space-borne He-3 refrigerator. *Cryogenics*, 30:263–270, March 1990.

[11] D. P. Finkbeiner, M. Davis, and D. J. Schlegel. Extrapolation of Galactic Dust Emission at 100 Microns to Cosmic Microwave Background Radiation Frequencies Using FIRAS. *Astrophysical Journal*, 524:867–886, October 1999.

[12] E. Grossman. AT Software. 1989.

[13] A. H. Guth. Inflationary universe: A possible solution to the horizon and flatness problems. *Physical Review D*, 23:347–356, January 1981.

[14] S. Hanany and P. Rosenkranz. Polarization of the atmosphere as a foreground for cosmic microwave background polarization experiments. *New Astronomy Review*, 47:1159–1165, December 2003.

[15] W. Hu, M. M. Hedman, and M. Zaldarriaga. Benchmark parameters for CMB polarization experiments. *Physical Review D*, 67(4):043004–+, February 2003.

[16] W. C. Jones. *A Measurement of the Temperature and Polarization Anisotropies in the Cosmic Microwave Background Radiation*. PhD thesis, 2005.

[17] W. C. Jones, R. S. Bhatia, J. J. Bock, and A. E. Lange. A Polarization Sensitive Bolometric Detector for Observations of the Cosmic Microwave Background. *ArXiv Astrophysics e-prints*, September 2002.

[18] M. Kamionkowski and A. Kosowsky. The Cosmic Microwave Background and Particle Physics. *Annual Review of Nuclear and Particle Science*, 49:77–123, 1999.

[19] B. Keating and A. Lange, 2005. Wide Bandwidth Polarization Modulator, Switch, and Variable Attenuator, US Patent 60/689,740.

[20] B. Keating, P. Timbie, A. Polnarev, and J. Steinberger. Large Angular Scale Polarization of the Cosmic Microwave Background Radiation and the Feasibility of Its Detection. *Astrophysical Journal*, 495:580–+, March 1998.

[21] B. G. Keating, P. A. R. Ade, J. J. Bock, E. Hivon, W. L. Holzapfel, A. E. Lange, H. Nguyen, and K. W. Yoon. BICEP: a large angular scale CMB polarimeter. In S. Fineschi, editor, *Polarimetry in Astronomy*, volume 4843 of *Proceedings of the SPIE*, pages 284–295, February 2003.

[22] A. Kogut, J. Dunkley, C. L. Bennett, O. Doré, B. Gold, M. Halpern, G. Hinshaw, N. Jarosik, E. Komatsu, M. R. Nolta, N. Odegard, L. Page, D. N. Spergel, G. S. Tucker, J. L. Weiland, E. Wollack, and E. L. Wright. Three-Year Wilkinson Microwave Anisotropy Probe (WMAP) Observations: Foreground Polarization. *Astrophysical Journal*, 665:355–362, August 2007.

[23] A. Kogut, D. N. Spergel, C. Barnes, C. L. Bennett, M. Halpern, G. Hinshaw, N. Jarosik, M. Limon, S. S. Meyer, L. Page, G. S. Tucker, E. Wollack, and E. L. Wright. First-Year Wilkinson Microwave Anisotropy Probe (WMAP) Observations: Temperature-Polarization Correlation. *Astrophysical Journal Supplement*, 148:161–173, September 2003.

[24] J. M. Kovac, E. M. Leitch, C. Pryke, J. E. Carlstrom, N. W. Halverson, and W. L. Holzapfel. Detection of polarization in the cosmic microwave background using DASI. *Nature*, 420:772–787, December 2002.

[25] J. D. Krauss. *Radio Astronomy*. 1966.

[26] J. W. Lamb. Miscellaneous data on materials for millimetre and submillimetre optics. *International Journal of Infrared and Millimeter Waves*, 17:1997–2034, 1996.

[27] O. P. Lay and N. W. Halverson. The Impact of Atmospheric Fluctuations on Degree-Scale Imaging of the Cosmic Microwave Background. *Astrophysical Journal*, 543:787–798, November 2000.

[28] E. M. Leitch, J. M. Kovac, N. W. Halverson, J. E. Carlstrom, C. Pryke, and M. W. E. Smith. Degree Angular Scale Interferometer 3 Year Cosmic Microwave Background Polarization Results. *Astrophysical Journal*, 624:10–20, May 2005.

[29] W. Lu and J. Ruhl, 2004. Measurement of Reflectivity of Eccosorb, private communication.

[30] C. J. MacTavish, P. A. R. Ade, J. J. Bock, J. R. Bond, J. Borrill, A. Boscaleri, P. Cabella, C. R. Contaldi, B. P. Crill, P. de Bernardis, G. De Gasperis, A. de Oliveira-Costa, G. De Troia, G. di Stefano, E. Hivon, A. H. Jaffe, W. C. Jones, T. S. Kisner, A. E. Lange, A. M. Lewis, S. Masi, P. D. Mauskopf, A. Melchiorri, T. E. Montroy, P. Natoli, C. B. Netterfield, E. Pascale, F. Piacentini, D. Pogosyan, G. Polenta, S. Prunet, S. Ricciardi, G. Romeo, J. E. Ruhl, P. Santini, M. Tegmark, M. Veneziani, and N. Vittorio. Cosmological Parameters from the 2003 Flight of BOOMERANG. *Astrophysical Journal*, 647:799–812, August 2006.

[31] E. D. Marquardt, J. P. Le, and R. Radebaugh. Cryogenic Material Properties Database. Presented at the 11th International Cryocooler Conference, June 2000.

[32] T. E. Montroy, P. A. R. Ade, J. J. Bock, J. R. Bond, J. Borrill, A. Boscaleri, P. Cabella, C. R. Contaldi, B. P. Crill, P. de Bernardis, G. De Gasperis, A. de Oliveira-Costa, G. De Troia, G. di Stefano, E. Hivon, A. H. Jaffe, T. S. Kisner, W. C. Jones, A. E. Lange, S. Masi, P. D. Mauskopf, C. J. MacTavish, A. Melchiorri, P. Natoli, C. B. Netterfield, E. Pascale, F. Piacentini, D. Pogosyan, G. Polenta, S. Prunet, S. Ricciardi, G. Romeo, J. E. Ruhl, P. Santini, M. Tegmark, M. Veneziani, and N. Vittorio. A Measurement of the CMB <EE> Spectrum from the 2003 Flight of BOOMERANG. *Astrophysical Journal*, 647:813–822, August 2006.

[33] B. J. Naylor, P. A. R. Ade, J. J. Bock, C. M. Bradford, M. Dragovan, L. Duband, L. Earle, J. Glenn, H. Matsuhara, H. Nguyen, M. Yun, and J. Zmuidzinas. Z-Spec: a broadband, direct-detection, millimeter-wave spectrometer. In T. G. Phillips and J. Zmuidzinas, editors, *Millimeter and Submillimeter Detectors for Astronomy. Edited by Phillips, Thomas G.; Zmuidzinas, Jonas. Proceedings of the SPIE, Volume 4855, pp. 239-248 (2003).*, volume 4855 of *Presented at the Society of Photo-Optical Instrumentation Engineers (SPIE) Conference*, pages 239–248, February 2003.

[34] C. W. O'Dell, D. S. Swetz, and P. T. Timbie. Calibration of millimeter-wave polarimeters using a thin dielectric sheet. *IEEE Transactions on Microwave Theory and Techniques*, 50:2135–2141, 2002.

[35] L. Page, G. Hinshaw, E. Komatsu, M. R. Nolta, D. N. Spergel, C. L. Bennett, C. Barnes, R. Bean, O. Doré, J. Dunkley, M. Halpern, R. S. Hill, N. Jarosik, A. Kogut, M. Limon, S. S. Meyer, N. Odegard, H. V. Peiris, G. S. Tucker, L. Verde, J. L. Weiland, E. Wollack, and E. L. Wright. Three-Year Wilkinson Microwave Anisotropy Probe (WMAP) Observations: Polarization Analysis. *Astrophysical Journal Supplement*, 170:335–376, June 2007.

[36] F. Piacentini, P. A. R. Ade, J. J. Bock, J. R. Bond, J. Borrill, A. Boscaleri, P. Cabella, C. R. Contaldi, B. P. Crill, P. de Bernardis, G. De Gasperis, A. de Oliveira-Costa, G. De Troia, G. di Stefano, E. Hivon, A. H. Jaffe, T. S. Kisner, W. C. Jones, A. E. Lange, S. Masi, P. D. Mauskopf, C. J. MacTavish, A. Melchiorri, T. E. Montroy, P. Natoli, C. B. Netterfield, E. Pascale, D. Pogosyan, G. Polenta, S. Prunet, S. Ricciardi, G. Romeo, J. E. Ruhl, P. Santini, M. Tegmark, M. Veneziani, and N. Vittorio. A Measurement of the Polarization-Temperature Angular Cross-Power Spectrum of the Cosmic Microwave Background from the 2003 Flight of BOOMERANG. *Astrophysical Journal*, 647:833–839, August 2006.

[37] M. C. Runyan. *A search for galaxy clusters using the Sunyaev-Zel'dovich effect.* PhD thesis, 2002.

[38] M. C. Runyan, P. A. R. Ade, R. S. Bhatia, J. J. Bock, M. D. Daub, J. H. Goldstein, C. V. Haynes, W. L. Holzapfel, C. L. Kuo, A. E. Lange, J. Leong, M. Lueker, M. Newcomb, J. B. Peterson, C. Reichardt, J. Ruhl, G. Sirbi, E. Torbet, C. Tucker, A. D. Turner, and D. Woolsey. ACBAR: The

Arcminute Cosmology Bolometer Array Receiver. *Astrophysical Journal Supplement*, 149:265–287, December 2003.

[39] M. Shimon, B. Keating, N. Ponthieu, and E. Hivon. CMB Polarization Systematics Due to Beam Asymmetry: Impact on Inflationary Science. *ArXiv e-prints*, 709, September 2007.

[40] J. L. Sievers, C. Achermann, J. R. Bond, L. Bronfman, R. Bustos, C. R. Contaldi, C. Dickinson, P. G. Ferreira, M. E. Jones, A. M. Lewis, B. S. Mason, J. May, S. T. Myers, N. Oyarce, S. Padin, T. J. Pearson, M. Pospieszalski, A. C. S. Readhead, R. Reeves, A. C. Taylor, and S. Torres. Implications of the Cosmic Background Imager Polarization Data. *Astrophysical Journal*, 660:976–987, May 2007.

[41] I. Szapudi, S. Prunet, and S. Colombi. Fast Analysis of Inhomogenous Megapixel Cosmic Microwave Background Maps. *Astrophysical Journal Letters*, 561:L11–L14, November 2001.

[42] Planck Sky Model Team, 2007.

[43] X. Zhang. Design of conical corrugated feed horns for wide-band high-frequency applications. *IEEE Transactions on Microwave Theory and Techniques*, 41:1263–1274, 1993.

[44] J. Zmuidzinas. Thermal noise and correlations in photon detection. *Applied Optics*, 42:4989–5008, September 2003.